

SURFACE AND BULK PROPERTIES OF SOFT NANOCOMPOSITES

DISSERTATION

zur Erlangung des Grades

„Doktor der Naturwissenschaften“

am Department Chemie-Biologie der Universität Siegen

vorgelegt von

Dipl. –Ing. M.Sc. Sascha Alexander Pihan

geboren in Bad-Soden am Taunus

Mainz, den 19. April 2011

Die vorliegende Arbeit wurde in der Zeit von August 2008 bis April 2011 unter der Betreuung von Dr. Rüdiger Berger und Prof. Holger Schönherr am Max-Planck-Institut für Polymerforschung in Mainz angefertigt.

1. Berichterstatter: Prof. Dr. Holger Schönherr

2. Berichterstatter: Prof. Dr. Hans-Jürgen Butt

Abstract

In the context of my thesis I describe my investigations of the interaction of surface grafted polymer brushes with homopolymers. The interaction of surface grafted polymer brushes and homopolymers is mainly determined by their molecular weight ratio¹. By tailoring this molecular weight ratio, fascinating, new effects can be obtained: e.g. a controlled self assembly of nanoparticles² or increased surface wear resistance³. Furthermore the geometry of the surface to which the polymers are grafted plays a major role. In particular, not only flat surfaces can be coated, also curved surfaces like nanoparticles can be coated with dense polymer brush layers. Composites of polymer grafted nanoparticles with like homopolymers show intriguing material properties that are used in high technology products such as car tires. The most studied nanoparticle composites are made from hard, inelastic particles with the aim to increase hardness or tensile strength and decrease abrasion. In contrast to that, my work focuses on the behavior of polymer grafted soft nanoparticles mixed with like homopolymers. Such composites are rarely studied. The aim of my research was to gain some fundamental understanding of the surface wear mechanisms which take place at the surface of these composites on a nanometer scale. I found that the resistance to surface wear of nanocomposites composed of poly(ethyl methacrylate) (PEMA) and PEMA-grafted nanoparticles can be increased while the elastic modulus of the composite remains constant (**chapter 5**). The increment of the resistance to surface wear depends on the molecular weight ratio of grafted brushes (N) and the free homopolymer (P) in the matrix. In a nanowear experiment based on scanning probe microscopy (SPM), I associated a critical force to the onset of nanowear. The definition of this critical force allowed quantitative comparison of nanoparticle-polymer systems of different composition. Increased nanowear resistivity was obtained only for composites where the matrix molecular weight was smaller than the brush molecular weight i.e. $N/P > 1$. The elevated nanowear resistivity was attributed to the increased number of entanglements with the grafted polymer brushes and is a direct consequence of the dispersion behavior of the PEMA-grafted nanoparticles in a PEMA matrix.

In order to get insight into the dispersion behavior, I investigated the dispersion of PEMA-grafted nanoparticles, in terms of the distance between neighboring nanoparticles in a PEMA matrix of varying molecular weight. Daoud and Cotton⁴ extended the model of Alexander and de Gennes^{5,6} for polymer brushes on flat substrates to describe the behavior of star polymers. I could show that this extension is also applicable for polymer-grafted nanoparticles (**chapter 4**). By SPM and grazing

incidence small angle X-ray scattering I was able to analyze the composites on a nanometer scale not only at the surface but also inside the bulk. I found a transition from stable dispersions to aggregated nanoparticles when the molecular weight of the matrix was by a factor of 0.3 to 0.5 smaller than that of the grafted brushes. The transition was assigned to the swelling of the polymer brushes by matrix polymers with low molecular weight. Thus swelling of the surface grafted polymers plays a key role in the surface nanowear behavior while the mechanical properties of the nanoparticles determine the overall mechanical properties which were found to be almost constant (**chapter 4**).

The above characterization of the composite materials was necessary to understand the basic interaction between nanoparticles and its surrounding homopolymers matrix. However, additional parameters like grafting density of the polymer brush layer and processing of the composite materials determine its properties significantly⁷. A detailed study of those properties would go beyond the scope of my thesis. Therefore, I focused on a method allowing for a screening of the mechanical properties of polymers or polymer nanocomposite materials. For the purpose of screening of materials I discuss my approach of using nanomechanical cantilever sensors (**chapter 7**). In order to achieve a homogeneous coating of polymers the same concept is applied that was used to achieve a homogeneous distribution of polymer nanocomposites: The surface of nanomechanical cantilever sensors was functionalized with polymer brushes having a higher molecular weight than the subsequent Inkjet-printed polymer layer. This approach leads to thick homogeneous polymer coatings on cantilevers. When the surface of the cantilever was not functionalized with brushes, the printed polymer did not wet the surface. Only thick polymer films enabled us to explore the mechanical properties of soft films. The mechanical properties of the printed films were then determined by measuring the resonance frequency of the cantilevers (**chapter 7**). An analytical approach was applied to compare the measured resonance frequency of the coated cantilevers with theoretical values. In addition, I performed finite element analysis (FEM) of uncoated and coated cantilevers to identify critical parameters of the coating process. Furthermore, I have shown that the formation of continuous films formed by fusion of colloidal monolayers on a cantilever can be modeled by FEM. Experimental data could be reconstructed qualitatively by a modal analysis of a cantilever-shaped structure covered with spheres in a close-packed pattern. The most exciting part of my work during the PhD was to investigate how small changes in the properties of polymers like the molecular weight can cause dramatic changes of composites with nanoparticles.

Contents

Abstract	I
1. Introduction.....	1
2. Fundamentals.....	3
2.1 Wetting & Dewetting of polymers at interfaces	3
2.2 Tailoring surface properties	4
2.3 Surface-initiated polymerization.....	5
2.4 Entropy controlled miscibility of brush coated nanoparticles in like homopolymers	9
3. Experimental Methods to Investigate Physical Properties of Composites and its Constituents	13
3.1 Classic methods	14
3.2 Methods to investigate thin films	20
3.3. Theory of cantilever mechanics	27
3.4. Inkjet printing of polymeric solutions	29
3.5. Finite Element Method (FEM) with ANSYS.....	30
4. PEMA-g- μ gels and Dispersions with like Homopolymers	33
4.1 Preparation of PEMA matrix polymers.....	33
4.2 Cleaving of the grafted PEMA-chains.....	33
4.3 Characterization of the cleaved PEMA-chains	34
4.4 Characterization of individual particles.....	36
4.5 Characterization of dispersions of PEMA-g- μ gels and homopolymers.....	40
4.6 GISAXS measurements	48
4.7 Dynamic Mechanical Thermal Analysis	51
5. Nanowear in Nanocomposite reinforced Polymers	59
5.1 Nanowear due to constant applied normal forces	60
5.2 Quantification of nanowear for varying N/P ratios.....	63
5.3 Low molecular weight homopolymer blends.....	65
5.4. Blends with varying molecular weight	68

5.5 Reference experiments	69
6. Plasma Deposited Polymer Layers and their Effect on Surface Wear	71
6.1 Preparation of the plasma polymer films.....	73
6.2 Characterization of plasma polymerized multilayers.....	74
7. Towards screening the mechanical properties of polymeric materials	79
7.1 Analyzing the Mechanical Properties and the Cross-link Density of Ion-irradiated Polystyrene Surfaces from Rippling	80
7.2 Micromechanical Cantilever Sensors as a Tool to Characterize Polymer Films.....	85
7.3 Nanoparticle Monolayer Assembly on Silicon Cantilevers.....	100
8. Concluding Remarks and Outlook	105
Dispersion behavior and wear resistivity	105
Cantilever sensors	106
References.....	108
Acknowledgements	119
List of publications.....	121
Oral presentations at international conferences	122
Poster presentations at international conferences	122

1. Introduction

Composite materials are a class of materials with two or more constituents having substantially different mechanical, chemical or optical properties. Within the composite each constituent remains distinct, i.e. they do not dissolve in each other. The constituent which is present in the greater quantity in the composite is named as the matrix. It is also called the continuous phase and is percolated by the constituent of the smaller quantity. Therefore, the properties of the matrix are tailored by incorporating another constituent to form a composite. One of the earliest man-made composite was a mixture of straw and mud formed into bricks for building construction (Figure 1a). Because neat mud bricks were too brittle after drying in the sun, straw was added to reinforce the brick. A straw stalk can accommodate high tensile forces due to its internal, fibered structure (the tensile strength of wheat straw is about 20-30 MPa⁸) and the mud acts as an adhesive for the straw and as additional stiffener. Because the straw percolates the mud in random orientations the brick is reinforced in all directions.

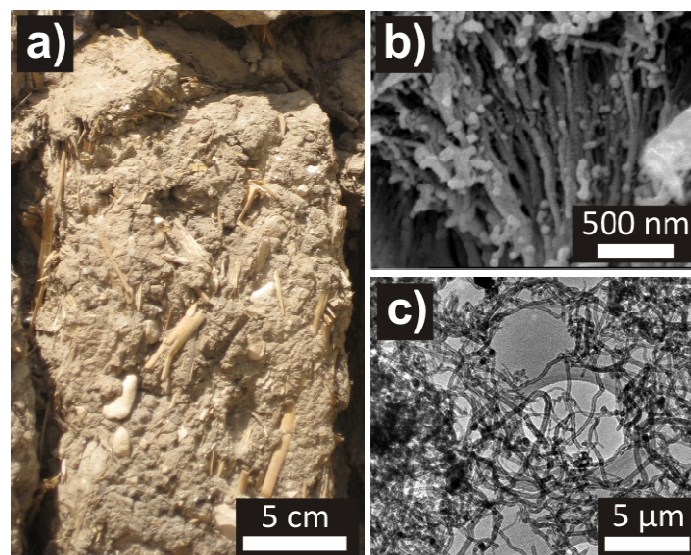


Figure 1. a) A mud brick made in Egypt is one of the first man-made composite material. b) SEM micrograph of a MWCNT composite dispersed in a polystyrene matrix⁹. c) TEM image⁹ of MWCNT synthesized by pyrolysis of CH₄.

In analogy to the straw-reinforced mud bricks, carbon nanotube reinforced polymers (Figure 1b) have gained a lot of interest in material research, chemistry and engineering. Similar to the straw in sun dried mud bricks, the carbon nanotubes (Figure 1c) can accommodate high tensile forces since their tensile strength is approximately 100-600 GPa¹⁰.

Beside the fiber reinforced composites mentioned above, today's best known example of a particle composite is the rubber of car tires which was first invented by John Boyd Dunlop in 1888¹¹. Tires typically consist of a mixture of styrene-butadiene rubber and natural rubber along with many other additives for vulcanization and lifetime enhancement. One crucial constituent to enhance the mechanical properties of tires is silica, which nowadays substitutes carbon black as a reinforcing filler material. It is added in different amounts, depending on the requirements of the tire to enhance abrasion, hardness or tensile strength. The use of silica has several advantages compared to carbon black. The surface of silica can be functionalized with coupling agents via silane chemistry to enhance the compatibility of the particles with the rubber matrix. When the size of the silica particles is in the nanometer range, the composite is called a nanocomposite.

While in car tires the addition of silica increases the hardness and the tensile strength, in thermoplastic materials like polypropylene these effects are sometimes not desired. Polypropylene is widely used in textile, packaging and automotive industry because of its good processibility. However, because of its relatively poor impact toughness, the application as an engineering thermoplastic is somewhat limited¹². Toughness is the ability of a material to absorb energy while plastically deform without fracturing. For some applications it may therefore be advantageous to increase the toughness of a material while keeping its other mechanical properties like elasticity modulus constant. Dental fillings for example must exhibit the ability to withstand wear while their impact toughness should be kept high¹³. A possible route to achieve increased wear resistivity might be the addition of soft, deformable nanoparticles to the polymer matrix.

Because of the high surface to volume ratio of nanometric particles, the particles are most favorably homogeneously dispersed in polymer matrices consisting of a homopolymer with linear chains. The central task in the preparation of nanocomposite materials is the intrinsic incompatibility between the high energy inorganic filler surfaces and the lower energy polymer matrix. As a consequence of this incompatibility, contact aggregation of the filler and macro-phase separation may occur^{14, 15}. Asakura et al. created the term "depletion demixing" for this phenomenon and described it theoretically¹⁶. Entropic effects are the reason for this depletion attraction, as verified experimentally by Bechinger et al.¹⁷. Surface modification (e.g. via silane chemistry) is a typical approach used to overcome the intrinsic incompatibility between nanoparticles and the homopolymer matrix. The surface modification reduces the surface energy difference between the constituents of the nanocomposite and allows for the preparation of homogeneous blends. To understand the effect of the surface energy difference on the dispersion behavior of nanoparticles in polymers. The concept of wetting and dewetting of polymers at interfaces is introduced.

2. Fundamentals

2.1 Wetting & Dewetting of polymers at interfaces

In general the terms wetting and dewetting are referring to the study of characteristic spreading of a liquid on a surface. This phenomenon is of great importance in many industrial areas like paint and ink industry, food packaging and automobile manufacturing as well as tire fabrication. In material science and in particular in composite material design the understanding of wetting and dewetting phenomena is crucial for the preparation and the composition of new materials with desired properties (e.g. homogeneity, dispersion). The wetting and dewetting phenomena can be explained by having a look to the surface of liquids. The liquid surface might be seen as a stretched membrane characterized by the surface tension that opposes its distortion. A molecule inside the liquid phase L benefits from the interactions of all its neighboring molecules. However, a molecule located at the liquid-gas (L - G) interface loses half of its attractive interactions (Figure 2a) which is the physical reason why liquids adjust their shape in order to expose the smallest possible surface area at the liquid-gas interface. If a liquid drop is placed on a solid surface two more interfaces come into play which affects the shape of the drop (Figure 2b). The liquid-gas interface is characterized by the surface tension of the liquid. The liquid-solid (S - L) interface is determined by the difference in surface energy of the liquid L and the solid S and the solid-gas interface (S - G) is determined by the surface energy of the solid.

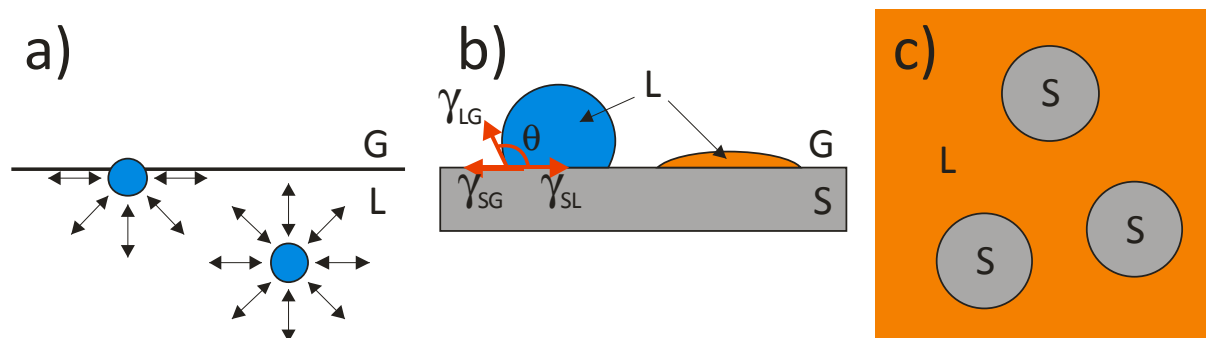


Figure 2. Illustration of the surface tension phenomenon. a) Liquid molecules at the gas-liquid interface. b) Liquid drops with different surface tension on a solid substrate. Indicated are the interfacial surface tensions γ_{LG} , γ_{SG} , γ_{SL} and the contact angle θ . c) Solid particles dispersed in a liquid matrix with similar surface energy.

The surface energy is a measure of the energy necessary to break the chemical bonds of a solid or a liquid to form a new surface. It is defined as the energy that is consumed to generate the surface per unit area. The surface energy of liquids equals their surface tension which can be measured easily

and is given in units of $J \cdot m^{-2}$ or $N \cdot m^{-1}$. As a rule of thumb one can say that materials with strong covalent bonds (mostly materials with a high melting and boiling point) have higher surface energies than materials with weak bonds. For solids the surface energy cannot be measured directly because the above mentioned creation of a new surface involves many other processes that consume energy. With the help of quantum mechanical calculations it is possible to estimate surface energies of solids¹⁸. Whether a drop spreads on a solid surface or not is a question of the energy difference at the *S-G*- the *S-L*- and the *L-G*-interface. The wetting behavior can be described by Young's relation.

$$\gamma_{LG} \cos(\Theta) = \gamma_{SG} - \gamma_{SL} \quad (2.1)$$

The spreading parameter $S = \gamma_{SG} - (\gamma_{SL} + \gamma_{LG})$ distinguishes the two different regimes of wetting. It measures the difference between the surface energy (per unit area) of the substrate when dry and wet. If $S > 0$, total wetting of the surface will occur and the drop spreads out to a film of nanometric thickness. If $S < 0$, the drop does not spread out but forms a cap remaining on the substrate with a contact angle Θ . This effect is referred to the term partial wetting. In contrast to a liquid drop placed on a flat, solid substrate we could also think of a solid particle surrounded by a liquid matrix (Figure 2c). If $S > 0$, the particles would likely disperse in the liquid, like a drop would preferably spread on a surface. Rearranging equation 1) and inserting the spreading parameter leads to the Young-Dupre equation:

$$S = \gamma_{LG}(\cos \Theta - 1) \quad (2.2)$$

which only has a physical solutions for Θ when $S < 0$. Here γ_{LG} is the surface tension of the liquid and Θ is the contact angle of the drop (Figure 2b). If S is close to zero we observe complete wetting. For $S \ll 0$ partial wetting will occur. A drop of poly(ethyl methacrylate) (PEMA) melt placed on a clean silicon wafer has a contact angle of about $36 \pm 6^\circ$. This contact angle would lead to a spreading parameter $S = -0.03$ if we consider a surface energy of 180 mJ/m^2 for silicon (Table 1). This spreading parameter is referred to partial wetting. If we modify the surface of the silicon wafer with a PEMA layer (Table 1) to lower the surface energy of the silicon, a drop of PEMA exhibits a contact angle $< 5^\circ$, which leads to a spreading parameter of $S = -0.0001$. We observe complete wetting in this case. How such a modification of a surface can be performed is explained in the following sections.

2.2 Tailoring surface properties

An elegant way to tailor the wetting behavior of a solid surface by a liquid is to modify the surface in a way to make it hydrophilic or hydrophobic. We know that silicon or glass are high surface energy solids and are wetted by almost all liquids since their surface tension is quite high (Table 1). It has to

be noticed here that total wetting only occurs for perfectly clean and neat surfaces. In the natural state of silicon and glass (that is to say, when stored under ambient conditions) the surface is contaminated with organic and other impurities that have to be removed carefully. On clean surfaces it is possible to lower the surface tension by forming a layer of fluoroalkanes and thus mimicking a fluorinated polymer like PTFE (Teflon).

Table 1. Surface energy γ for selected materials.

Elements ¹⁸	γ [mJ/m ²]	Polymers	γ [mJ/m ²] @ 25°C	Liquids ¹⁹	γ [mJ/m ²] @ 25°C
Si	144 - 180	PDMS ²⁰	21	Pentane	17
C	400 - 970	PE ²¹	30	Toluene	29
		PEMA ^{22, 23}	33-36	Water	74
		PMMA ²¹	40		

The surface becomes hydrophobic and the wetting behavior is changed dramatically. Typically the fluorination of silicon or glass is done by self assembly of perfluoroorganosilane²⁴ molecules at the surface of the sample. Furthermore, low surface energy materials can be altered by a plasma treatment to make the surface hydrophilic. In this process silanole groups are formed in a plasma reactor by feeding a gaseous monomer like hexamethyldisiloxane (HMDSO) which reacts with additional oxygen to form a thin hydrophilic layer on the sample surface²⁵.

In polymer chemistry, the surface-initiated polymerization to generate tailor-made surfaces has become an active research field since around 20 years. Polymer layers in which the polymer chains are irreversibly attached to a substrate surface are of high interest when it is required to balance the surface energy of different materials to allow e.g. wetting of flat surfaces or dispersion of particles in a matrix. I will therefore briefly discuss the concept of surface-initiated polymerization and the theory of polymer brushes in the next section.

2.3 Surface-initiated polymerization

Surface-initiated polymerization is a technique based on the growth of polymer chains at initiator molecules, which are covalently bound to a substrate surface. This technique is also called “*grafting from*” in opposition to the approach called “*grafting to*”, where already existing polymer chains are grafted to the surface. Polymer layers obtained via *grafting from* are attractive for a variety of applications because of their stability against mechanical impact and solvents. In a polymer layer with a high grafting density Γ the polymer chains adopt a rather unusual conformation. The individual coils overlap and the chains are strongly stretched away from the surface (Figure 3a). This

conformation is far away from how a polymer chain would configure in solution and such systems are referred to as “polymer brushes”.

2.3.1 Polymer brushes

There are several methods of surface modification reported including silanization^{26, 27}, surfactant absorption²⁸ and polymer grafting²⁹. For large particles, the stabilization by grafting polymers to the particle surface has been conducted for many years³⁰. As shown by Schärfl et al.³¹ and others³²⁻³⁴ grafting polymer brushes can also stabilize nanoparticles in suspensions. These polymer grafted nanoparticles can be homogeneously dispersed in polymer matrices forming stable suspensions with exceptional mechanical properties^{35, 36} e.g. an increased dynamic storage modulus G' .

Scientifically and practically polymer brushes are very interesting systems because the strong stretching of the chains leads to drastic changes in the physical properties of the polymer layer. If random coils are molecularly deformed, only a small amount of energy is stored in the system as an increase in entropy. If the chain is attached to a surface and is already strongly stretched like in polymer brushes (Figure 3), it has less degree of freedom compared to the random coil. Thus, to induce a small deformation in the brush, the energy penalty is much larger. Such a deformation might be induced by the penetration of solvent molecules or other polymer molecules from solution into the polymer brushes. However, these entropic reasons lead to totally different conformational changes of the brushes when they are in contact with other molecules compared to free coils in contact with other molecules.

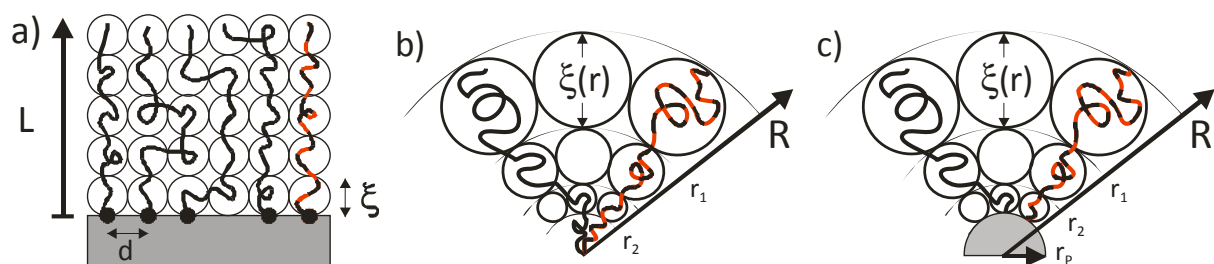


Figure 3. Schematic illustration of stretched polymer brushes. a) The Alexander model theoretically describes the chains with “blobs” of size ξ where the segments behave like random coils. The segments are illustrated as alternating red and black parts of the chain. b) Star-polymers as described by Daoud and Cotton and c) polymer brushes grafted on spherical particles with radius r_p and blob size $\xi(r)$.

The very first theoretical description of polymer brushes attached to planar surfaces at distance d in a good solvent (Figure 3a) was given by Alexander⁵ and got further developed by de Gennes⁶ for polymer brushes in contact with a polymer melt. In both models the brushes are represented by a succession of blobs with size ξ . Each blob contains a number of polymer segments (illustrated as alternating red and black parts of the chain in Figure 3), resulting in a segment density φ for each blob.

Alexander calculated the interaction energy of binary monomer-monomer interactions and the elastic energy of a Gaussian chain and minimized the results with respect to the brush height. In this way he proposed a relation which predicts the experimentally observed scaling behavior more or less correctly. For good solvents the brush length L scales with the degree of polymerization N and the grafting density Γ as

$$L \sim N \cdot \Gamma^{1/3} \quad (2.3)$$

and for brushes in a poor solvent, that is close to the Θ condition as

$$L \sim N \cdot \Gamma^{1/2} \quad (2.4)$$

For star shaped polymers, Daoud and Cotton⁴ developed a model which extended the work of Alexander and de Gennes. They considered a star with f branches joining at the origin of the star. Each branch has N statistical units of length l . The size of the blobs in this case is a function of the distance to the centre of the star $\xi = \xi(r)$ assuming spherical coordinates (Figure 3b). Each blob has a local monomer concentration φ which is also a function of the distance to the centre $\varphi = \varphi(r)$. Three different regions for the conformation of a single brush can be defined:

1. **The core region:** At small distances x to the centre of the star the concentration $\varphi(r)$ is unity for $x < r_2$. They expressed r_2 as

$$r_2 = f^{1/2}l \quad (2.5)$$

2. **The unswollen region:** In this region the excluded volume effects start to influence the monomer concentration. r_1 denotes the crossover distance between the unswollen and the swollen regime and is defined as

$$r_1 = f^{1/2}v^{-1}l \quad (2.6)$$

where v is the monomer excluded volume parameter ($v = \frac{1}{2} - \chi$), and χ is the Flory interaction parameter which is zero for athermal mixtures^{37,38}.

3. **The swollen region:** In the swollen region the branches behave like single chains. Thus, in a good solvent and for large distances x , the local behavior is supposed to be swollen.

The radius of the star R can then be evaluated by the condition

$$Nfl^3 = \int_0^R \varphi(r) dr \quad (2.7)$$

leading to⁴

$$R = \left[Nf + \frac{1}{10} \frac{f^{3/2}}{v^2} + \frac{1}{6} f^{3/2} \right]^{3/5} v^{1/5} f^{-2/5} l \quad (2.8)$$

The model for star shaped polymers of Daoud and Cotton can also be applied as a first approximation to brushes attached to curved surfaces, i.e. spherical particles of radius r_2 (Figure 3c). Since in this model the blob size $\xi(r)$ increases with radius r , it leads to the main difference when we go from planar to curved surfaces. For polymer brushes attached to planar surfaces the segment density φ stays constant and drops at a distance $x = L$ depending of the polydispersity of the brushes (Figure 4a). For star shaped polymers, the segment density is constant for $x < r_2$ (Figure 4b). If the brush is attached to a spherical particle with radius r_p the density is zero for $x < r_p$ (Figure 4c). For $x > r_2$ the segment density φ drops in a nonlinear behavior and reaches the swollen region.

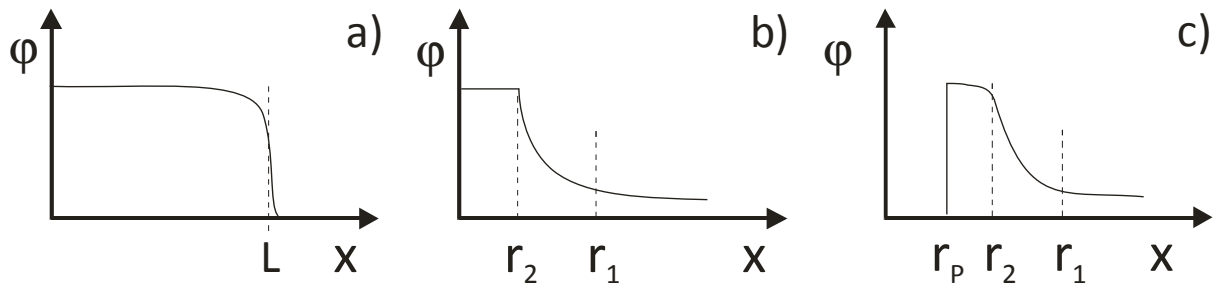


Figure 4. Schematic illustration of the segment density profile of polymer brushes attached to a) planar surfaces, star shaped polymers b) and brushes attached to curved surfaces.

Since the segment density at $x > r_2$ is decreasing with increasing distance r , there is more free volume at the brush ends ($x > r_1$) which might be occupied by “solvent” molecules. These solvent molecules might also be free polymer molecules from a surrounding polymer melt that can interact with the polymer brushes. As stated before, the aim of a surface modification with polymer brushes is to balance the surface energy difference between the nanoparticles and the surrounding matrix, to allow the preparation of homogeneous blends. The case in which the miscibility is affected by the interaction between brush and matrix will be discussed in the next section.

2.4 Entropy controlled miscibility of brush coated nanoparticles in like homopolymers

Current approaches in polymer media design aim at adding new functionalities, reducing the weight of fabricated components and furthermore enhancing mechanical properties of polymeric materials³⁹. Promising candidates to fulfill these conditions are nanocomposites⁴⁰, which consist of a polymer matrix and a nanoscale inorganic filler, which can be, for example, a spherical particle with a non-penetrable and smooth surface. As explained before, the grafting of polymer brushes on nanoparticles can stabilize dispersions of nanoparticles in homopolymer matrices. The explanations for the stabilizing effect of grafted polymers on nanoparticles dispersed in polymer melts were derived from theories initially developed for flat substrates. If the system is chosen in such a way that the polymer grafted on the surface is of the same chemical nature as the polymer melt wetting the surface, brush - matrix interactions are determined by entropy-driven forces⁴¹. For flat silicon surfaces with end-attached polystyrene brushes, Maas et al.¹ reported on a theoretical wetting diagram which shows two different wetting transitions (Figure 5). They indicate a first order wetting transition at low grafting densities and a second order wetting transition at high grafting densities. Green and Mewis⁷ were able to map out a similar phase diagram for a nanoparticle suspension experimentally. They chose PDMS-grafted silica spheres dispersed in a PDMS matrix with moderate grafting densities and low core volume fractions. Recent studies, complementing the work of Hasegawa and coworkers⁴², have shown that the thermodynamic wetting of a grafted polymer brush by an identical homopolymer melt is controlled by the degree of polymerization of the free chain (P) of the melt as well as by the grafting density (Γ) of the brush. At a constant chain length of the grafted polymer (degree of polymerization, N), the parameters (P , Γ) define the complete wetting region. This wetting region is a result of the enthalpic attraction provided by the grafted polymers on the free matrix chains. For a given chain length, the discontinuous (jumplike) first order transition at low grafting densities is called allophobic dewetting as it is caused by unfavorable polymer-substrate interactions. At high grafting densities the transition from complete wetting to incomplete wetting is gradual and thus associated to a second order transition called autophobic dewetting.

These transitions can be explained theoretically by calculating the Gibbs energy G of a homopolymer chain with molecular weight P in contact with a brush of molecular weight N . For a given grafting density the transition is a function of the ratio N/P . It is, however, clear that the brush conformation, i.e. a swollen or a contracted state, plays a crucial role in the mixing/demixing behavior of a suspension. If the brush is swollen by surrounding homopolymer chains these chains must somehow interpenetrate with the brush.

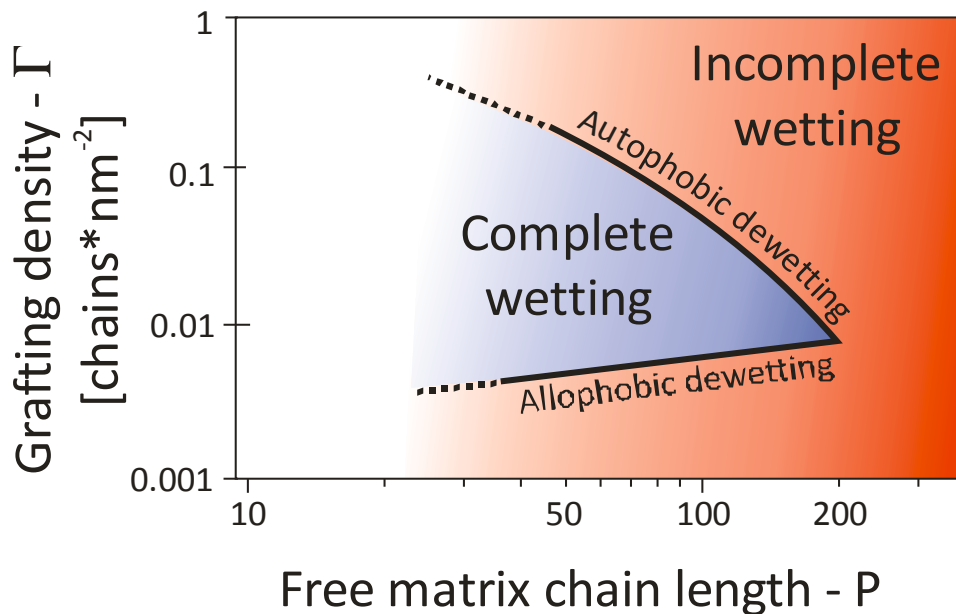


Figure 5. Theoretical phase diagram for a polymer brush ($N=200$) in contact with a chemically identical melt of linear chains.

The degree of interpenetration of the matrix chains will have an influence on the conformation of the brushes (Figure 6) and thus also an influence on the distance between neighboring particles. We considered a scenario with three different cases for the brush conformation in a system with high grafting density. a) Polymer-grafted nanoparticles without polymer matrix. The polymer brushes are contracted. Thus the distance between single particles should be minimal (Figure 6 a). b) Polymer-grafted nanoparticles dispersed in a homopolymer matrix with molecular weight comparable to that of the brushes ($N/P \approx 1$). The brushes should be swollen by the surrounding homopolymer chains thus inter-particle distance is increased (Figure 6b). c) Polymer-grafted nanoparticles dispersed in a homopolymer matrix with molecular weights higher than that of the brushes ($N/P < 1$). The homopolymer chains could not swell the brush anymore and thus aggregation should take place, leading to a reduced inter-particle distance (Figure 6c). The transition between the swollen and contracted state leading to demixing is referred to in the literature as the drying/interpenetration limit⁷. Considering the theoretical phase diagram of Green and Mewis (Figure 5), we see that at a grafting density, e.g. $0.7 \text{ brushes} \cdot \text{nm}^{-2}$, the transition between complete and incomplete wetting is predicted to take place at very low values of P . Although this phase diagram is constructed for a polymer brush with degree of polymerization $N = 200$, we may extrapolate the autophobic dewetting transition line. This would lead us to transition that would occur at a degree of polymerization for the matrix $P < 50$, which in turn for poly(ethyl methacrylate) (PEMA) corresponds to a molecular weight $< 6000 \text{ g/mol}$.

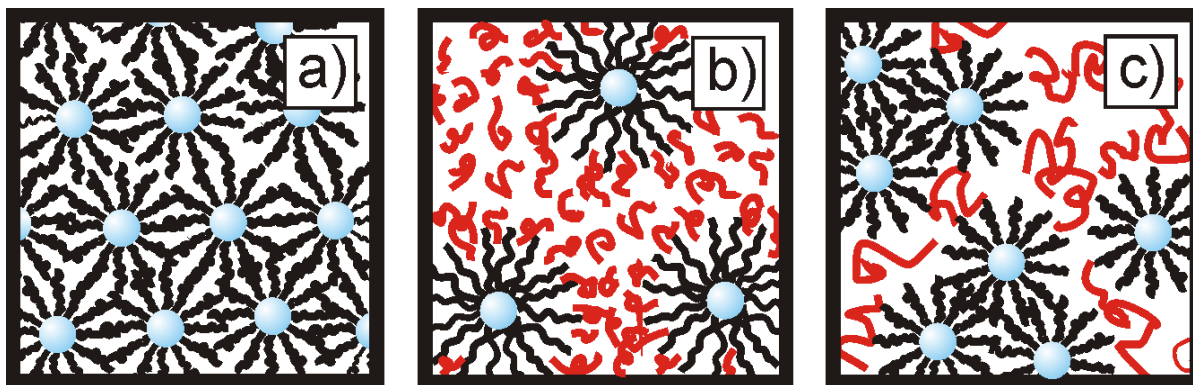


Figure 6. Influence of brush conformation on the distance between polymer-grafted nanoparticles: a) Without polymer matrix. b) With low molecular weight polymer matrix ($N = P$). c) With high molecular weight polymer matrix ($N/P < 1$).

In this work I show that the transition in the brush conformation between the swollen and contracted state can be inferred by means of quantitative measurements of the distance between neighboring particles. Furthermore, the role of the inter-particle distance is studied for the mechanical stability of nanocomposites. The attractive interaction between brushes in a contracted state and high molecular weight matrix is weaker (Figure 6c) compared to brushes swollen by low molecular weight matrix (Figure 6b). To check at which molecular weight the transition from complete wetting to partial wetting occurs in our system and to see if this transition is a function of the conformation of the brush (swollen, contracted), we prepared dispersions of PEMA-g- μ gels in homopolymers with different N/P ratio. As a first approach we imaged the surface of such samples with as scanning probe microscope and analyzed the distance between neighboring particles as a measure for the transition. The preparation of the silsesquioxane core particles and the principle grafting procedure to attach polymer brushes to such particles is reported in detail elsewhere^{36, 43}. However, the system used in this work involves a different monomer and thus the reaction conditions are different at some stages of the preparation routine. A system based on poly(ethyl methacrylate) (PEMA) with a much higher grafting density ($0.7 \text{ chains} \cdot \text{nm}^{-2}$) and a much higher molecular weight of the hairs was selected.

3. Experimental Methods to Investigate Physical Properties of Composites and its Constituents

In this chapter I will explain the experimental methods that I have employed to investigate the physical properties of the materials used for my thesis. I will start with the classic methods to analyze mechanical properties and measure the molecular weight distribution of polymers. This is followed by the description on how to determine the thickness of thin films and the size of particles. Before I go into detailed delineation of the methods, I want to point out some terms which are important in most of the explained techniques.

The **modulus** is a quantity which describes the viscous and elastic stresses and their relation to material properties through a factor of **stress** to **strain**. If the strain is applied parallel to the surface (Figure 7a) the modulus is called the **shear modulus** G .

$$G = \frac{\tau}{\gamma} = \frac{F/A}{\Delta x/L} = \frac{F \cdot L}{A \Delta x} \tag{3.1}$$

Here the shear stress τ is the ratio of the shearing force F applied to the area A of the specimen. The strain $\gamma = \Delta x/L$ is equal to the $\tan \theta$. Δx is the resulting transverse displacement and L the length of the specimen.

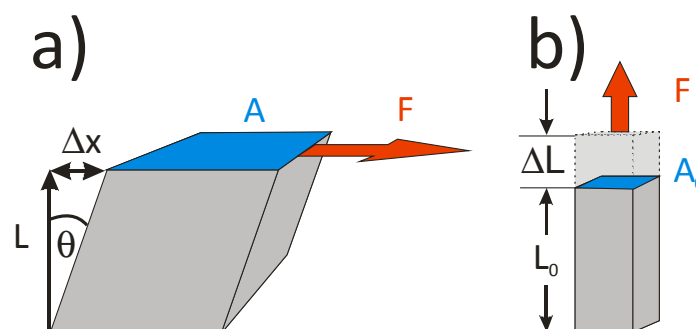


Figure 7. Stress applied to a specimen in a) shear and b) tension resulting in a shear strain and tensional strain respectively which is a measure of a body's change in shape.

If the stress is applied in tension or bending, the modulus is called the **Young's modulus** E (Figure 7b), where F is the force applied to the specimen, A_0 is the original cross-sectional area through which the force is applied, ΔL is the value by which the length of the specimen changes and L_0 is the initial length of the specimen.

$$E = \frac{\sigma}{\varepsilon} = \frac{F/A_0}{\Delta L/L_0} = \frac{F \cdot L_0}{A_0 \Delta L} \quad (3.2)$$

If we consider the specimen in (Figure 7b) to be an ideal spring and assume that its extension is in direct proportion with the load applied to it, according to Hooke's law we can write

$$F = -k \cdot \Delta L \quad (3.3)$$

where k is the spring constant.

3.1 Classic methods

3.1.1 Dynamic Mechanical Thermal Analysis (DMTA)

DMTA is a nondestructive method to mechanically characterize a variety of materials regardless of their physical state or form. The material may be a liquid with high or low viscosity in form of a paste, foam, dispersion or emulsion. It also can be solid with elastic or viscoelastic properties or containing fillers like particles or fibers. DMTA is rooted in the field of rheology which studies the deformation of a material in terms of elasticity and viscosity with instruments called rheometers. This is done by applying a defined strain to a sample while measuring the resulting stress at a certain temperature. Through Hooke's and Newton's laws the stress is related to the material properties elasticity and viscosity. The ratio of elastic stress to strain is called the elastic or storage modulus G' , while the ratio of viscous stress to strain is called the viscous or loss modulus G'' . The two moduli can be combined to a complex modulus $G^* = G' + iG''$ which reflects the contribution of both elastic and viscous components. If the strain is applied to the sample dynamically, e.g. with a sinusoidal oscillation (Figure 8a), strain and stress can be expressed like

$$\varepsilon = \varepsilon_0 \sin(\omega t) \quad (3.4)$$

$$\sigma = \sigma_0 \sin(\omega t + \delta) \quad (3.5)$$

where ω is the frequency, t the time and δ the phase lag between stress and strain. In purely elastic materials stress and strain are in phase ($\delta = 0$) whereby in purely viscous materials the strain lags the stress by a 90° ($\delta = \pi/2$) phase lag (Figure 8b). So the storage and loss modulus become

$$G' = \frac{\tau_0}{\gamma_0} \cos \delta \quad (3.6)$$

and

$$G'' = \frac{\tau_0}{\gamma_0} \sin \delta. \quad (3.7)$$

These complex numbers can be expressed in the form $G^* = G' + iG''$ where i is the imaginary unit with the property $i^2 = -1$.

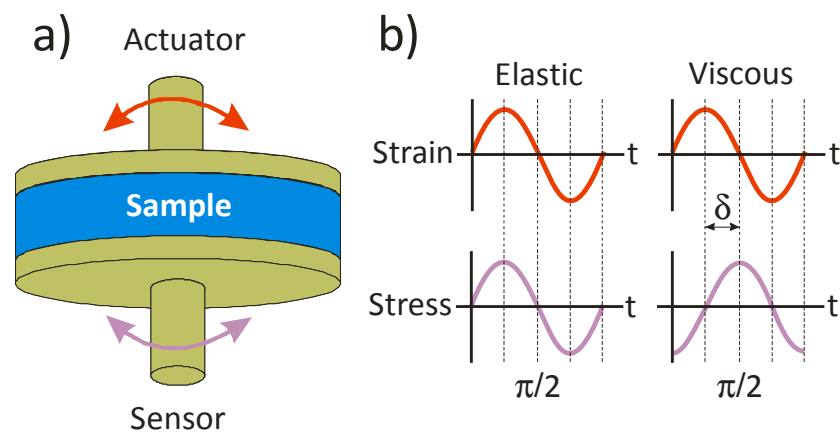


Figure 8. Schematic of a DMA experiment. a) The strain is applied to the sample via an actuator and the resulting stress is measured by a sensor. b) In purely elastic materials the applied strain is in phase with the stress while in purely viscous materials the stress lags the applied strain by $\pi/2$.

A material with both elastic and viscous properties exhibits a phase shift which is between 0 and $\pi/2$ and its damping behavior can be expressed as the tangent of the phase angle shift δ between the stress and strain vectors: $G''/G' = \tan \delta$. From equation (3.4) and (3.5) we can see that the moduli G and E vary with frequency. The physical reasons for these variations are the relaxation processes that take place when a polymer chain is deformed by external forces. In the glassy state an elastic response is observed at high frequencies (short times). In this region, the polymer lacks molecular mobility since no motion longer than a segment exists, so it maintains the disordered nature of a melt. Net movements of the chain backbone are impossible. At lower frequencies segmental movement becomes possible and segments of a few repeating units start to flow. As the frequency decreases further, parts of the polymer chain are able to change their position. This movement or rearrangement is called creep and takes place in the viscoelastic regime. When a stress is applied in

this regime the material creeps, which gives the prefix visco-. If the stress is released, the material fully recovers, which gives the suffix –elasticity. At very low frequencies, motion of entire chains takes place. This is called the viscous flow regime. The procedure used to determine the storage and loss moduli over a very broad frequency range is based on what is known as the time-temperature or frequency-temperature equivalence principle⁴⁴. It states that the viscoelastic behavior at one temperature (T_{ref}) can be related to that at another temperature (T) by a change in the timescale only. In other words, the temperature change is equivalent to the change of the deformation frequency of a given material. Typical rheometers are working in a frequency window of $\omega = 0.1-100$ rad/s. To cover the entire time range in which the above mentioned relaxation processes take place ($\sim 10^{-8}$ to $\sim 10^4$ s)⁴⁵, the temperature of the sample has to be varied. In this way a number of frequency dependent modulus curves according to (3.6) and (3.7) can be measured. From these measurements, a curve can be constructed by shifting the individual dynamic mechanical measurement curves measured at certain temperatures (Figure 9a) by a shift factor $a_T = \omega/\omega_{ref}$, relative to a reference temperature. The resulting curve is called the mastercurve (Figure 9b) which encompasses a huge frequency range of about 15-20 orders of magnitude.

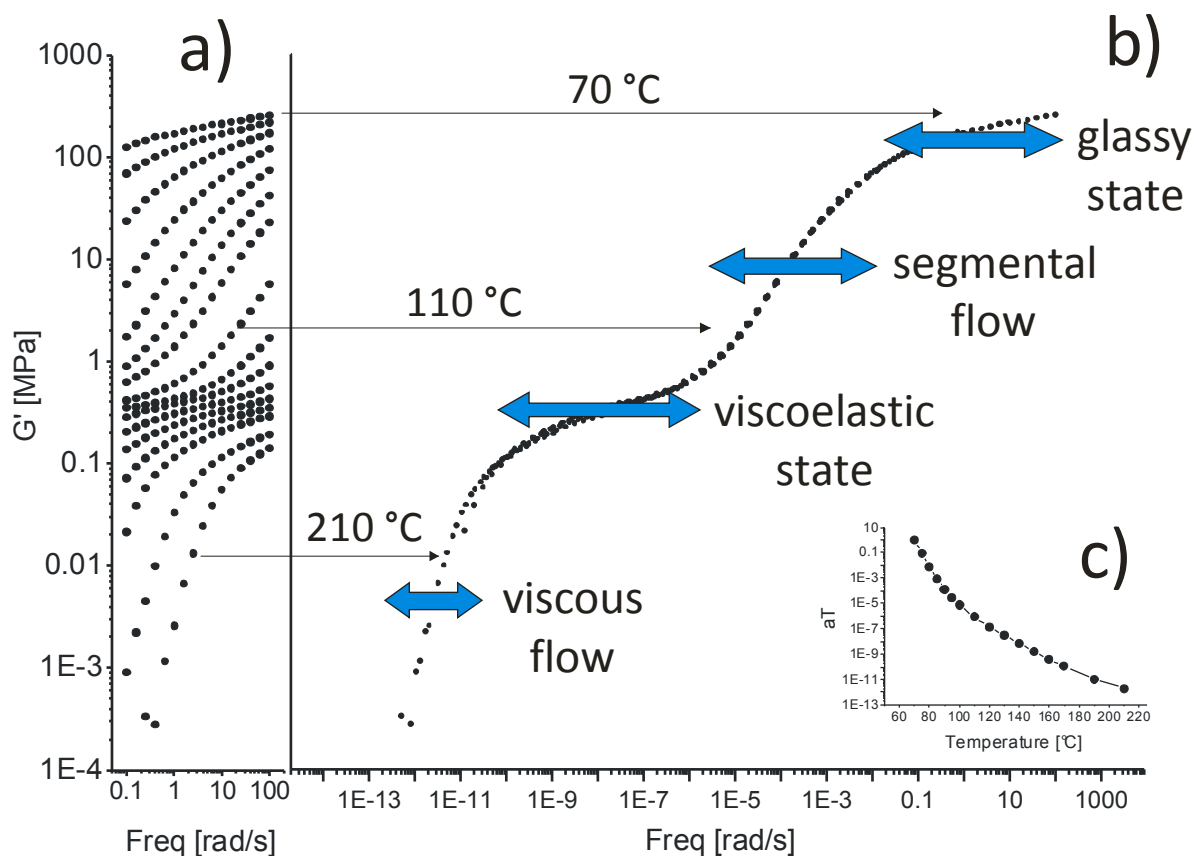


Figure 9. Individual dynamic mechanical measurements at certain temperatures of poly-(ethyl methacrylate) (a) can be superimposed by the time-temperature superposition principle to construct a mastercurve (b). For better visibility only the Storage modulus G' is shown. The shift factors a_T (c) are fitted with the WLF equation.

The relationship between the shift factors a_T and the temperature (Figure 9c) can be expressed by the WLF equation, which was postulated by Williams, Landel and Ferry⁴⁶

$$\log(a_T) = -\frac{C_1(T - T_{ref})}{C_2 + T - T_{ref}} = \log\left(\frac{\omega}{\omega_{ref}}\right) \quad (3.8)$$

where C_1 and C_2 are empirical constants adjusted to fit the values of a_T . Rearrangement of equation (3.8) leads to a useful expression of the WLF equation.

$$T = T_{ref} - \frac{C_2}{1 + \frac{C_1}{\log\left(\frac{\omega}{\omega_{ref}}\right)}} \quad (3.9)$$

With equation (3.9) it is possible to transform the mastercurve from a frequency dependent to a temperature dependent interpretation of the storage and shear moduli. Important values which describe the properties of the polymer can be extracted from the mastercurve.

1. In the viscoelastic regime we can determine the location of a plateau modulus G_N which reflects the unrelaxed, fully elastic response of the material corresponding to the flow transition.
2. The plateau modulus G_N is connected with the entanglement molecular weight M_e which is an important factor contributing to the unique physical properties of polymers.

The plateau modulus G_N can be obtained from the frequency where the minimum of the loss tangent ($\tan \delta$) is located by⁴⁷⁻⁴⁹ :

$$G_N = G'(\omega)_{\tan \delta_{min}} \quad (3.10)$$

and is directly connected with the entanglement molecular weight M_e via⁵⁰:

$$M_e = \frac{\rho_N \cdot R \cdot T_N}{G_N} \quad (3.11)$$

where ρ_N is the density of the polymer at the temperature T_N at which the plateau modulus is measured. R is the ideal gas constant ($R = 8.314 \text{ J} \cdot \text{mol}^{-1} \cdot \text{K}^{-1}$).

Setup used in this work

The DMTA measurements were performed using the Advanced Rheometric Expansion System (ARES, TA Instruments, Delaware, USA) in a parallel plate geometry. The studied materials were compress-molded as circular plates of 6 mm diameter and 1mm thickness. Before the measurements, isothermal strain sweeps at different temperatures were performed in order to separate the linear from the non-linear viscoelastic regimes. The shear deformation was applied with controlled deformation amplitude, which was kept in the range of the linear viscoelastic response of the studied materials. Frequency dependencies of the storage and the loss parts of the shear modulus have been determined from frequency sweeps measured within the frequency range 10^{-2} - 10^2 rad/s at various temperatures. Master curves for G' and G'' at a reference temperature have been obtained using the time-temperature superposition, i.e., shifting the data recorded at various temperatures only along the frequency coordinate.

3.1.2 Gel Permeation Chromatography (GPC)

Physical properties of polymers like the temperatures for transitions from solids to rubbers to liquids, e.g. glass transition temperature (T_g), depend on the molecular weight of the polymer. Furthermore, mechanical properties such as stiffness, strength, viscoelasticity, toughness, and viscosity of polymers also depend on their molecular weight. It is then obvious that also the molar mass distribution is of great importance. GPC, also referred to as size exclusion chromatography (SEC), is a widely used method to determine the molecular weight and the molar mass distribution of polymers.

By choosing different polymerization mechanisms, the molar mass distribution can be adjusted to achieve the desired properties of the polymer (Table 2). A polydispersity index (PDI) is defined as the quotient of weight average molar mass M_w and number average molar mass M_n ($PDI = M_w/M_n$) and describes the width of the molar mass distribution⁵¹.

Table 2. Polydispersity index for selected polymerization mechanisms⁵¹.

Polymerization method	PDI
Monodisperse Polymer (hypothetical)	1.00
Living Polymerization	1.01-1.05
Controlled Radical Polymerization	< 1.50
Radical Polymerization	1.50
Condensation Polymerization	2.00

GPC resembles high performance liquid chromatography (HPLC) forasmuch as a sample solution is pressed through columns filled with a porous material. Contrary to HPLC, the separation mechanism originates not from adsorption of molecules on the surface of the filler material, but ideally from size exclusion effects. During a GPC measurement the molecules are passing the pores of a solvent-swollen gel which fills the column. Because of the concentration gradient of the solvent-filled pores and the interspacing volume, polymer molecules can penetrate the pores. Depending on the size of the molecules they can either enter or not enter the pores. Molecules that can not enter the pores can not be separated at all and leave the column at first. Molecules with the ability to enter all pores leave the column without separation at the end of the measurement. This is called the separation threshold. The molecules with sizes in between the separation threshold are separated due to their hydrodynamic volume and will leave the column at different elution times. Typically, UV- or refractive index detectors are used to detect the mass-concentration of sample molecules in the eluent. Because GPC is a relative method to determine the molar mass of a polymer, calibration with well defined polymer standards is essential.

Setup used in this work

Analysis of all polymers used in this work was carried out at 20°C with a GPC set-up consisting of the following components: Waters 515 HPLC Pump, Waters WISP717 Autosampler, three Polymers Standard Service columns (SDV) in series (dimension: 300 x 8 mm, porosity: 500, 10⁵ and 10⁶ Å, respectively), filled with poly(styrene/divinyl benzene), and an ERC refractive index detector. Tetrahydrofuran, at a flow rate of 1 ml*min⁻¹, was used as an eluent. For calibration, low-polydispersity poly(methyl methacrylate) standards were applied.

3.1.3 Dynamic Light Scattering (DLS)

When a flashlight is pointed to a cloud of smoke, the light is scattered by the particles of the smoke and the cloud appears of a slight bluish color. This effect is known as the Tyndall effect and the intensity of the scattered light is determined by the size and shape of the particles. Similarly, the size and shape of particles or polymer chains in solution/dispersion can be determined by analyzing the scattered light. Two assumptions are required. First, the particles are assumed to be small compared to the wavelength and moving in Brownian motion were the probability density function of the position of a particle is expressed as⁵²:

$$P(x, t|0,0) = (4\pi D \cdot t)^{-3/2} e^{(-x^2/4D \cdot t)} \quad (3.12)$$

Here x is the position of a particle at time t . The temporal evolution of $P(x, t|0,0)$ is determined by the diffusion constant D of the moving particle. If the particle is a sphere with radius r , the Stokes-

Einstein relation connects the diffusion constant to the viscosity η of the solvent with temperature T and the Boltzmann's constant k_B by the equation⁵²:

$$D = k_B T / 6\pi\eta r \quad (3.13)$$

By using monochromatic and coherent laser light, time-dependent fluctuations in the scattered intensity due to the continuously moving particles can be observed. The dynamic information is then derived from an autocorrelation of the intensity trace recorded during the experiment. By using equations (3.12) and (3.13) the radius of a particle can be calculated. For polydisperse systems the autocorrelation is usually analyzed with the CONTIN algorithm developed by Steven Provencher⁵³. It should be noted that the radius r in equation (3.13) is not the effective radius of a hydrated particle in solution but the radius of a hard, perfect sphere which diffuses at the detected rate. It is also called the hydrodynamic radius (R_h) and is larger than the rotational radius of the particle, especially when the particle surface is modified with e.g. polymer brushes.

Setup used in this work

We determined the hydrodynamic radius (R_h), the size distribution of polymer-grafted-nanoparticles and the molecular weight of the neat nanoparticles by light scattering. The experiments were performed at room temperature (25 °C), using a commercial setup (ALV-5000, ALV GmbH, Germany). The samples of the neat particles and polymer-grafted-nanoparticles for DLS analyses were prepared by diluting the substances in toluene, yielding dilute dispersions of 1 to 0.1 g/l.

3.2 Methods to investigate thin films

The properties of thin films are of crucial interest for many applications in microelectronics, micromechanical sensing, data storage, as protective coatings and in biomedical applications. Herein the thickness of the film is the determining factor for methods applicable to measure the desired material properties. In the following I want to introduce the experimental methods and the theoretical background of the techniques used in my work. I will start with methods like ellipsometry and scanning probe microscopy. Then I will explain grazing incidence small angle X-Ray scattering (GISAXS). I will elucidate the use of micromechanical cantilever sensors (MCS) for the characterization of thin films and finally introduce the concepts of nanowear and wrinkling.

3.2.1 Scanning Probe Microscopy

The name Scanning Probe Microscopy (SPM) originates in the measurement principle of this method. A scanning probe could be the finger of a blind person reading the embossed letters of Braille line by line or the fine sapphire needle of a record player reading the audio track of the rotating vinyl disc. In

scanning probe microscopy, also referred to as atomic force microscopy (AFM), the probe is a small cantilever with a sharp tip at its end (Figure 10a, b). At the backside of the cantilever a laser is focused on the end of the cantilever itself. The reflected beam is sensed by a position sensitive detector (PSD). In a typical setup, the sample is moved under the tip in an x-y raster with a piezo-electric positioning system. Due to topographic features of the sample the cantilever is deflected and the deflection is sensed by the PSD (Figure 10c). In such a way a data stream of topographical information is produced. This stream is then used to construct an image of the scanned area. As will be explained later, other information about material properties can be also obtained.

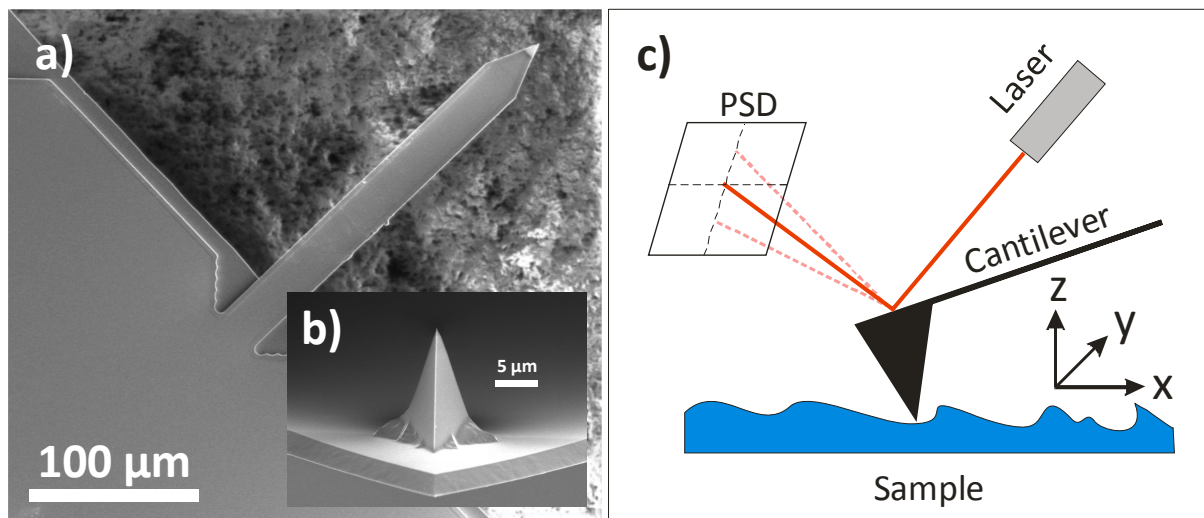


Figure 10. Typical SPM cantilever (a) for intermittent contact mode SPM with a sharp tip (b) at the end of the lever. The sample is moved under the tip and the topography is recorded by the reflected laser beam on a position sensitive detector (c).

Static and dynamic operation modes

In the static operation mode, the force between tip and sample is kept constant by using the cantilevers deflection as a feedback signal to adjust the z-position of the sample or the cantilever. For small deflections it can be assumed that the force F has a linear dependency to the deflection Δz given by $F = -k \cdot \Delta z$, where k is the spring constant of the cantilever. This mode is called the *constant force* or *contact mode* and is used to get topographical information of samples with a hard surface like metals or oxide films. The contact mode has two major disadvantages. (i) Due to frictional forces the tip wears off very fast. (ii) On soft surfaces such as polymers, even at very low forces in the range of a few nN, the wear leads to elastic and plastic deformation and/or disruption of the surface.

In the dynamic operation modes the cantilever is excited at or close to its resonance frequency ω_0 . In the so called *tapping* or *intermittant contact* mode, the vibration amplitude is used as a feedback parameter to measure the topography of a sample. To describe the dynamical behavior like frequency and amplitude of the vibrating cantilever we can use Newton's equation of motion.

$$m^* \frac{d^2 z(t)}{dt^2} + \gamma_D \frac{d z(t)}{dt} + k \cdot z(t) = F_{ts} + F(t) \quad (3.14)$$

were m^* is the effective mass of the cantilever with thickness h , width w , length L and density ρ ($m^* = 0.2427 \cdot w \cdot h \cdot L \cdot \rho$). γ_D is the damping coefficient and k the spring constant. The oscillatory movement is driven by a normal force $F(t)$. As a first approximation by neglecting the tip-sample interactions F_{ts} , equation (3.14) can be solved in steady state by inserting a periodic excitation $F(t) = F_0 \sin(\omega t)$ to

$$z(t) = z_0 \sin(\omega t + \varphi) \quad (3.15)$$

with an amplitude z_0 of

$$z_0 = \frac{F_0/m^*}{\sqrt{(\omega_0^2 - \omega^2)^2 + (\omega\omega_0/Q)^2}} \quad (3.16)$$

In equation (3.16) the angular resonance frequency of the cantilever $\omega_0 = \sqrt{k/m^*}$ and the quality factor $Q = \omega_0/\gamma_D$ which describes the relative width of the resonance peak are introduced. The phase shift can be expressed in terms of

$$\tan \varphi = \frac{\gamma_D \omega}{k - m^* \omega^2} \quad (3.17)$$

From (3.16) and (3.17) we can see that the amplitude and the phase shift depend on the angular frequency^{54, 55}. Let us now consider that the cantilever is far away from the surface. It oscillates with a “free” angular resonance frequency ω_0 and an amplitude z_0 . Close to the surface the oscillation is influenced by additional tip-sample forces F_{ts} . In sum, F_{ts} and γ_D can damp the oscillation resulting in a damped resonance angular frequency $\omega_D = \omega_0 \left(1 - \frac{1}{2Q^2}\right)^{1/2}$ and an amplitude z_D . By scanning over the surface we can use the amplitude information as a feedback to construct the topography image and in addition material property changes can be mapped by recording the phase shift between driving force and the tip oscillation φ . The phase shift is a very elegant way not only to obtain topographical information of the surface but also to distinguish regions with similar topography but different material properties like elastic or shear modulus.

Setup used in this work

The characterization and the imaging of all samples in this work, was carried out with a commercial SPM setup (Dimension 3100, Veeco, USA), unless otherwise indicated. Silicon cantilevers (OMCL-AC 160 TS, Olympus, Japan) with a nominal tip radius of ~ 10 nm and a tip height of 11 μm were used. The measurements were done in tapping mode with a resonant frequency of the cantilevers near 300 kHz.

3.2.3 Grazing Incidence Small angle X-ray Scattering (GISAXS)

Since the theory of scattering of electromagnetic waves can be applied to all wavelengths, visible light, X-ray photons, neutrons or electrons can be used as probing species in scattering experiments according to the length scales of interest and the sample properties. Any scattering process is characterized by a reciprocal law, which gives an inverse relationship between scattering angle and particles size.

Since X-rays are primarily scattered by electrons, small angle X-ray scattering (SAXS) is observed when electron density fluctuations of colloidal size exist in the sample where the electron density is represented by the square of the wave function Ψ^2 . These fluctuations from 1 nm to 1 μm in size are measured in terms of scattered intensity as a function of incident angle α_i , volume fraction, contrast, the shape and the size distribution of the scattering bodies in a SAXS configuration. To achieve measurable signals, the contrast, which is the electron density difference between the scattering bodies and the matrix, has to be sufficiently high. To visualize the scattering process we consider a simple example of a small spherical particle (Figure 11a). Waves that are scattered at the indicated points by an angle of 2θ have a path difference of 1λ . If the scattering at all points within the sphere is considered, it is obvious that no scattering will occur in the direction of 2θ when we superimpose waves with all possible phases because of destructive interference. If smaller scattering angles are taken into account, the phase differences become smaller and the waves start to amplify each other, so that a scattering maximum will be observed in the direction of zero scattering angle, because here all waves are in phase. Qualitatively the scattering curve has a shape as the illustrated curve 1 in Figure 11c. In a much bigger sphere, phase shifts of 1λ will already occur at smaller scattering angles for the same wavelength of the incident wave (Figure 11b). This leads to a narrower scattering curve (Figure 11c, curve 2) and finally, for particles that are huge compared to the incident wavelength, small angle X-Ray scattering is observed (Figure 11c, curve 3).

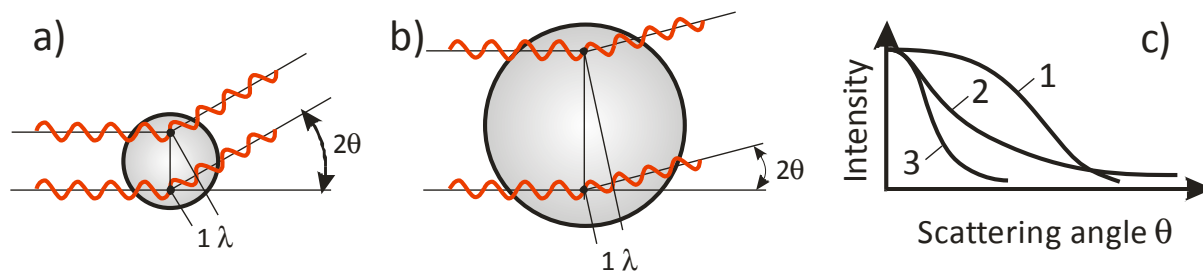


Figure 11. Scattering of waves at particles of different size. a) A small particle, b) a large particle compared to the wavelength of the incident waves. c) Qualitative shape of scattered intensities. Modified figure taken from⁵⁶.

Pursuing the above developed train of thoughts, it is possible to calculate the expected scattering curves for any particle. Therefore, the electron distance distribution function $p(r)$ needs to be considered. The electron distance distribution represents the likelihood of finding the electron in an orbital at any given distance r away from the nucleus. It is typically expressed by the radial distribution function. For s-orbitals, the radial distribution function is given by $p(r) = \Psi^2 4\pi r^2$. In general, the scattering curve I is obtained by Fourier inversion of $p(r)$.

$$I(\vec{h}) = 4\pi \int_0^\infty p(r) \frac{\sin \vec{h}r}{hr} \cdot dr \quad (3.18)$$

Here \vec{h} is the scattering vector which will be derived in the following. Let us suppose a similar situation as depicted in Figure 11. We denote the direction of the incident beam as the unit vector \vec{s}_0 and the direction of the scattered beam by \vec{s} (Figure 12).

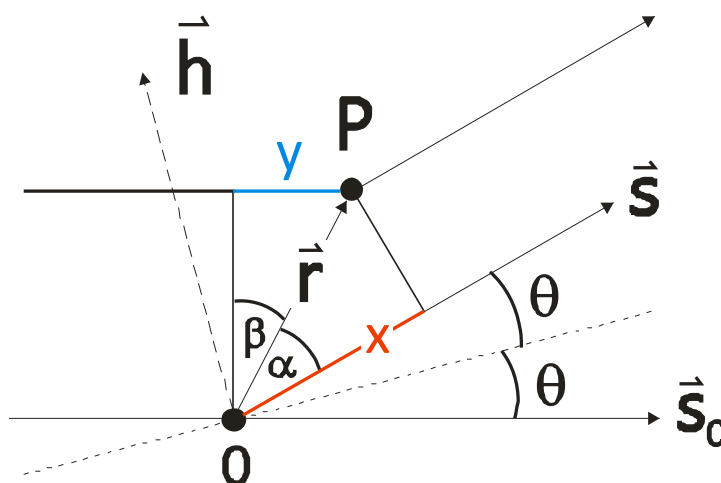


Figure 12. The scattering of waves at two points and the resulting scattering vector h .

The path difference of a point P , assigned by the vector \vec{r} , against the origin O is given by $x - y = r \cdot \cos \alpha - r \cdot \sin \beta$. Multiplying the unit vectors and transforming into a dot product leads to $-\vec{r}\vec{s} + \vec{r}\vec{s}_0 = -\vec{r}(\vec{s} - \vec{s}_0)$. Since the phase φ is $2\pi/\lambda$ times the difference between the optical path and some arbitrary reference point, the phase can be derived as $\varphi = -(2\pi/\lambda)\vec{r}(\vec{s} - \vec{s}_0)$ which takes

the form $\varphi = -\vec{h}\vec{r}$. $(\vec{s} - \vec{s}_0)$ lies symmetrically on the angle bisector of the incident and the scattered beam and its magnitude is $2 \sin \theta$. Consequently \vec{h} has the same direction as $(\vec{s} - \vec{s}_0)$ and its magnitude is

$$\vec{h} = \frac{4\pi \sin \theta}{\lambda} \quad (3.19)$$

By considering only constructive interference and substituting Bragg's law ($n\lambda = 2d \sin \theta$) into equation (3.19), where d is the distance between scattering centers, \vec{h} is reduced to

$$\vec{h} = \frac{2\pi}{nd} \quad (3.20)$$

So far, we have only considered the case of scattering of an isolated particle which was postulated by Guinier⁵⁷ in the early 19th century (Figure 13a). If the sample consists of monodisperse, sufficiently dilute solutions, the scattered intensities simply add up⁵⁶ (Figure 13b). The task in small angle X-Ray scattering consists of deducing the size, shape or electron density distribution from the scattering curve. This task is known as the inverse scattering problem which is the problem of determining the characteristics of an object from measured data. However, there is one parameter which can be easily deduced from the scattering curve of dispersed particles, that is the interparticle distance. Similar to the diffraction pattern produced by diffraction of light through a slit with spacing d , we can deduce the interparticle distance from small angle X-Ray scattering curves. At a scattering vector \vec{h} , where the intensity has a maximum we apply equation (3.20) to calculate d .

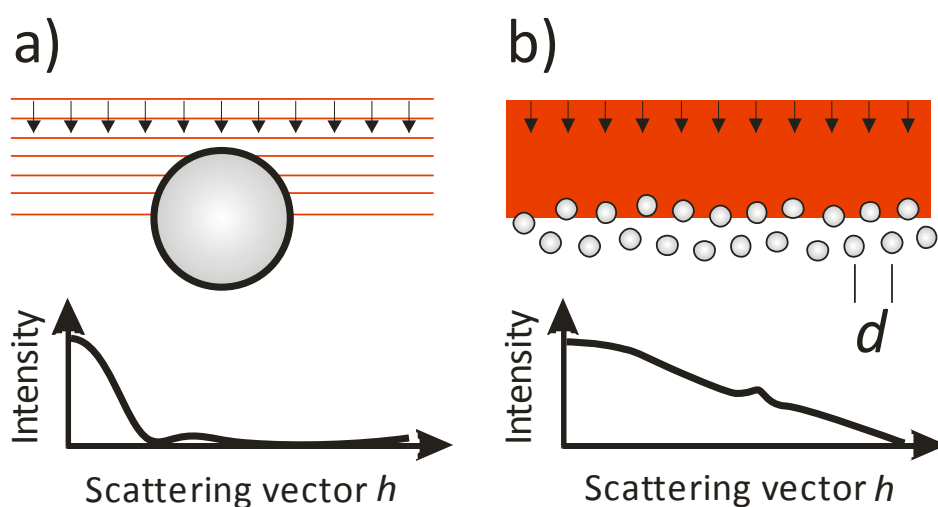


Figure 13. Schematic intensity profiles for scattered X-Ray beams at small scattering angles. a) Scattering at a single particle. b) Scattering at many, monodisperse particles.

However, SAXS is usually done in transmission geometry which limits its application to samples with a sufficiently high amount of scattering bodies and small substrate thicknesses. When the sample is aligned in grazing-incidence geometry (Figure 14), the analysis of thin films on thick substrates becomes possible.

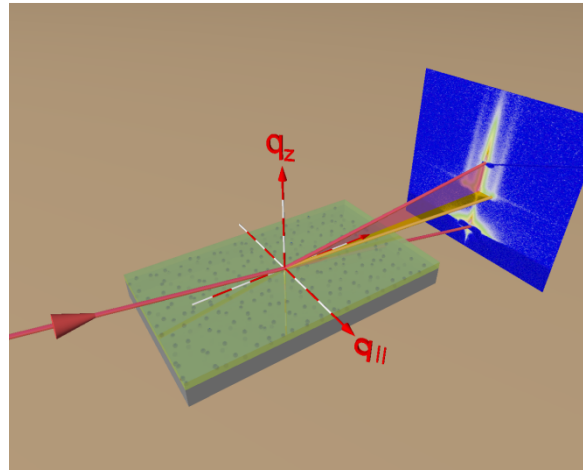


Figure 14. Small angle X-ray scattering setup in grazing incidence geometry. The incidence is coming from the right and is reflected (red) and refracted (orange) at the surface of the sample which contains nanoparticles and the substrate. The scattered intensity is represented as an intensity map in the scattering plane.

In order to understand the scattering patterns gathered in a GISAXS geometry, some examples are given in Figure 15. If the sample consists of lamellae that are oriented parallel to the surface plane, the scattering is represented by stripes of high intensity at equidistant spacing along the q_z direction (Figure 15a). These stripes in the diffuse reflectivity are referred to as Bragg sheets. If the lamellae are oriented perpendicular to the surface plane, the signature is correlation peaks parallel to the interface of the lamellae, with a rod-like shape normal to the surface (Figure 15b). If the sample consists of partially ordered or disordered lamellae, the scattering pattern contains rings or partial rings of high intensity (Figure 15c).

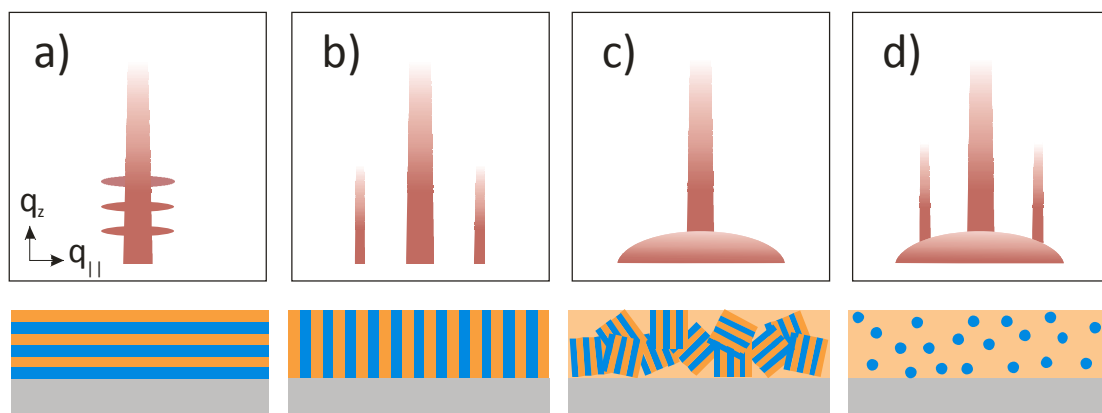


Figure 15. GISAXS scattering patterns for exemplary orderings inside a sample. The intense specular reflection from the surface is omitted. a) Lamellae parallel to the surface. b) Lamellae perpendicular to the surface. c) Tilted lamellae and d) dispersed particles. Modified figure take from⁵⁸.

If the incident beam is aligned at the critical angle for total external reflection $\alpha_i = \alpha_c$ it is reflected and refracted primarily at the substrate. The refracted beam travels along the surface of the substrate and the film and thus holds information of the film structure (Figure 14). In the scattering plane the GISAXS intensity distribution corresponds to a detector scan in diffuse Reflectivity. The intensity distribution parallel to the surface plane corresponds to a line cut through the corresponding transmission SAXS pattern.

By analyzing the full GISAXS intensity map one can extract lateral and normal density correlations which, for example, give information about the distribution of nanoparticles in a polymer matrix. This makes GISAXS a nondestructive, versatile tool to characterize nanocomposite materials especially as thin films.

Setup used in this work

The GISAXS experiments were done at the BW4 beamline of the HASYLAB @ DESY using the μ -focus option. We operated the experiments at a sample to detector distance of 2.0 m, a wavelength of $\lambda = 0.138$ nm and a beam size of $32 \times 17 \mu\text{m}^{59, 60}$ (horizontal x vertical). For our experiments an incident beam angle of $\alpha_i = 0.7^\circ$ was chosen. We performed transverse detector scans of the full 2D scattering pattern in reciprocal scattering plane ($q_{||}$) to extract the scattering curves. The transverse cuts were carried out at the maximum intensity of the Yoneda peak ($\alpha_c = 0.19^\circ$)⁶¹. We deduced the correlation length of our samples from the position of the correlation peak in the scattering curves. The error was given by the full width half maximum (FWHM) of the peak.

3.3. Theory of cantilever mechanics

The equation which describes the motion of an oscillating cantilever with an external applied force F as a time (t) dependent deflection z at point x along the cantilever length L is given by⁶².

$$EI \frac{\partial^4 z(x, t)}{\partial x^4} + \frac{m}{L} \cdot \frac{\partial^2 z(x, t)}{\partial t^2} = F(x, t) \quad (3.21)$$

Herein m is the mass of the rectangular beam of width w and height h with an elastic modulus E and a moment of inertia I . By solving equation (3.21) the corresponding Eigenfrequencies f_n are given by

$$f_n = \frac{\lambda_n^2}{2\pi L^2} \sqrt{\frac{EI}{\rho A}} \quad (3.22)$$

where ρ is the density and A the cross-sectional area of the beam. λ_n is the n^{th} Eigenvalue ($n = 1, 2, 3 \dots$) which satisfies the condition $\cosh \lambda \cdot \cos \lambda + 1 = 0$. The first three values for λ are 1.875, 4.694

and 7.855. For higher order modes n , the very accurate approximation $\lambda \cong \pi \left(n - \frac{1}{2} \right)$ may be used. Let us now consider a bar consisting of two materials with an elastic modulus E_1 and E_2 as well as a moment of inertia I_1 and I_2 (Figure 16a). By using a combination of $E_1 I_1$ and $E_2 I_2$ we can write equation (3.22) as⁶³

$$f_n = \frac{\lambda_n^2}{2\pi L^2} \sqrt{\frac{E_1 I_1 + E_2 I_2}{\rho_{mean} \cdot A_{1,2}}} \quad (3.23)$$

where $\rho_{mean} = \frac{\rho_1 \cdot h_1 + \rho_2 \cdot h_2}{h_1 + h_2}$ is the average density of the composite beam. $A_{1,2}$ is the cross-section of the composite beam.

By taking the shift of the neutral axis h_n into account we can derive I_1 and I_2 for the individual layers as

$$I_1 = \frac{w}{3} [h_n^3 - (h_n - h_1)^3] \quad (3.24)$$

and

$$I_2 = \frac{w}{3} [(h_n - h_1)^3 - (h_n - h_1 - h_2)^3] \quad (3.25)$$

The position of the neutral axis can be expressed as

$$h_n = \frac{1}{2(E_1 h_1 + E_2 h_2)} \cdot (E_1 h_1^2 + 2E_2 h_2 h_1 + E_2 h_2^2) \quad (3.26)$$

A typical geometry for a composite beam made of two materials is given in Figure 16a. Herein the cantilever is denoted with the subscript 1 and the coated material is denoted with the subscript 2.

Microcantilevers used in this work

The microcantilevers (Octosensis, Micromotive GmbH, Mainz, Germany) which were used in this work consist of an array of eight silicon cantilever bars attached to a chip (Figure 16b). The cantilevers were 500 – 1000 μm long and had a thickness between 0.7 – 5.0 μm . Within one chip the thickness variation is < 1%.

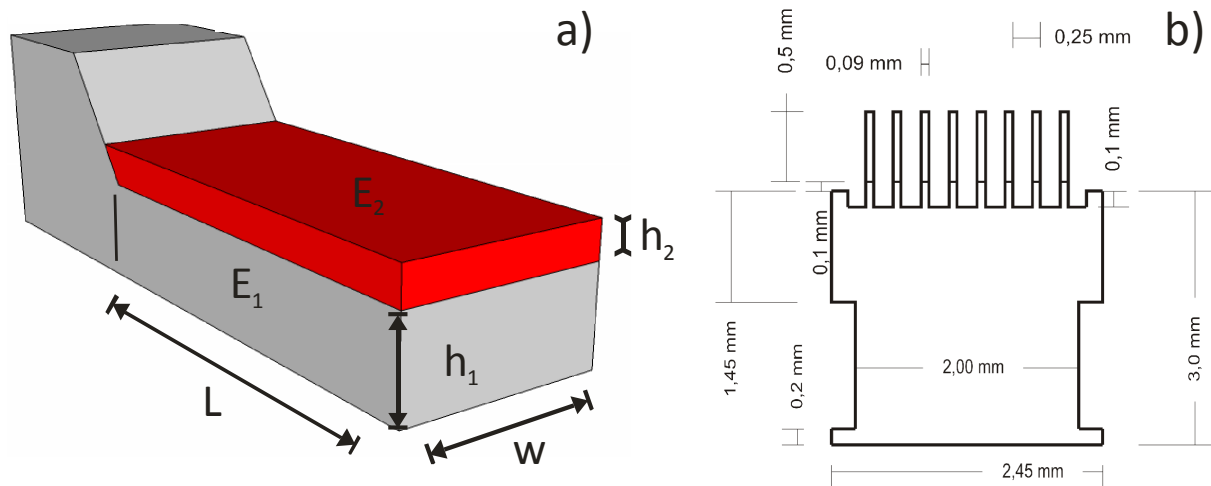


Figure 16. a) Geometry of a coated cantilever sensor with of length L and width w . The cantilever consists of a material with elastic modulus E_1 and height h_1 , while the coating of height h_2 has an elastic modulus E_2 . b) Dimensions of a typical micromechanical cantilever array consisting of eight cantilever bars.

3.4. Inkjet printing of polymeric solutions

Devices for printing text or digital images on sheets of paper are nowadays the standard equipment of offices and also gained big markets in private consumer products. The inkjet printing technique was first developed in the early 1950 and got further improved mainly by Canon, Epson and Hewlett-Packard. However, in the past years engineers and scientists have invested much effort to design inkjet printing devices for industrial and scientific deposition processes⁶⁴.

In principle the technique is based on the ejection of liquid ink drops through a fine jet nozzle. In most consumer printers the ejection of the ink is carried out via a thermal impulse which causes a rapid pressure increase inside a tiny ink chamber. In inkjet printers used for material deposition in science and technology the ejection is typically achieved with piezoelectric devices.

Setup used in this work

To print polymer solutions onto cantilever sensors we used a Nano-plotter NP 2.0 (GeSIM, Grossmerkmannsdorf, Germany). The setup mainly consists of a mobile pipet dispenser which is driven by step motors with a precision of $\pm 10 \mu\text{m}$ (Figure 17a). The dispenser is equipped with a piezo-driven micro nozzle (Nano-Tip) which produces drop volumes from 10 to 50 nL (Figure 17b). The drop volume, the ejection speed and ejection frequency can be adjusted by tuning the electric signal of the piezocrystal of the Nano-Tip. The software provided by the manufacturer allows a fully automated operation of the system. In addition, manual guiding of the drop position is possible. The respective drop position can be defined in a live image provided by a video microscope. The video assisted drop positioning is suitable for more complex substrates, like microcantilever arrays.

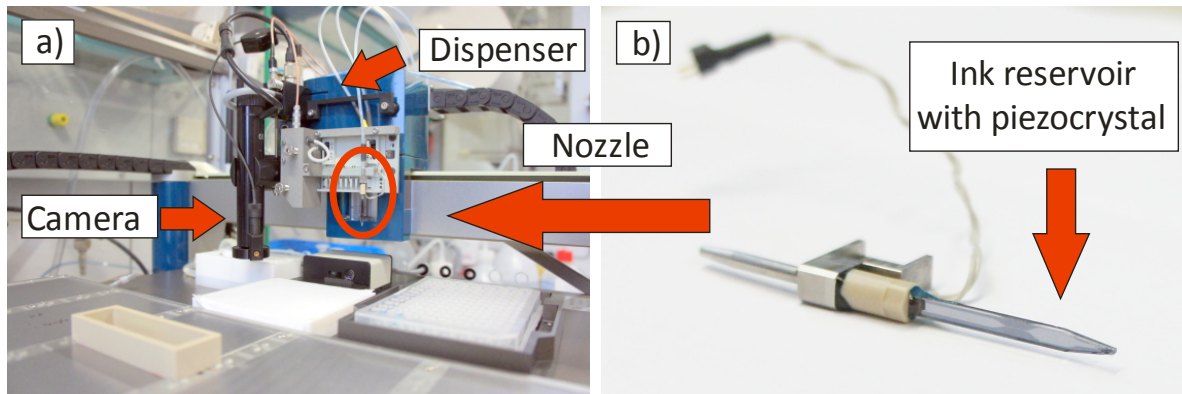


Figure 17. a) Nano-Plotter NP 2.0 with pipet dispenser and microscope camera for position control. b) The piezo driven Nano-Tip nozzle with a small ink reservoir.

3.5. Finite Element Method (FEM) with ANSYS

To calculate the physical behavior of a structural element, self-consistent solutions are available to calculate e.g. the displacement Δx of a cantilever (Figure 18a) similar to equation 1).

$$\Delta x = \frac{FL^3}{3EI} \quad (3.27)$$

When the geometry is more complex, e.g. a simple structured L-braked (Figure 18b), there are no self-consistent solutions and the above mentioned approach can not be applied. The basic concept in FEM is therefore to divide a complex geometry into discrete small parts (Figure 18c). These parts are called **elements** and their deformation can be described individually. The individual solutions are then summed up to get the solution for the whole geometry. The individual elements are connected via knots, i.e. points at the vertices of the elements. Each knot has 3 degrees of freedom (u_x , u_y , u_z) which describes his movement in space.

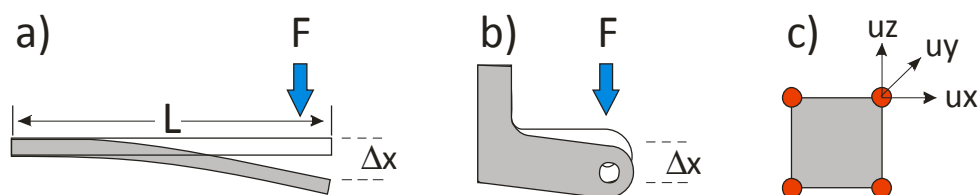


Figure 18. a) Displacement of a simple cantilever due to an applied load. b) For more complex geometries the displacement can not longer be described with self-consistent solutions. c) Therefore the geometry is divided into discrete elements.

By assuming equations for the displacement u , e.g. a linear equation ($u(x) = a \cdot x + b$), the software computes the equation of motion of a structure⁶⁵.

$$[M] \cdot \{\ddot{u}\} + [C] \cdot \{\dot{u}\} + [K] \cdot \{u\} = \{F\} \quad (3.28)$$

Herein M is the inertia matrix, C is the damping matrix and K is the stiffness matrix. For a given applied load F , equation (3.28) can be solved by iterative methods. The time which is needed for the computation of (3.28) depends on the number of elements which are “*meshed*” over the geometry. If the solution of (3.28) is known, all other physical values like stress, resonance or restoring forces can be derived.

3.5.1 Modal analysis

Resonant vibration is mainly caused by an interaction between the inertial and elastic properties of the materials within a structure. To better understand any structural vibration problem, the resonant frequencies of a structure can be analyzed with finite element methods. Modal analysis has become a widespread means of finding the modes of vibration and the resonance frequencies of structural elements and arbitrary geometries.

The modes of a structure describe their inherent properties which are determined by material properties like mass, damping, stiffness/rigidity and boundary conditions. Each structure has an infinite number of modes which are defined by a resonance frequency and a mode shape. To calculate the resonance frequency and the mode shape we can make use of the concept of single-degree-of-freedom systems (SDOF).

A SDOF system is mathematically described similar to equation (3.14) and (3.28) as:

$$m\ddot{u}(t) + c\dot{u}(t) + ku(t) = f(t) \quad (3.29)$$

where m , c and k are the mass, the damping coefficient and the spring constant respectively.

Transforming equation (3.29) to the Laplace domain $F(s) = \mathcal{L}\{f(t)\}$ and assuming zero initial conditions yields:

$$Z(s) \cdot U(s) = F(s) \quad (3.30)$$

with s being the complex number $s = \sigma + i\omega$ and $Z(s) = ms^2 + cs + k$ the dynamic stiffness. The transfer function $H(s)$ between displacement u and force F , $U(s) = H(s) \cdot F(s)$, equals the inverse of the dynamic stiffness

$$H(s) = \frac{1}{ms^2 + cs + k} \quad (3.31)$$

Since the roots of the denominator of the transfer function are the poles of the system, for small damping coefficients we get $\lambda = -\sigma \pm i\omega_d$ with $f_d = \omega_d/2\pi$ as the damped resonance frequency

and a damping ratio $\xi = \frac{c}{2m\omega_n} = \sigma/|\lambda|$ for the undamped resonance frequency $\omega_n = \sqrt{k/m} = |\lambda|$. The properties of a more complex multiple-degree-of-freedom (MDOF) system, given by equation (3.28), can always be represented as the linear superposition of a number of SDOF characteristics⁶⁶.

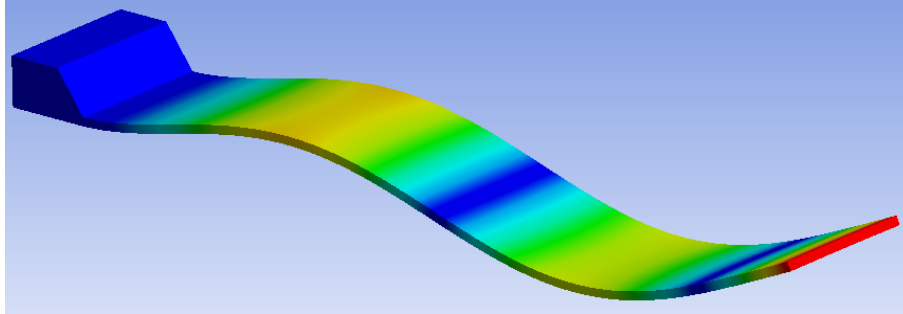


Figure 19. Result of a modal analysis of a cantilever geometry. The image shows the shape of the second resonance mode where displacements are indicated with a color map.

The FEM modal analysis is therefore a convenient way to simulate the mechanic behavior of coated cantilevers (Figure 19) and offers the possibility to identify critical parameters of the coating process. Once the geometry is designed, most parameters like film thickness, elastic modulus and film homogeneity can be iterated to find best results or to fit them to experimental data.

Software used in this work

To simulate the resonance frequencies of the cantilevers used in this work we employed the ANSYS DesignSpace software package. The iterations of the parameters were done using the ANSYS Workbench 12.1 on a HP-Workstation xw4600.

4. PEMA-g- μ gels and Dispersions with like Homopolymers

4.1 Preparation of PEMA matrix polymers

The matrix PEMA polymers were prepared according to Ramakrishnan et al.⁶⁷ in 50 vol-% anisole solution at 32°C. Polymers with a molecular weight > 200 kg/mol were prepared by living anionic polymerization. In this case we used sec-buthyllithium/1,1-diphenylethylene in THF at -70°C as the initiator system. MeOH was chosen for termination. The PEMA homopolymers were produced in a controlled fashion as indicated by the narrow polydispersity index. The molecular weight in all cases was above the entanglement regime ($M_e \approx 10\text{ k g}^*\text{mol}^{-1}$)⁶⁸.

Table 3. Polymer characteristics for PEMA matrix homopolymers

Abbr.	M_w [g/mol]	PDI [M_w/M_n]	Tg [°C]
12k	11700	1.20	68
15k	14600	1.22	68
19k	18600	1.15	67
36k	36400	1.12	69
75k	75400	1.14	73
98k	98400	1.23	72
101k	100900	1.21	73
140k	139800	1.27	78
178k	177800	1.28	83
269k	269200	1.11	87

4.2 Cleaving of the grafted PEMA-chains

In order to analyze the PEMA brushes by GPC, the core of the nanoparticles was dissolved with hydrofluoric acid. Dissolution was accomplished adapting a procedure described by Marutani et al.⁶⁹ for PMMA-brushes and modified to work for PEMA brushes too. In a poly(ethylene) flask 80mg of the PEMA-g- μ gel particles were dispersed in 10 ml of Toluene by means of 10 min ultrasonification and

90 min vigorous stirring. 0.7 g of the phase transfer catalyst Aliquat 336 (Alfa-Aesar) and 3 ml of 5 wt-% HF were added. During two hours of stirring the cores were dissolved. Stirring was stopped and the aqueous layer was allowed to separate from the organic layer. The aqueous layer was removed from the bottom of the flask using a syringe and discarded after neutralization. The organic layer containing the PEMA was stirred with 20 ml of a saturated aqueous solution of NaHCO_3 to neutralize residual HF. In a separating funnel the organic phase was separated and subsequently concentrated under reduced pressure. The polymer was precipitated in a mixture of 8/2 ml of MeOH/Millipore water, filtered (G2 glass filter crucible) and dried in a vacuum.



Figure 20. Cleaving the PEMA-brushes from the μ gel-particles with a phase-transfer catalyst Aliquat 336.

4.3 Characterization of the cleaved PEMA-chains

Because the interaction between matrix polymer and grafted polymer brushes depends on their molecular weights, the determination of brush molecular weight was essential. Dissolution of the μ gel particles with HF was carried out and the free polymer recovered and subjected to GPC measurements (green dash-dotted curve, Figure 21). This result was compared to the GPC-results of the μ gel particles (black dashed curve) and the PEMA-g- μ gels (red solid curve).

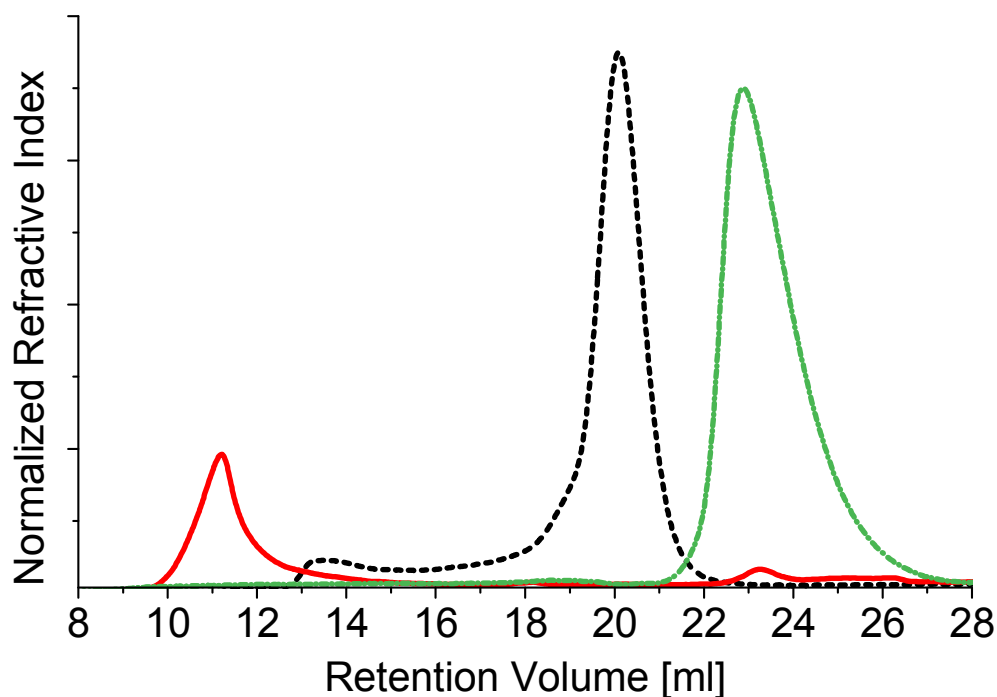


Figure 21. Representative GPC-results for the μ gel-particles (black dashed line), the PEMA-g- μ gels (red solid line), and the cleaved PEMA brushes (green dash-dotted line).

The size of the particles increased after polymerization is represented by a decrease in retention volume from 20 ml to 11 ml due to the addition of the polymer brushes. Dissolution of the core with diluted HF gave “free” PEMA with a retention volume of 23 ml. From the retention volume of the free PEMA we estimated the number average molecular weight $M_n = 26100$ g/mol, a mass average molecular weight of $M_w = 37700$ g/mol and the polydispersity index $PDI = 1.45$ of the PEMA brushes, (by comparing the data with a PMMA standard with known M_n and PDI) after cleaving them from the μ gel-particles. In conclusion, the GPC-data confirmed the successful grafting as well as the cleaving of the brushes.

Several questions arise when looking in detail at the GPC. The GPC curve of the particles (black, dashed) has a shoulder at lower retention volume. A reason for this shoulder could be the presence of aggregates. The GPC curve of the core-shell particles (red, solid) has a second, but much smaller peak at a higher retention volume, comparable to that of the cleaved polymer (green, dash-dotted). This peak is attributed to the formation of unbound polymer during polymerization. Thus we concluded that the polymer in solution grew to the same length as the polymer on the surface of the particles. For the measurement of the cleaved polymer the question arises as to why we observed a PDI of 1.45 in GPC. This was unusually high for a controlled reaction and could result in an elevated polydispersity of the PEMA-g- μ gels. An explanation could be that the HF-treatment hydrolyzed some of the ester groups. In order to support the success of the synthesis and our hypothesis from GPC data, we have performed DLS and SPM measurements of μ gel-particles and PEMA-g- μ gels.

4.4 Characterization of individual particles

4.4.1 Determination of grafting density

Besides the molecular weight of immobilized chains and the size of the filler μ gel-particle, the grafting density of grafted PEMA can be estimated by using the following equation

$$\Gamma = \frac{n(\text{PEMA})}{n(\mu\text{gel}) \cdot \text{particle surface}} \quad (4.1)$$

where $n(\text{PEMA}) = 1.12 \cdot 10^{-7}$ mol and $n(\mu\text{gel}) = 1.5 \cdot 10^{-10}$ mol were obtained by TGA⁷⁰. The particle surface (1018 nm^2) was calculated from SPM measurements of the μ gel-particles (shown later). We calculated a grafting density of $\Gamma = 0.7$ brushes $\cdot\text{nm}^{-2}$.

4.4.2 Dynamic Light Scattering

To clarify if the presence formed aggregates, as indicated by the shoulder in the GPC curve, we performed dynamic light scattering on the μ gel-particles and the PEMA-g- μ gels. The hydrodynamic radius of the μ gel-particles ($R_{h(\mu\text{gel-particles})}$) was determined by the average value of the data obtained from five different scattering angles (30° - 150° in steps of 30°). The measurement resulted in a hydrodynamic radius $R_{h(\mu\text{gel-particles})}$ of 14 ± 1 nm. The error is the standard deviation of the mean value obtained from 5 scattering angles. After the “grafting from” of the PEMA chains we found an increase in the hydrodynamic radius of the PEMA-g- μ gel particles ($R_{h(\text{PEMA-g-}\mu\text{gel})} = 48 \pm 2$ nm).

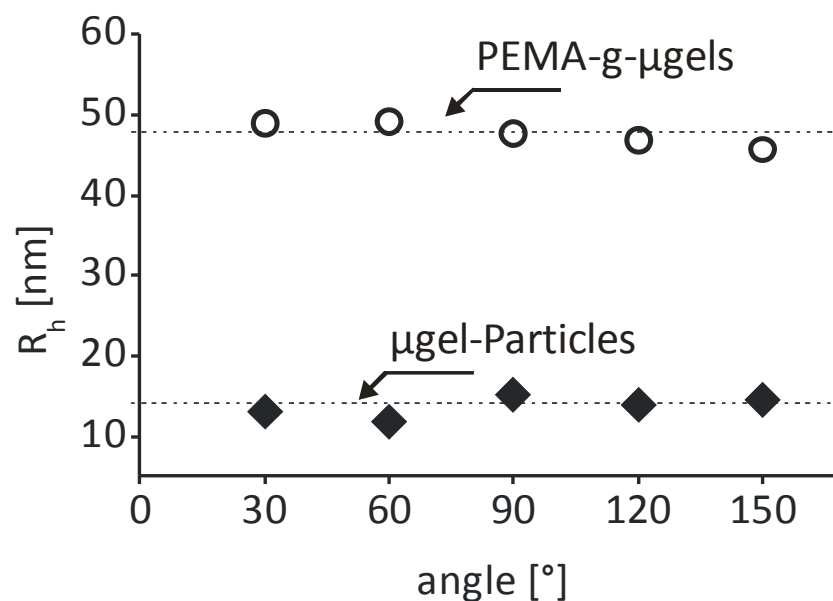


Figure 22. Hydrodynamic radius R_h of μ gel-particles and PEMA-g- μ gels at different scattering angles, calculated from DLS measurements.

The brush shell thickness was calculated by

$$lb_{(DLS)} = R_{h(PEMA-g-\mu gel)} - R_{h(\mu gel-particles)} \quad (4.2)$$

resulting in $lb_{(DLS)} = 34 \pm 2 \text{ nm}$.

Comparison of experimental data and theory

An estimation for the radius of such swollen particles could be made by considering the model for star shaped polymers explained earlier. Before we apply this model to our system of polymer-grafted nanoparticles, we have to bear in mind that the model of Daoud and Cotton assumes a star shaped polymer. The main difference between a star shaped polymer and a polymer-grafted nanoparticle is the core region. In a star shaped polymer the core consists of polymer chains, where each monomeric unit contributes to the radius of the star. The segment density stays constant up to a certain radius r_2 . In a polymer grafted nanoparticle the core consists of a different material which is not accounted in the model. However, for high grafting densities, i.e. $0.7 \text{ brushes} \cdot \text{nm}^{-2}$ as calculated for the μgel particles using equation (4.1), and small nanoparticles we expect that the segment density stays constant with increasing distance to the particle surface up to a certain value (referring to r_2 in Figure 3 and Figure 4). So the calculations according to Daoud and Cotton should reflect the length of the polymer brush which is attached to the μgel -particle.

Taking the radius of the μgel -particles and a grafting density of $\Gamma = 0.7 \text{ brushes}/\text{nm}^2$, we can calculate the number of brushes f grafted on one μgel -particle by $f = 4\pi r^2/\Gamma = 1724 \pm 255$. Furthermore, from the molecular weight of the brushes, which was determined by GPC, we can calculate the number of monomeric units $N = 330$, each having a effective bond length of a vinyl monomeric unit $l_{eff} = 0.2546 \text{ nm}$ ⁵¹. Thus we are now able to estimate the brush length by using relation (2.8) to $lb_{calc} = 33 \pm 1 \text{ nm}$ which is in perfect agreement to the measured brush length of $lb_{(DLS)} = 34 \pm 2 \text{ nm}$. These results lead us to some important conclusions:

1. The determination of the brush molecular weight by GPC after cleaving the brushes from the μgel -particles and the evaluation of the grafting density by equation (4.1) gave reasonable results.
2. The unusual high PDI for the cleaved PEMA brushes was a result of the cleaving process because a high polydispersity would also affect the hydrodynamic radius of the PEMA-g- μgels which in turn would lead to a bigger difference to the calculated values.
3. The length of the grafted brushes measured by DLS is in perfect agreement with the length calculated by the model of Daoud and Cotton.

Cleaning of silicon wafers

The silicon wafers we used as a substrate for SPM and GISAXS-measurements were cleaned by treating them in an argon plasma for 10 min at a pressure of $\sim 2 \cdot 10^{-2}$ mbar in a commercial plasma cleaning setup operating at 30 watt plasma power (PDC-002, Harrick Plasma, USA).

4.4.3 Sample preparation for SPM and GISAXS measurements

We prepared the samples in the following way. We mixed PEMA-grafted μ gels with core volume fractions (Φ_c) of 0.26 and 0.49 with homopolymers of different molecular weight (Table 3). The particle-matrix system was diluted in toluene (p.a. - grade, Riedel de Haën) yielding a concentration of 100 mg/mL and treated with ultra-sound for 15 min. To prepare samples for GISAXS measurements we spin-coated (2000 rpm, 30 sec) the solution on pieces of silicon wafer (Si-Mat, CZ), previously cleaned as described above. The thickness of these films varied between 400 and 600 nm. Furthermore, we prepared samples of PEMA-grafted μ gels and non-modified μ gel-particles without a homopolymer matrix in the same way.

4.4.4 SPM-Imaging

By SPM-imaging of μ gel-particles which were spin coated on a silicon wafer we found that the μ gel particles were well-distributed over the wafer and single particles could be addressed for analysis (Figure 24a, c). More than 100 μ gel-particles were analyzed and a Gaussian distribution was fitted to the histogram of the height distribution (Figure 24b, l). The fit has a maximum at 18 ± 1 nm which results in a radius of the μ gel-particles denoted as $r_c = 9 \pm 1$ nm. The height of the particles (h_p) is given by the displacement of the SPM-tip in z-direction during a scan across a particle. To measure the width of a particle, we have to take the tip convolution into account. As long as the tip is much sharper than the feature, the true edge profile of the feature is represented in the cross-section. However, when the feature is sharper than the tip, the image will be dominated by the shape of the tip. In Figure 23a the origin of tip convolution is demonstrated. The lateral distance x is much larger than the height of the particle h_p (Figure 23b).

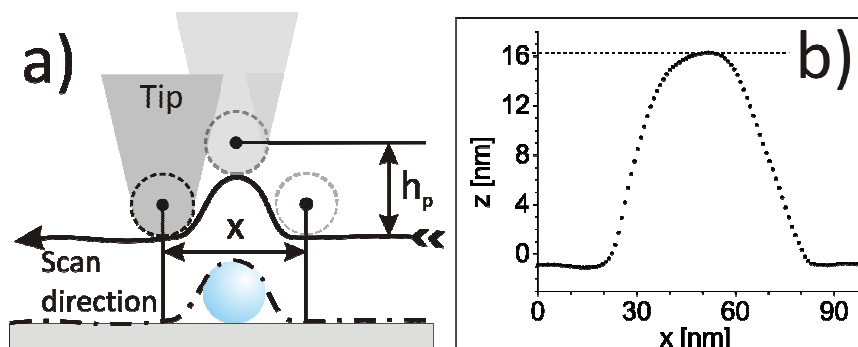


Figure 23. Schematic illustration of SPM-imaging of features with a size comparable to the tip size. Lateral dimensions have to be corrected with the tip diameter. b) Topographic cross-section of a μ gel-particle.

We observed some aggregates of μ gel-particles (Figure 24a) which could explain the shoulder in the GPC curve for the μ gel-particles (Figure 21, black, dashed). Furthermore, comparison of the DLS ($R_{h(\mu\text{gel-particle})} = 14 \pm 1 \text{ nm}$) and SPM ($r_c = 9 \pm 1 \text{ nm}$) measurements showed that the hydrodynamic radius was about 5 nm larger than the radius of μ gel-particles in the dry state. The reason for this discrepancy was most likely the swelling of the μ gel-particles in solvent during the DLS measurement.

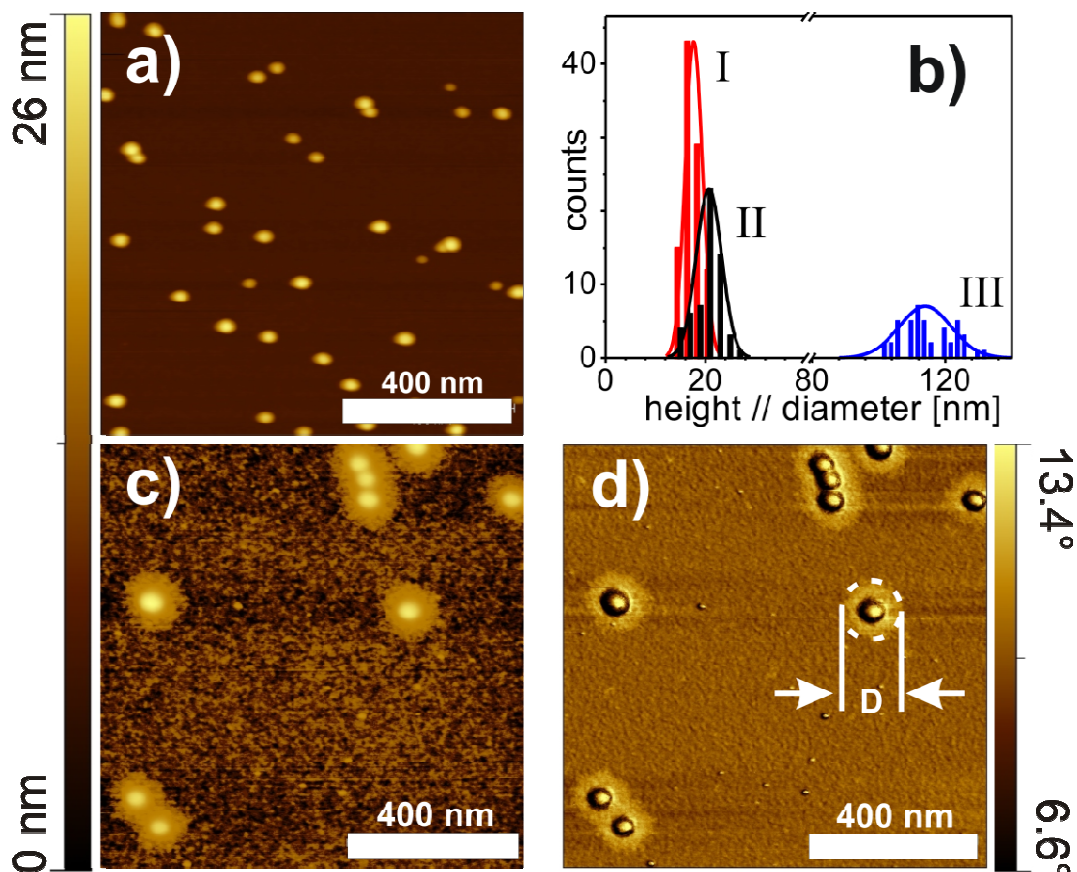


Figure 24. a) Topography image of μ gel-particles. b) Histogram data of the height of μ gel-particles (I), height of PEMA-g- μ gels (II) and diameter D of PEMA disk (III). c) Topography image of PEMA-grafted μ gels spin-coated on a silicon wafer. d) Phase-contrast image where the PEMA brushes appear as a bright disk with diameter D around the core.

We found an increase in height of 3 nm for the PEMA-g- μ gels (Figure 24b, II) compared to the unmodified μ gel-particles. This increase was attributed to the presence of PEMA brushes underneath and on top of the μ gel particle as sketched in Figure 25. From the topography image (Figure 24c) the PEMA-g- μ gels appear as heightened dots, whereby in the phase-contrast image the brushes appear more intense as a disk around the μ gel-particle (Figure 24d). The small features between the PEMA-g- μ gels could be free polymers as the peak at bigger retention volumes in GPC data (Figure 21, red, solid) suggests. To determine the brush shell thickness we have the obtained radius r_c of μ gel particles likewise from topography images and the diameter ($D = 114 \pm 8 \text{ nm}$) of the disk of PEMA-g- μ gels from the phase-contrast image (Figure 24d). An estimate of the brush shell thickness from SPM results was obtained on the basis of a geometric model (Figure 25) and the following equation.

$$l_{b(SP\text{M})} = D/2 - r_c \quad (4.3)$$

The brush shell thickness $l_{b(SP\text{M})}$ was determined to be 48 ± 8 nm. The error was calculated via Gaussian error propagation. A calculation using the same degree of polymerization as our polymer brush ($N = 330$ monomeric units) having an effective bond length ($l_{eff} = 0.2546$ nm) of a vinyl monomeric unit

$$r_{cont} = N \cdot l_{eff} \quad (4.4)$$

yields the conventional contour length r_{cont} of 84 nm. This value is the maximum end-to-end distance of a physically completely stretched chain (all-trans conformation). This implies that the PEMA brushes are spread on the silicon wafer to 57% of the contour length. Comparison of the DLS ($l_{b(DLS)} = 34 \pm 2$ nm) to the SPM ($l_{b(SP\text{M})} = 48 \pm 8$ nm) measurements showed a discrepancy of 15 nm between the swollen state of the brush in DLS measurements and a dry, but spread state in SPM measurements. This result showed that the brush is more stretched on a substrate (e.g. silicon wafer) than in toluene solution.

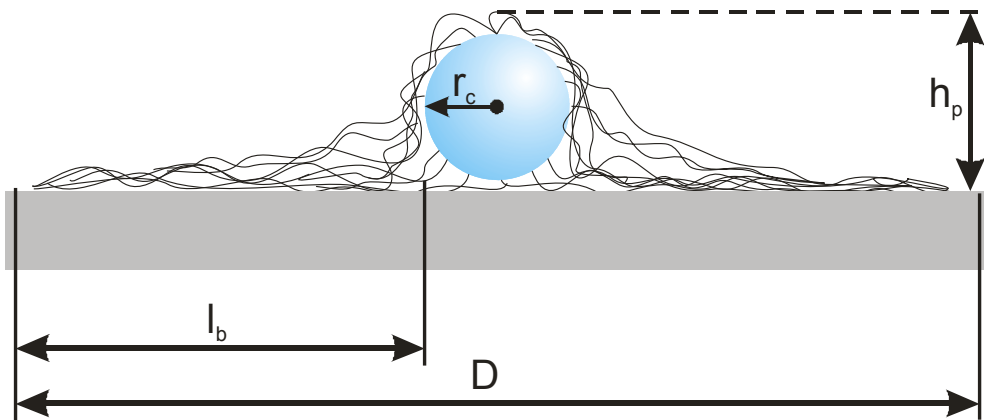


Figure 25. Schematic illustration of a PEMA-g-μgel particle of height h_p lying on a silicon substrate. The diameter of the PEMA-brush disc D and the radius of the core particle r_c were taken to calculate a brush-shell thickness l_b . Dimensions do scale.

4.5 Characterization of dispersions of PEMA-g-μgels and homopolymers

After characterizing the neat μgel-particles, the polymer brushes, the PEMA-g-μgels and the homopolymers we investigated the distribution and dispersion behavior of the PEMA-g-μgel particles dispersed in PEMA homopolymer matrices. We chose PEMA-g-μgel dispersions with core volume fractions of $\Phi_c = 0.26$ and 0.49 , corresponding to 20 and 40 wt.%.

Surface imaging of PEMA-g- μ gels dispersed in a homopolymer matrix

By analyzing the phase-contrast images of $\Phi_c = 0.26$ samples, the PEMA-g- μ gels appeared as bright areas and the homopolymer matrix as darker areas. In the case without a matrix homopolymer (Figure 26, $P = 0k$), we observed a dense packing of the PEMA-g- μ gels. For the matrix with the lowest molecular weight we observed distributed PEMA-g- μ gels (Figure 26, $P = 12k$). The dispersion became unstable (Figure 26, $P = 101k$) with a higher matrix molecular weight and finally aggregates (Figure 26, $P = 269k$) were formed.

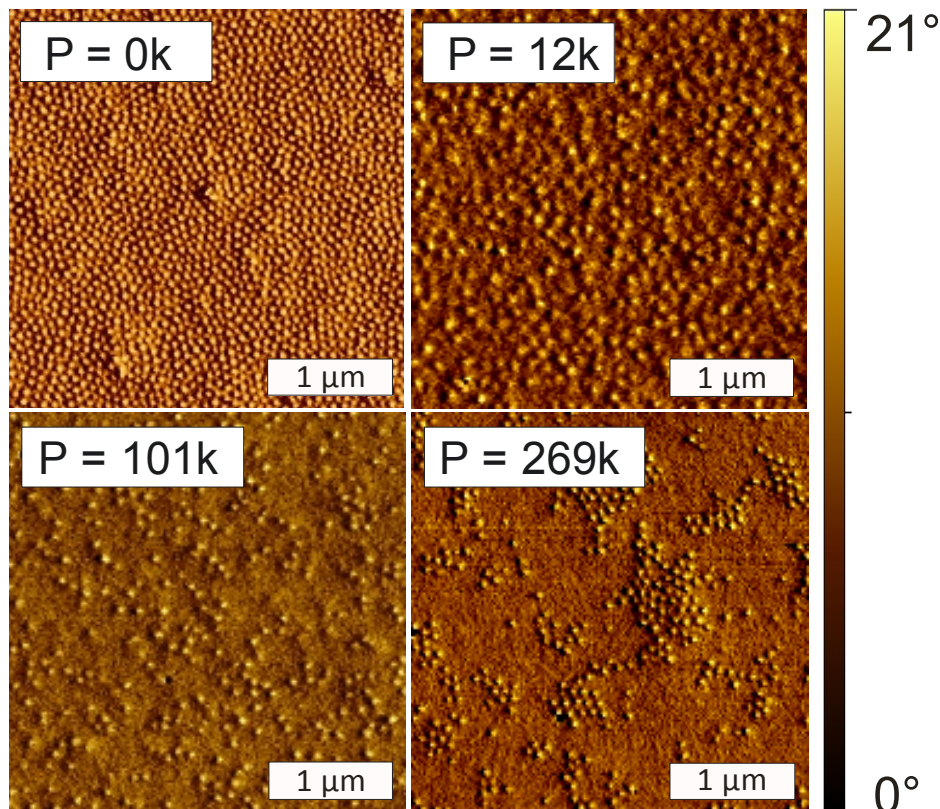


Figure 26. Phase-contrast images of PEMA-grafted μ gels ($\Phi_c = 0.26$) dispersed PEMA matrix homopolymer with different molecular weights. PEMA-grafted μ gels appear as bright dots embedded in a matrix with darker contrast.

In order to compare the different compositions more quantitatively, it would be very useful to find a parameter which relates the dispersion behavior with the N/P ratio. The distance between neighboring particles and the distribution of distances indicates aggregation or homogenous distribution of particles, therefore the nearest neighbor distance might be a possible indicator. The SPM images seen above contain all information we need to extract this distance and their distribution.

NN1-Distance calculation

The images of PEMA-g- μ gels dispersed in a homopolymer matrix were analyzed by applying a straightforward k-nearest neighbor algorithm written in MATLAB. In this algorithm particle positions

were assigned by hand and the Euclidian distance between each particle in the overall image was calculated using:

$$NN_v = \sqrt{(x_j - x_i)^2 + (y_j - y_i)^2} \quad (4.5)$$

x_j, y_j are the coordinates of the particle of interest and x_i, y_i are the coordinates of every other particle in the image respectively. NN_v indicates an array of all k-nearest neighbors for a particle v in which $(0 < k < n-1)$. n is the number of all particles observed. In the following we will use NN_1 -Distance as an abbreviation for the first nearest neighbor distance. To understand the results of this analysis and to interpret the results correctly I like to give some exemplary results of test images that have been analyzed with the algorithm. The basic test image consists of grid of 10*10 squares with a lattice length of 100 nm. If we distribute imaginary particles randomly over this grid (Figure 27a), the first nearest neighbor distance NN_1 should have a Gaussian distribution (Figure 27b). The maximum of this Gaussian represents the average distance of neighboring particles. In case of the test image in Figure 27 we distributed $n=50$ particles randomly over the grid. The maximum is at 113 nm with a standard deviation of ± 22 nm.

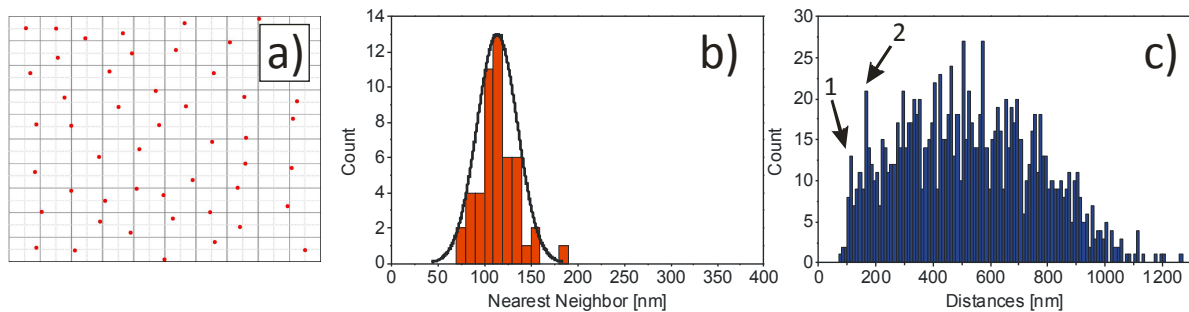


Figure 27. Results for the NN_1 analysis of homogenous particle distribution over a given area. a) The test grid with 50 imaginary particles represented as red dots. b) Histogram of the first nearest neighbor distance. c) Histogram of all calculated distances.

For $(i, j = n - 1)$ we achieve 1225 values using equation (4.5) for $n=50$ particles (Figure 27c). The nearest neighbor distance can also be deduced from the histogram of all calculated distances (Figure 27c, first arrow "1"). Furthermore, the second nearest neighbor distance (165 nm), which also has a Gaussian distribution, can be deduced from the histogram of all distances (Figure 27c, second arrow "2"). If we assume a situation where the particles tend to accumulate at the edges of the sample, e.g. because of interface effects (Figure 28a), we can deduce the different length-scales of the distribution by analyzing the NN_1 -Distance and the histogram of all distances. In the NN_1 -Distance histogram (Figure 28b) we can see two distributions. The first one representing the NN_1 -Distance between the particles on the left and right face of the grid with of 65 nm. The second one represents the NN_1 -Distance (183 nm) of the particles in the center of the grid. The distance of the particles on

the left to the particles on the right side of the grid can be deduced from Figure 28c. Here the peak at 805 nm indicates the distance between the “lined up” particles.

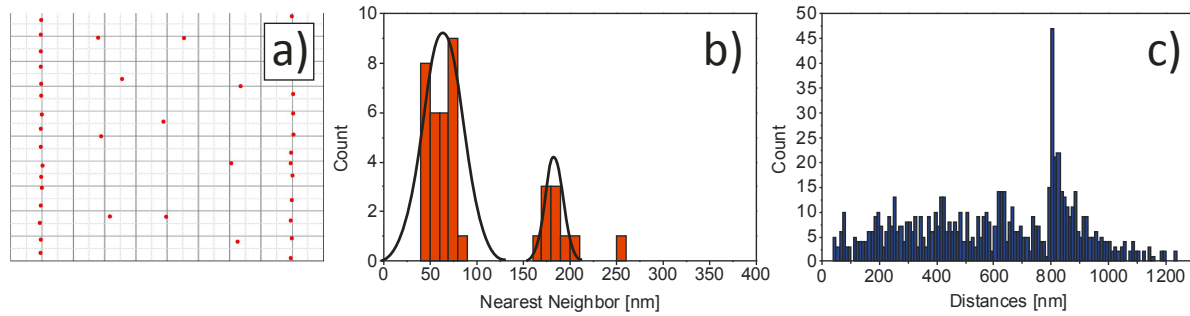


Figure 28. Results for the NN_1 analysis of an inhomogeneous particle distribution over a given area with a preference of the particles to the left and right face of the grid. a) The test grid with 50 imaginary particles represented as red dots. b) Histogram for the first nearest neighbor distance. c) Histogram for all calculated distances

In conclusion, the analysis of the NN_1 -Distance and the histogram of all distances provides information of interparticle distance and preferred particle positions, i.e. in case of particle accumulation at interfaces (Figure 28a). The presented straight forward algorithm which calculates the Euclidian distance between particles may therefore be a tool to analyze particle mixtures with homopolymers of different composition.

In Figure 29 we plotted the NN_1 -Distance, obtained by the analysis of the phase contrast images of samples with different matrix M_w , as a function of the N/P ratio for both Φ_c . For the sample without homopolymers (Figure 26, $P = 0k$), we observed a NN_1 -Distance of 38 ± 4 nm (Figure 29a, star). This means that for two neighboring μ gel particles each having a radius of $r_c = 9 \pm 1$ nm the brush shell thickness $l_{b(SPM,assembly)}$ can be calculated by

$$l_{b(SPM,assembly)} = \frac{NN_1}{2} - r_c \quad (4.6)$$

We calculated the thickness of the brush shell $l_{b(SPM,assembly)} = 10 \pm 2$ nm. For high molecular weight of the matrix with a ratio of $N/P = 0.14$ and 0.21 , we observe a NN_1 -Distance of 38 ± 6 and 39 ± 6 nm respectively for the low core volume fraction. For the high core volume fraction we measured a NN_1 -Distance of 37 ± 6 and 38 ± 6 nm respectively. Compared to the sample where no homopolymer is present we can conclude that within the aggregates at low N/P ratios there is no homopolymer present as depicted in Figure 6c.

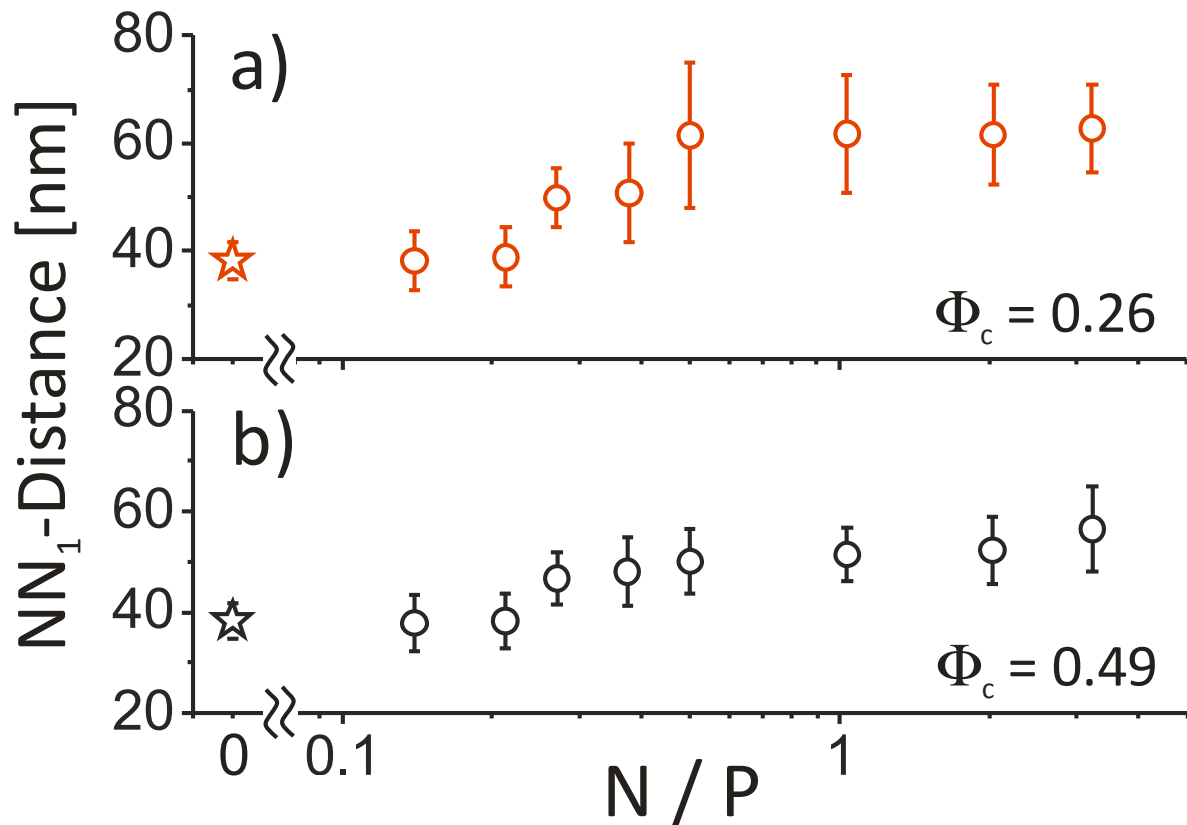


Figure 29. Particle distance as a function of N/P a) for a core volume fraction $\Phi_c = 0.26$ and b) for a core volume fraction $\Phi_c = 0.49$. The stars represent the respective samples without matrix polymer.

As we have seen from DLS measurements, if the brush is swollen by a good solvent like toluene, the thickness of the brush-shell is about 34 ± 2 nm. In the dry state when spread out on a silicon wafer, the brushes even extend to a length of 48 ± 8 nm as measured by SPM. So at small N/P ratios, the brushes must be contracted and/or interpenetrate each other to a certain extent. If the N/P ratio is increased, or in other words the molecular weight of the matrix is decreased, we observe an increasing NN_1 -Distance for both core volume fractions until reaches a maximum of 63 ± 8 and 56 ± 8 nm for $\Phi_c = 0.26$ and $\Phi_c = 0.49$ respectively. The increasing NN_1 -Distance indicates that the polymer-brushes start to swell when the matrix M_w decreases. For $\Phi_c = 0.26$ a plateau is reached at which the NN_1 -Distance does not increase any more at $N/P > 0.5$, i.e. matrix $M_w = 75400$ g/mol. For $\Phi_c = 0.49$ the plateau is not as distinct as for $\Phi_c = 0.26$ but the NN_1 -Distance does not increase significantly for $N/P > 0.3$, i.e. matrix $M_w > 126000$ g/mol. We may therefore say that a transition between well dispersed and aggregated PEMA-g- μ gels appears at $N/P \geq 0.5$ for $\Phi_c = 0.26$ and at $N/P \geq 0.3$ for $\Phi_c = 0.49$.

In contrast, Dutta and Green⁷¹ observed a transition between stable and aggregated states of PDMS-g-silica particles in concentrated polymer solutions at a N/P ratio ~ 1 by DLS. The first argument for this difference could be that in our study the interface between the polymer and air plays a role

when the PEMA-g- μ gels distribute at the surface of our samples. As we have seen in Figure 2a, a molecule located at the liquid-gas (L-G) interface loses half of its attractive interactions. If we transfer this concept to the PEMA-g- μ gels located at the L-G interface (the liquid in our case is the polymer melt) we might expect a distance between particles that is larger than it would be inside the bulk material. For brush coated particles which are dispersed inside the melt it is hard to calculate the interacting forces. Wijmans et al.⁷² used self-consistent field methods to calculate the interaction potentials between two parallel plates with grafted polymer brushes in the presence of non-adsorbing, “free” polymer chains. For free polymers that are larger than the brush ($N/P < 1$), a depletion-induced attraction appears between the grafted plates. For a fixed grafting density this attraction becomes stronger with increasing free polymer length.

To answer the question, whether the distance between particles is larger at the surface than inside the bulk material, we prepared cross-sections of the above presented samples by fracturing them as depicted in (Figure 30b). The fractured faces were then imaged by SPM.

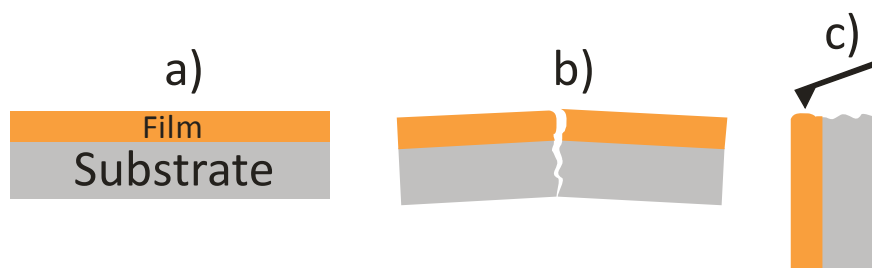


Figure 30. Preparation of cross-sections for SPM imaging. A sample a) is fractured b) and the cross-section is imaged c).

SPM-Imaging of fractured surfaces

In Figure 31a we present the topography image of a fractured sample ($\Phi_c = 0.26$) with molecular weight of the homopolymer $M_w = 18500$ g/mol, reflecting an N/P ratio of 2.04. The flat area on the right side of the image is the fractured silicon substrate. It is followed by a ~ 500 nm thick homopolymer film containing the PEMA-g- μ gels and a dark area which is air. Some of the PEMA-g- μ gels are torn off the fractured surface and appear as highlighted dots in the image with a height of about 30-40 nm. The holes also have a diameter between 25 and 40 nm indicating that particles were torn off this cross-section but remained on the other face of the section. Interestingly the height of the particles is much larger than the height of the particles measured in dry state (21 nm) by SPM (Figure 25). This indicates that the torn off PEMA-g- μ gels are swollen by the short matrix chains and thus their diameter is increased. In Figure 31b the respective phase contrast image is shown.

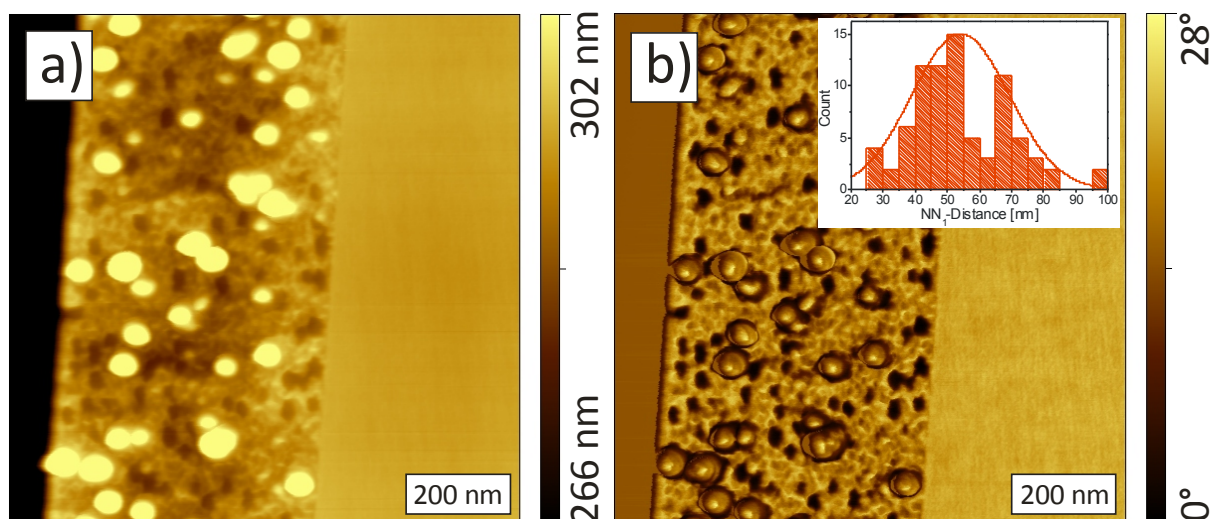


Figure 31. Fractured sample of PEMA-g- μ gels ($\Phi_c = 0.26$) dispersed in PEMA homopolymer ($M_w = 18500$ g/mol). a) Height image and b) phase contrast image. The inset in (b) shows the NN_1 -Distance distribution measured from the phase contrast image.

The inset in Figure 31b shows the NN_1 -Distribution of the PEMA-g- μ gels measured from the phase contrast image. To achieve this histogram, not only the particles but also the holes were assigned for the calculation, because a hole represents the position of a particle which remained on the other side of the fractured face. A Gaussian distribution was fitted to the histogram to calculate the average NN_1 -Distance and the standard deviation. We have calculated a NN_1 -Distance of 54 ± 15 nm which is lower than the one measured at the unfractured surface 63 ± 8 nm.

The cross-section of a sample with high molecular weight matrix ($M_w = 177800$ g/mol) is presented in Figure 32, having a N/P ratio of 0.21. The film thickness here was > 1 μ m, so the scanned area does not cover the air interface as shown in Figure 31. The topography of the fractured surface (Figure 32a) is much rougher than for the low M_w sample and shows elongated, wormlike structures. The silicon substrate on the right side of the image is not clearly visible in the topography image but highly contrasted in the phase contrast image (Figure 32b). Neither in the topography image, nor in the phase contrast image single PEMA-g- μ gels could be clearly addressed for NN_1 -Distance analysis. Though, the elongated, wormlike structures might be agglomerated PEMA-g- μ gels as could be seen from a detailed analysis of these structures in the phase contrast image (blue circles, Figure 32b). The features marked with the blue circles in Figure 32b might be PEMA-g- μ gels, but, however, the number of them was not sufficient for statistical analysis. The preparation of the cross-sections with a focused ion beam may lead to smoother surfaces and may allow an analysis of the NN_1 -Distance.

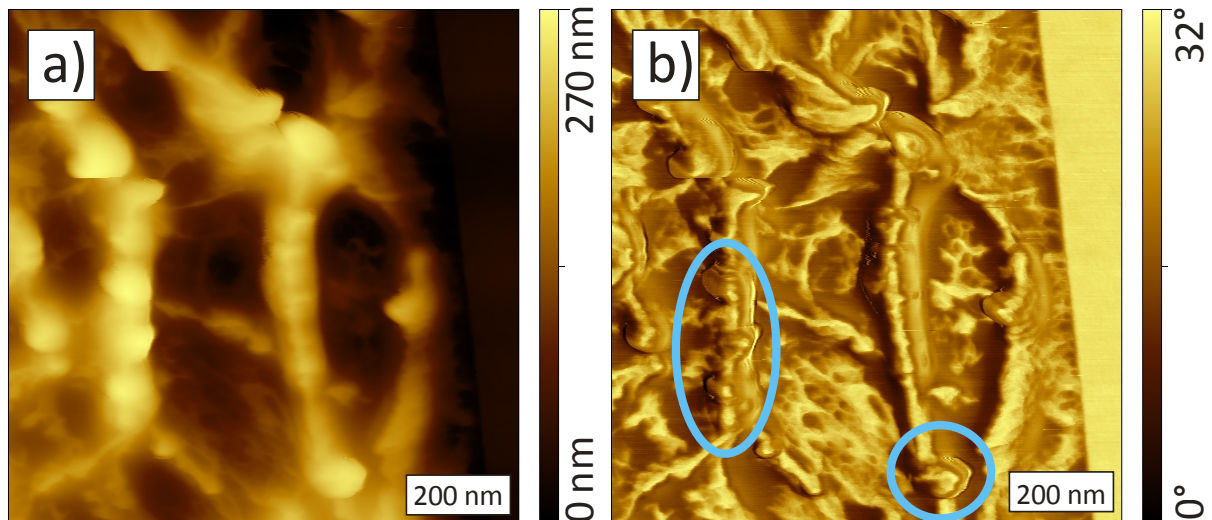


Figure 32. Fractured sample of PEMA-g- μ gels ($\Phi_c = 0.26$) dispersed in PEMA homopolymer ($M_w = 177800$ g/mol). a) Height image and b) phase contrast image.

However, for the low M_w matrix, the discrepancy in the NN_1 -Distance between an unfractured surface and a cross-section supports the hypothesis we made for particles having more attractive interactions inside the bulk material than particles at the surface. Nevertheless, the standard deviation of the NN_1 -Distance is much larger for the cross-section than for the unfractured surface. So the discrepancy and the high standard deviation might be caused by the fracturing process. It would be therefore desirable to investigate the dispersion of the PEMA-g- μ gels in a sample that is undisturbed, e.g. without preparing cross-sections, and additionally being able to get information of the distribution *inside* the sample. We therefore carried out GISAXS measurements of the same samples which were discussed above.

4.6 GISAXS measurements

In a typical GISAXS experiment, from the scattered intensity map one can extract a quantity which is related to the correlation length of the scattering bodies. In general the correlation length is defined as the distance from a certain point beyond which there is no further correlation of a physical property associated with that point. A typical scattered intensity map of our samples is shown in Figure 33. The intense specular reflection from the surface is blocked by a beamstop located at the upper part of the image. The primary beam is blocked by a second beamstop located in the lower part of the image.

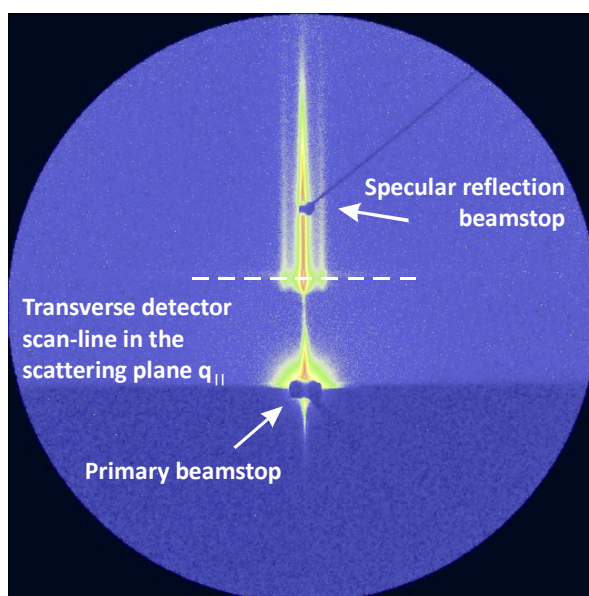


Figure 33. Typical scattered intensity map obtained from a GISAXS experiment. Matrix M_w 17400 g/mol and $\Phi_c = 0.49$.

We interpreted the measured correlation length as the averaged centre of mass distance between neighboring particles. Transverse detector scans of the full 2D scattering pattern in reciprocal scattering plane $q_{||}$ result in a scattering curve which contains information about the correlation of the sample. Therefore we determined the correlation length of our samples as the position of the correlation peak.

In Figure 34 we show the transverse detector scans of four PEMA-grafted μ gel – homopolymer samples with a core volume fraction $\Phi_c = 0.49$. Curve I represents the pure PEMA-g- μ gels without any homopolymer matrix, followed by curve II representing a homopolymer M_w of 19k, curve III: 36k and curve IV: 178k.

For samples of the PEMA-g- μ gels without homopolymer matrix, we expected the brushes to be contracted and to some extent interpenetrated. Thus inter-particle distance should be small. We calculated a distance of $\Lambda = 41 \pm 9$ nm for this case.

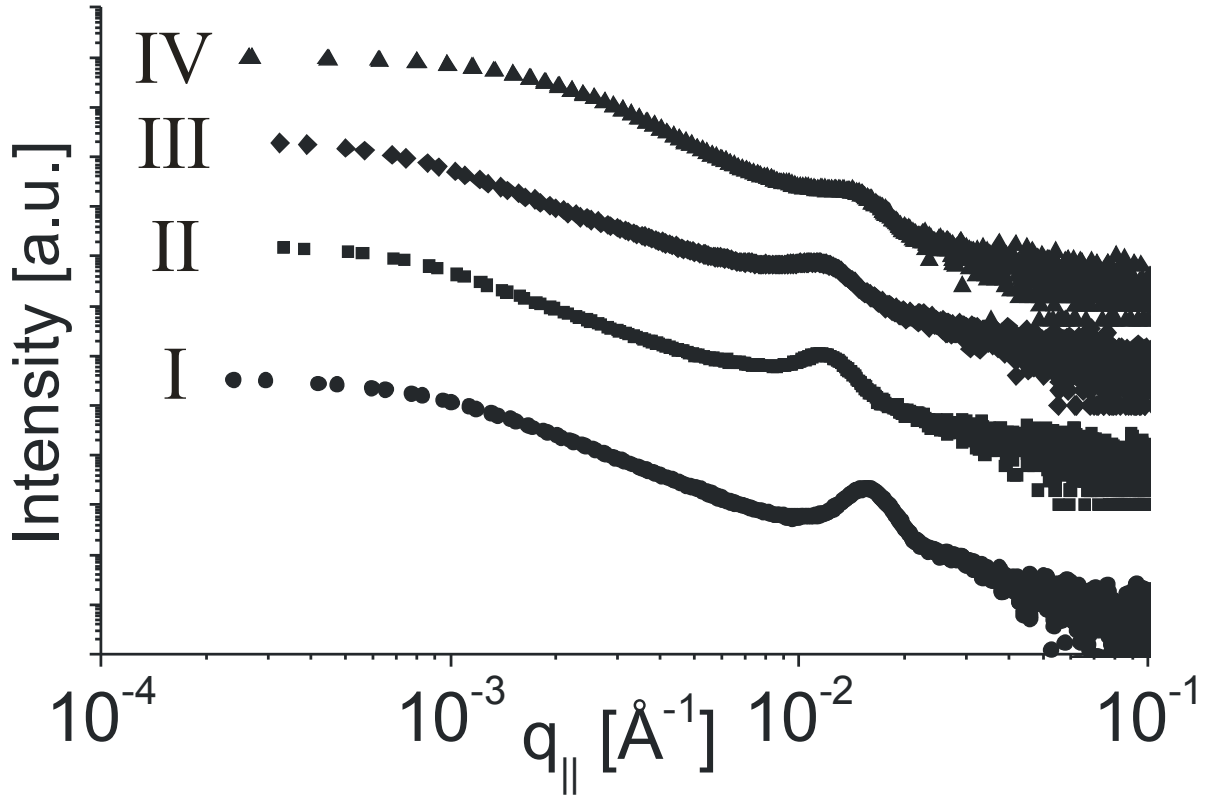


Figure 34. GISAXS spectra of four PEMA-grafted μ gel – homopolymer dispersions (volume fraction $\Phi_c = 0.49$). The M_w of the matrix polymer was varied from I to IV as follows. I = no homopolymer (0k), II = 19k, III = 36k and IV = 178k. The curves have been multiplied by factors of 10^2 in the ordinate for clear visualization.

In the absence of a homopolymer matrix the distance between two neighboring μ gel-particles, each having a radius of $r_c = 9 \pm 1$, is referred to the brush shell thickness ($l_{b(GISAXS)}$) of the grafted polymer brush and can be calculated from GISAXS data in analogy to equation (4.6) as:

$$l_{b(GISAXS)} = \frac{\Lambda}{2} - r_c \quad (4.7)$$

We calculated a brush shell thickness of $l_{b(GISAXS)} = 12 \pm 5$ nm. This is in good agreement with the data obtained by SPM ($l_{b(SPM,assembly)} = 10 \pm 2$ nm). The brushes were contracted and interpenetrated one another. Comparing these brush shell thicknesses to the value obtained by DLS for a wet brush ($l_{b(DLS)} = 34 \pm 2$ nm) the brushes contracted to nearly a third in absence of solvent or matrix polymer. The correlation lengths for particles dispersed in homopolymer matrices with varying molecular weight are plotted in Figure 35 for both core volume fractions.

For ratios $N/P < 1$ we observed a small inter-particle distance for both core volume fractions. The brushes expel the surrounding high M_w matrix and the dispersion is unstable. Since the intensity of the correlation peak decreased with increasing molecular weight of the matrix, there must be contributions of other correlation lengths leading to a more shoulder-like shape of the peak (Figure

34, IV). These contributions may come from a broader inter-particle distance distribution which is also shown in SPM images (Figure 26). At the highest molecular weight of the matrix at 178000 g/mol measured in GISAXS ($N/P = 0.21$), the particles had a distance of $\Lambda = 43$ nm which indicated that the particles formed aggregates, which have a similar inter-particle distance like the above-mentioned dry brush systems without a matrix (Figure 34, I).

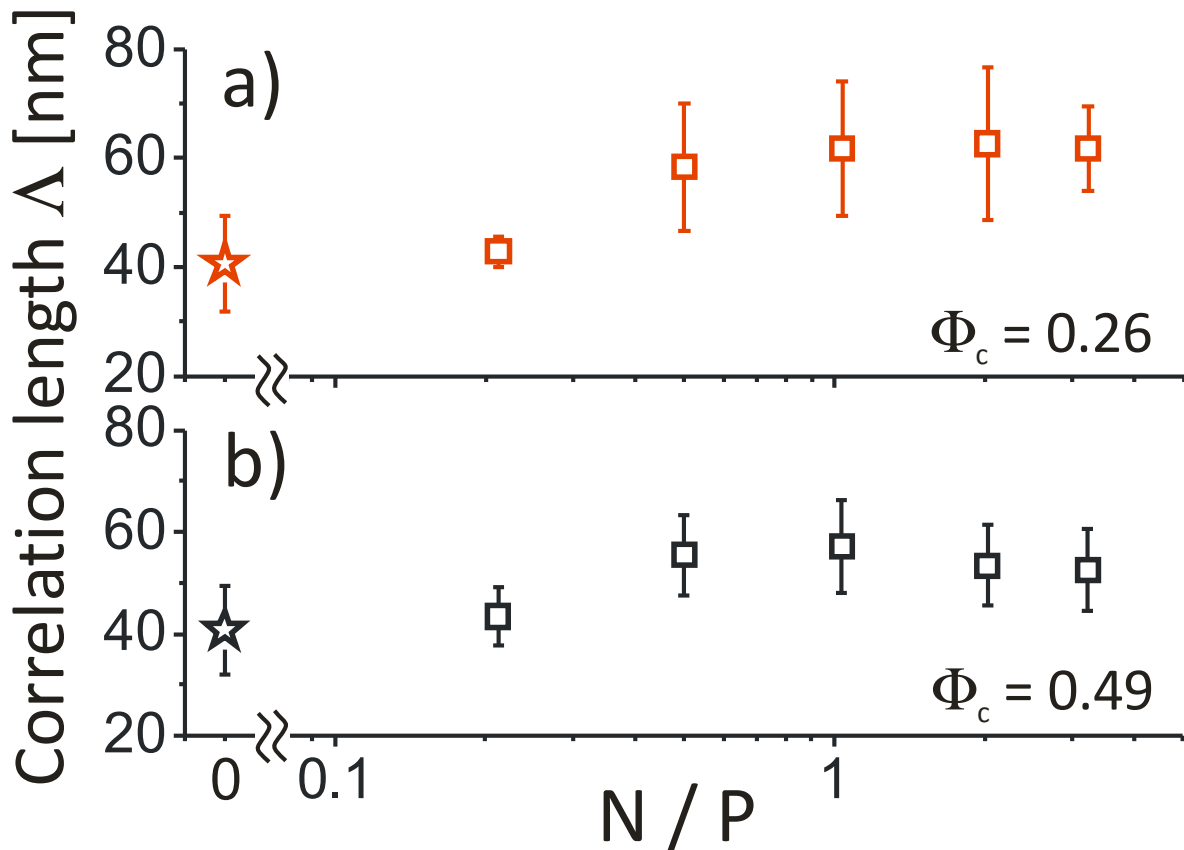


Figure 35. Correlation length Λ as a function of N/P a) for a core volume fraction $\Phi_c = 0.26$ and b) for a core volume fraction $\Phi_c = 0.49$. The stars represent the respective samples without matrix polymer.

Mixing of the particles with low molecular weight matrices led to swelling of the brushes and an increase of inter-particles distance up to $\Lambda = 62 \pm 8$ nm ($\Phi_c = 0.26$, $P = 12k$) and $\Lambda = 56 \pm 8$ nm ($\Phi_c = 0.49$, $P = 12K$). The particles were distributed throughout the matrix and no aggregates were visible in SPM images. If we compare the NN_1 -Distance of the cross-section (54 ± 15 nm) with the NN_1 -Distance measured at the unfractured surface (63 ± 8) and the correlation length of ($\Lambda = 62 \pm 8$ nm) measured by GISAXS we can conclude that the fracturing process had an influence on the interparticle distance. The shape of the curves in Figure 35 and the absolute values of the correlation lengths are in good agreement with NN_1 -Distance measurements at the surface of the sample (Figure 32).

4.7 Dynamic Mechanical Thermal Analysis

Here it is the aim to design a composite material that has the mechanical properties of the pure matrix polymer (e.g. elastic modulus) while the other constituent (e.g. nanoparticles) add or enhances wear resistivity. The nanoparticles which were used in this work consist of a “soft” network of silicon-organic compounds which could be swollen by solvent as seen from DLS measurements. We therefore expect a less pronounced reinforcing effect (in terms of elastic modulus) than one would expect from solid, hard nanoparticles when blended with a polymer matrix.

We have shown before that the dispersion behavior of PEMA-g- μ gels depends on the M_w ratio of brushes to matrix polymer (N/P). It is evident that a well dispersed system shows different mechanical properties than a phase separated system. One can imagine that an armored concrete beam will fracture under load when the steel armor is only incorporated at one end of the beam. Following this train of thought, the contribution of the PEMA-g- μ gels to the elastic modulus of the composite should also depend on the N/P ratio.

In this chapter I will investigate how the composition of N/P and core volume fraction due to the addition of PEMA-g- μ gels influences the elastic properties of the composite. I will discuss the effect of unmodified μ gel particles as well as the effect of the polymer brushes on the mechanical behavior of the composite. The beneficial effect that is served by the PEMA-g- μ gels, namely the enhanced wear resistivity, is then discussed in chapter 7.

DMTA of neat homopolymer

The result of a DMTA measurement for a PEMA homopolymer ($M_w = 36400$ g/mol) is given in Figure 36. The mastercurves for the storage and the loss moduli at $T_{ref} = 70^\circ\text{C}$ are showing the typical regimes for a viscoelastic material. At high frequencies, in the glassy state, the storage modulus G' predominates and reaches the value of about $5 \cdot 10^8$ Pa. In the segmental flow region at around 10^7 Pa the loss modulus G'' predominates and decreases slower than G' . This slow decrease is due to the energy dissipation in the form of heat, caused by friction in the main chain segments, which consist of a few repeating units that become mobile and as a result begin to move. Also in this region the loss tangent ($\tan \delta$) has a local maximum which indicates high damping due to the movement of the segments.

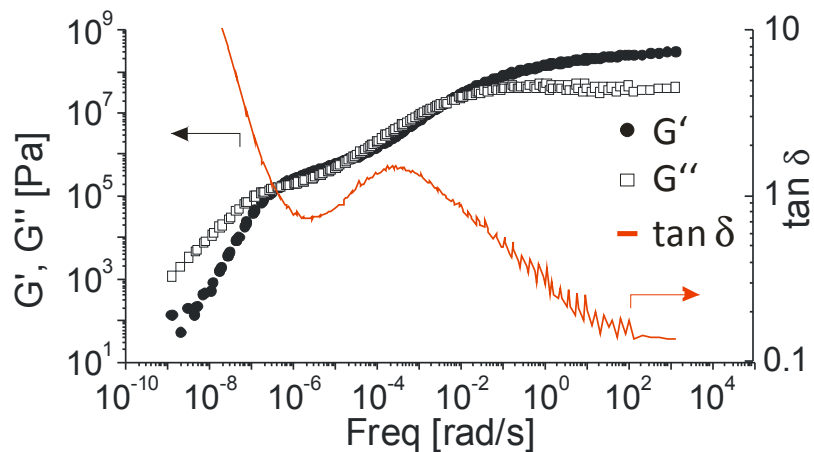


Figure 36. Exemplary mastercurve of G' (filled circles) and G'' (open squares) and loss tangent ($\tan \delta$) as a function of frequency for homopolymer with $M_w = 36\text{k}$. The reference temperature to construct the mastercurve was 70°C .

As the frequency decreases further, G' and G'' are reaching the viscoelastic regime where elastic behavior dominates ($G' > G''$). We observe a local minimum of the loss tangent and can therefore determine the plateau modulus according to equation (3.10) and an entanglement molecular weight according to equation (3.11) which results in $3.8 \cdot 10^5$ Pa and 9340 g/mol respectively. In the viscous flow regime at low frequencies, dissipation of energy prevails and G'' predominates. The polymer starts to creep.

DMTA of low M_w matrix composites ($N/P > 1$)

For samples where the PEMA-g- μ gels were blended with homopolymer of $M_w = 18500$, i.e. at a N/P ratio of 2.03 we observed a plateau modulus for $\phi_c = 0.26$ of $4.4 \cdot 10^5$ Pa for the homopolymer and $5.2 \cdot 10^5$ and $4.8 \cdot 10^5$ Pa for the blended samples (Figure 37a). No horizontal shift was observed for both composites compared to the homopolymer. The mastercurves were showing the same shape which implies similar mechanical behavior of the homopolymer and the composite as it was desired. In both samples ($\phi_c = 0.26$ and 0.49) we observed that they start to creep at higher temperatures

(i.e. lower frequencies) than the homopolymer. The enhanced creep behavior might be a hint of improved interfacial interaction between PEMA-g- μ gel particles and the homopolymer.⁷³

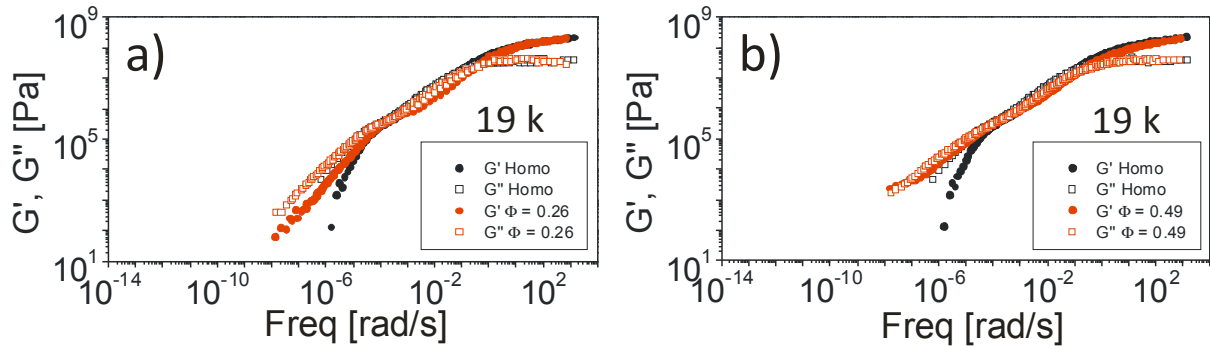


Figure 37. Mastercurves for blends of PEMA-g- μ gels with homopolymers of $M_w = 18500$ g/mol for core volume fractions of 0.26 (a) and 0.49 (b).

DMTA of medium M_w matrix composites ($N/P \approx 1$)

The results of DMTA measurements for a homopolymer matrix with $M_w = 36400$ g/mol and a blend of the same homopolymer and PEMA-g- μ gels are shown in Figure 38a, b. We calculated a plateau modulus of $3.8 \cdot 10^5$ Pa and for the composites $3.3 \cdot 10^5$ and $4.6 \cdot 10^5$ Pa for $\phi_c = 0.26$ and 0.49 respectively. From the very similar plateau moduli of the homopolymer at $\phi_c = 0.26$ we can conclude that the addition of PEMA-g- μ gels does not change the elastic modulus significantly.

When the core volume fraction is increased to 0.49 the plateau modulus also increases. At such high volume fractions we see the contribution of the μ gel particles to the plateau modulus of the composite. In the segmental flow and the rubbery region the storage and loss moduli for the composite with high volume fraction decrease faster than the moduli of the homopolymer. This fast decrease indicates that the PEMA-g- μ gels have an effect on the elastic properties of the matrix.

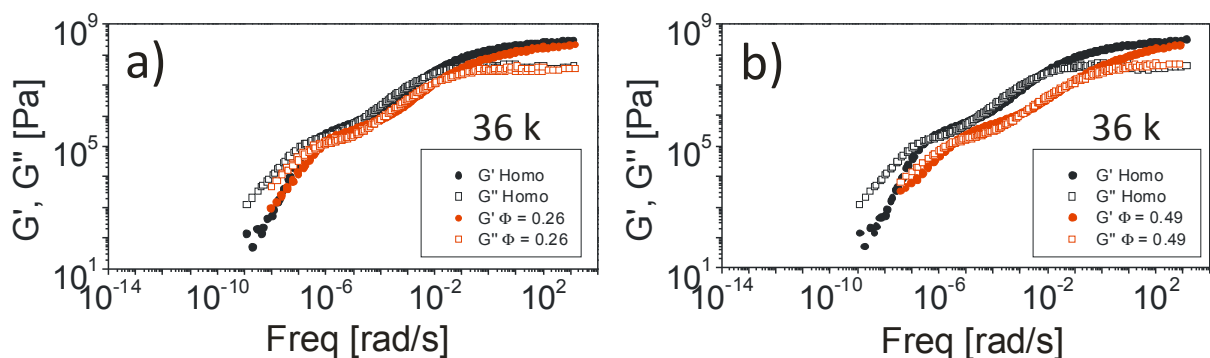


Figure 38. Mastercurves for blends of PEMA-g- μ gels with homopolymers of $M_w = 36400$ g/mol for core volume fractions of 0.26 (a) and 0.49 (b).

DMTA of high M_w matrix composites ($N/P < 1$)

For the highest molecular weight ($M_w = 177800$ g/mol), i.e. when the N/P ratio is small (0.21) and phase separation of PEMA-g- μ gels and homopolymer takes place. Here we observed a horizontal shift of the mastercurve towards higher frequencies and a vertical shift to lower moduli (Figure 39). The horizontal shift of G' and G'' to higher frequencies due to addition of PEMA-g- μ gels would imply a reduction of the glass transition temperature. Indeed, T_g decreases from 83 °C for the homopolymer to 81 °C for $\phi_c = 0.26$ and to 76 °C for $\phi_c = 0.49$ as measured by DSC⁷⁰ (Table 4).

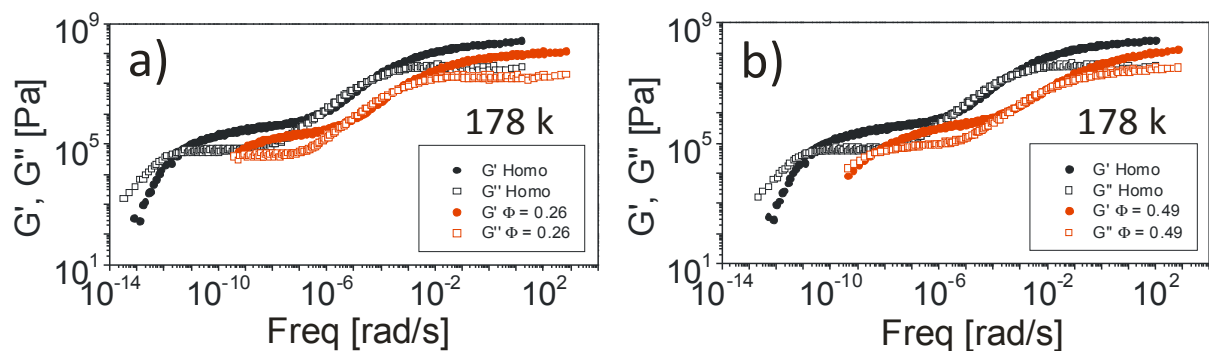


Figure 39. Mastercurves for blends of PEMA-g- μ gels with homopolymers of $M_w = 177800$ g/mol (red) for core volume fractions of $\phi_c = 0.26$ (a) and 0.49 (b) compared to the neat homopolymer (black).

We can calculate the plateau moduli for the sample with $M_w = 177800$ g/mol, which represents the vertical shift of the mastercurve. We see that due to addition of PEMA-g- μ gels ($\phi_c = 0.26$), the modulus reduces from $4.0 \cdot 10^5$ to $2.0 \cdot 10^5$ Pa. This reduction is attributed to the poor interaction of the PEMA-g- μ gels with the surrounding high M_w matrix. The aggregates we have seen in SPM and GISAXS measurements in this case are hindering the matrix to entangle and thus causing defects in the melt which are leading to a decreased modulus. If the core volume fraction is increased to 0.49, the modulus of the PEMA-g- μ gel clusters is contributing to the modulus of the composite, since almost half of the composite consists of PEMA-g- μ gels. In this case the plateau modulus is calculated to be $3.4 \cdot 10^5$ Pa.

DMTA of blends made from two homopolymers with different molecular weight

The reduction of T_g of around 5 °C for $\phi_c = 0.26$ is a surprising result and the question arises, why the glass transition temperature should decrease due to the addition of PEMA-g- μ gels.

The first possibility for the decrease in T_g is that by blending the PEMA-g- μ gels into the homopolymer, we also introduce polymer chains (polymer brushes) with lower molecular weight than the matrix. Since we know the T_g (342 °K) of the homopolymer with similar molecular weight ($M_w = 36400$ g/mol) compared to that of the brushes, we expect a slightly higher T_g for the polymer brushes ($M_w = 37700$ g/mol) but well below that of the 178k matrix (353 °K). We have calculated the

number of brushes which were grafted on a μ gel-particle before to $f = 4\pi r^2/\Gamma = 1724 \pm 255$ which equates to $1.183 \cdot 10^{-21} \text{ mol}$ PEMA. The grafted polymer brushes have a molecular weight (M_w) of 37700 g/mol which results in a mass of $4.46 \cdot 10^{-17} \text{ g}$ of brushes per μ gel particle. The μ gel particles itself have a molecular weight⁷⁴ of $5.6 \cdot 10^6 \text{ g/mol}$ which results in a mass of $9.29 \cdot 10^{-18} \text{ g}$ per particle. The ratio of brush mass to μ gel mass is therefore 4.8. Accordingly, by blending the PEMA-g- μ gel with homopolymers, we introduce 4.8 times more PEMA brushes than μ gel particles (by weight). So the first question would be, if the addition of this high amount of PEMA-brushes with $T_g = 342^\circ\text{K}$ (estimated by comparing with a homopolymer with similar molecular weight compared to the brushes) can cause the shift of the mastercurve to higher frequencies (lower temperatures). We therefore prepared a sample consisting of PEMA homopolymer with $M_w = 178\text{k}$ mixed with homopolymer of $M_w = 36\text{k}$ in a ratio that resembles the amount of PEMA brushes in the sample with $\phi_c = 0.26$ in Figure 39a. The reference temperature and all other experimental parameters were kept the same for all DMTA measurements (Figure 40).

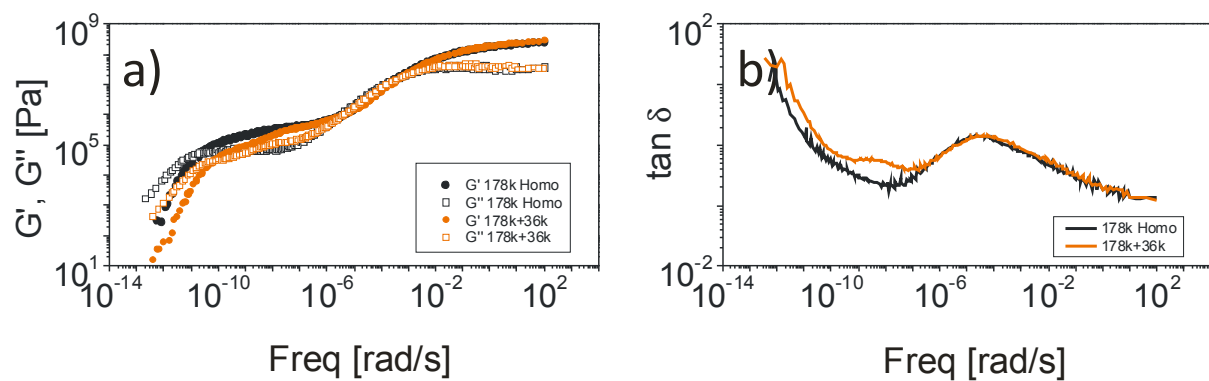


Figure 40. DMTA results of blends made from homopolymer with $M_w = 178\text{k}$ and $M_w = 36\text{k}$. a) Mastercurve of the 178k Homopolymer (black) and the 178k + 36k blend (orange). b) Loss tangent for the 178k Homopolymer (black) and the 178k + 36k blend (orange).

The glassy and the segmental flow region ($G', G'' > 10^6 \text{ Pa}$) of the 178k+36k blend (Figure 40a) have shown the same behavior as the PEMA homopolymer. For the 178k+36k blend we observe two processes for G' and G'' in the viscoelastic regime. The first one at a frequency of $7.5 \cdot 10^{-10} \text{ rad/s}$ and a second one at $6.9 \cdot 10^{-8} \text{ rad/s}$ corresponding to the two plateau moduli of $0.9 \cdot 10^5$ and $3.6 \cdot 10^5 \text{ Pa}$ respectively. These two processes were also observed in the loss tangent curves of the sample (Figure 40b). The 178k+36k blend starts to creep earlier than the 178k homopolymer, which is attributed to the lower content of low M_w chains in the blend. The observations of two processes in the viscoelastic regime shows, that both homopolymers (178k and 36k) contribute to the shape of the master curve. Since no horizontal shift was observed compared to the PEMA-g- μ gel composite in Figure 39 we conclude that the PEMA brushes did not cause the horizontal shift of the composite.

The second possibility for the decrease in T_g is the addition of nanoparticles that affect the segmental motion of free polymer chains. Liang et al.⁷⁵ prepared nanocomposites composed of

oligomeric silsesquioxane nanoparticles and cyanate ester resins. Cyanate esters can be cured by heating which results in a cross-linked thermoset material with very high T_g . The authors could show that the T_g of the composite is decreasing with increasing amount of nanoparticles. They explain the reason for this decrease of T_g by an increase of free volume due to the addition of the nanoparticles, which in turn increases the segmental motion. To check if these findings can be reproduced with our system to explain the horizontal shift of the PEMA-g- μ gel composite in Figure 39 we mixed μ gel particles without polymer brushes into a homopolymer with high molecular weight and performed DMTA measurements (Figure 41).

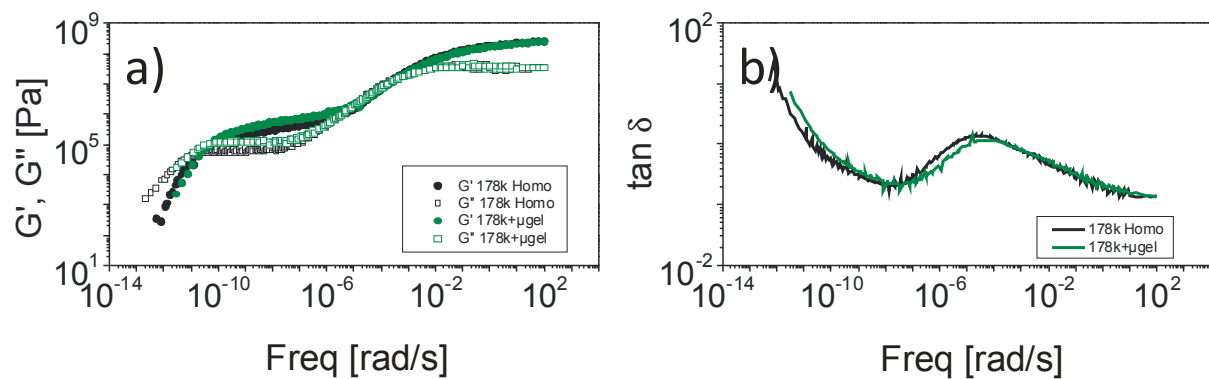


Figure 41. DMTA results of the 178k homopolymer compared to a blend made of 178k homopolymer and unmodified μ gel particles at a volume fraction of 0.26 . a) Mastercurve for G' and G'' of the 178k homopolymer sample (black) and the μ gel-particle blended sample (green). b) Loss tangent curves of the 178k homopolymer sample (black) and the μ gel-particle blended sample (green).

From the storage modulus curve in Figure 41a we deduced the plateau modulus G_N of the sample which is blended with unmodified μ gel-particles to $6.0 \cdot 10^5$ Pa and a G_N of the homopolymer of $4.0 \cdot 10^5$ Pa. We also observed a small shift to higher frequencies for the blend with unmodified μ gel particles compared to the homopolymer. We could not observe a vertical shift of the mastercurve to lower moduli as seen for the 178k sample which was blended with PEMA-g- μ gels in Figure 39.

We may therefore conclude that the vertical shift of about $3 \cdot 10^3$ rad/s observed in Figure 39 is caused by an effect which can not be explained by the separate contributions of unmodified μ gel particles or small M_w brushes as shown in Figure 40 and Figure 41. However, the values for the glass transition temperature presented in Table 4 suggest that the shift is caused by the reduction of the T_g . We also see from the values of that the reduction of T_g is much smaller for the 36k sample ($\Delta T_g = 1-2$ °C) and for the 19k sample ($\Delta T_g = 1-2$ °C) which confirms the results from the DMTA measurement where the vertical shift of the blended samples was also much smaller compared to the 178k sample.

Table 4. T_g measured by DSC⁷⁰ for the samples analyzed with DMTA. ¹ Values taken from Table 3

M _w [g/mol]	177800	36400	18600
T _g (Homo) [°C] ¹	83	69	67
T _g (Φ _c =0.26) [°C]	81	67	66
T _g (Φ _c =0.49) [°C]	76	68	68

Summary

The DMTA measurement of blends with a N/P ratio ≥ 1 have shown that the elastic modulus is not significantly changed due to the addition of PEMA-g- μ gels. For a ratio of $N/P = 2.03$ the creep behavior of the blend was improved which is a hint to increased cross-linking of the composite⁷³. We proved that the elastic modulus for these composites is almost the same as for the homopolymers. Thus I could show that the first condition we made in the beginning of this chapter is fulfilled. A study of the surface wear will be discussed in the next chapter.

5. Nanowear in Nanocomposite reinforced Polymers

To investigate the influence of PEMA-g- μ gels on the wear resistivity of blends made from homopolymers and PEMA-g- μ gels we carried out a nanowear test⁷⁶ as a proof of concept. The samples were containing PEMA-g- μ gels and PEMA homopolymers with different M_w . The idea of this nanowear test is depicted in Figure 42. A surface is scanned by an SPM tip with a force F normal to the surface at a velocity v .

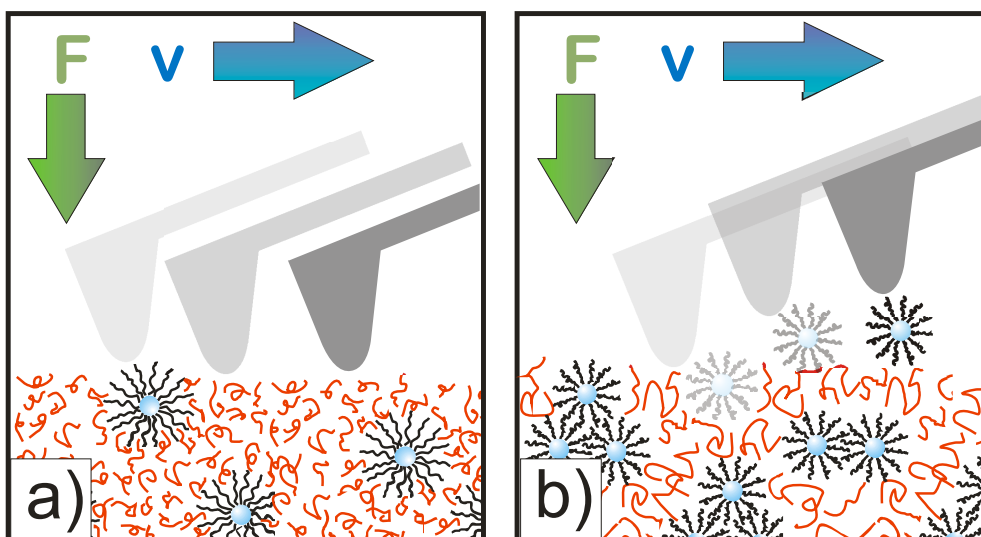


Figure 42. Schematic illustration of PEMA-g- μ gels dispersed in a homopolymer matrix scanned by an SPM tip with normal force F and velocity v . a) At low matrix M_w the brushes are swollen by the matrix and incorporated strongly. b) At high matrix M_w brushes are not swollen by matrix molecules

In case of PEMA-g- μ gels dispersed in a low M_w matrix (Figure 42a), we expect the brushes to be swollen by the matrix molecules. Thus, the PEMA-g- μ gels are strongly incorporated in the matrix and the scanning tip may not tear off single PEMA-g- μ gels. On the other hand, when the matrix M_w is high, the brushes are not swollen by the matrix molecules and the PEMA-g- μ gels are forming clusters. Single PEMA-g- μ gels might be torn off by the SPM tip and be moved over the surface (Figure 42b).

In the first part of this chapter I will show that the concept for a nanowear test depicted in Figure 42 is applicable to distinguish different compositions of nanocomposites which are described earlier in this work. In the second part of this chapter I will introduce a modification of the nanowear experiment which allowed us to compare different compositions of nanocomposites quantitatively.

5.1 Nanowear due to constant applied normal forces

Prior to the nanowear test, we imaged an area of $2 \times 2 \mu\text{m}^2$ of the samples in tapping mode (Figure 43a). Subsequently, we performed the wear test by scanning an area of $1 \times 1 \mu\text{m}^2$ with a defined force of 10 nN for 10-100 times in contact mode (Figure 43b). The scan velocity in the direction of the fast scan axis was $10 \mu\text{m/s}$. Finally an image of $2 \times 2 \mu\text{m}^2$ was acquired in tapping mode, including the previously scanned area (Figure 43c). The samples were tested with a scanning force microscope (Dimension 3100, NanoScope IIIa controller, Veeco, USA) using commercial silicon tips (OMCL AC 240 TS, Olympus, Japan).

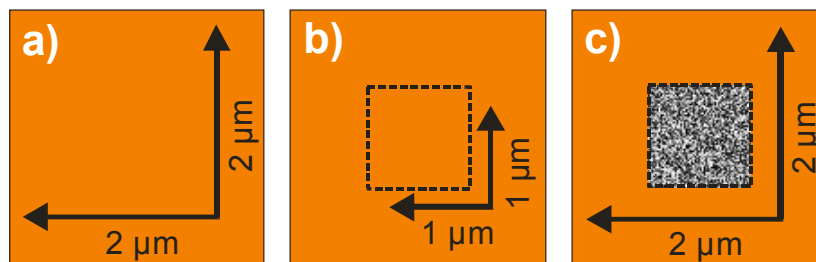


Figure 43. Schematic representation of the nanowear experiment. a) Imaging of an area of interest. b) Scanning an area of $1 \times 1 \mu\text{m}$ at elevated forces. c) Imaging the area of interest again.

To adjust the normal forces precisely we determined the spring constant and the resonance frequency of each individual cantilever experimentally by the thermal noise method⁷⁷ before each measurement. From the average of 5 individual taken thermal noise spectra (Figure 44) we calculated an error for the spring constant, which results in an error for the applied normal force < 1 nN for all following experiments.

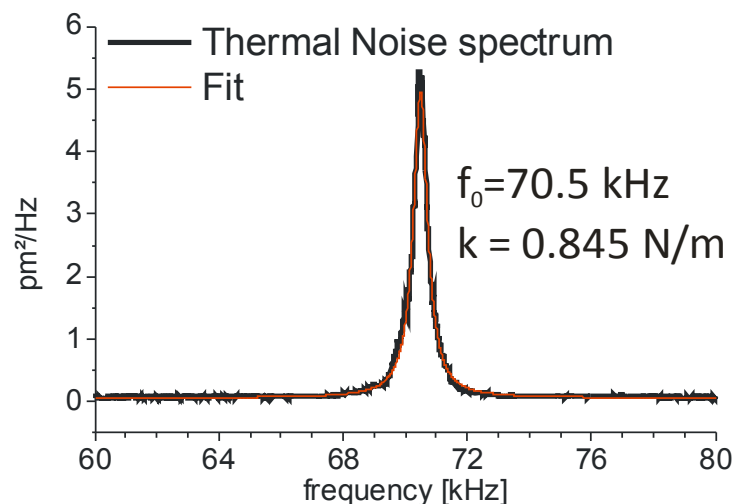


Figure 44. Raw and fitted thermal noise spectrum and for a typical SPM cantilever used in the nanowear experiments.

We investigated the samples with a core volume fraction of 0.26 mixed with a 12k matrix (Figure 45a, b) and a 98k matrix (Figure 46a, b). In contrast we prepared a sample with unmodified μgel -particles

at the same core volume fraction and a low matrix M_w (Figure 47a, b). The samples were annealed for 12h at 90°C, which is above the glass transition temperature of the PEMA. For the sample composed of PEMA-g- μ gels and low M_w matrix (12k), the nanowear test revealed that the worn area is stable against repeated scanning at 10 nN normal force. We could observe slight trenches at the left and right face of the worn area which originate from higher torsional forces of the tip at its turning point. Further damage of the worn area could not be observed (Figure 7a, b). The PEMA-g- μ gels may have a strong connection with the matrix, i.e. the brushes are swollen by the short matrix molecules. Also after annealing the sample above the T_g of the matrix the surface changed significantly as can be seen by comparing Figure 45a and Figure 26, 12k. The PEMA-g- μ gels almost disappeared from the surface due to better incorporation into the matrix. However, scanning at higher forces than 10 nN revealed that PEMA-g- μ gels are still close to the surface but covered with matrix polymer.

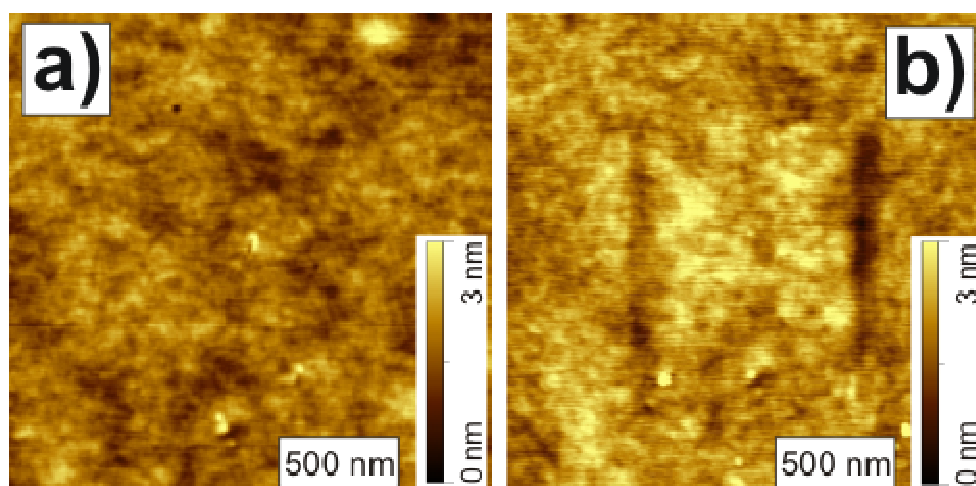


Figure 45. PEMA-g- μ gels dispersed in homopolymer matrix of 11700 g/mol. a) Sample before and b) after the wear test. The inner square in (b) was scanned 100 times with a normal force of 10 nN.

For the sample composed of PEMA-g- μ gels and high M_w matrix (98k) we observed torn of PEMA-g- μ gels even after 10 subsequent scans (Figure 46a, b). We could also observe holes within the worn area which indicates that PEMA-g- μ gels were torn of and moved over the surface by the SPM tip. For these images we chose a higher magnification that allowed us to address single PEMA-g- μ gels and identify the corresponding holes. Upon annealing the samples above the T_g of the PEMA matrix, no significant changes in the surface morphology could be observed.

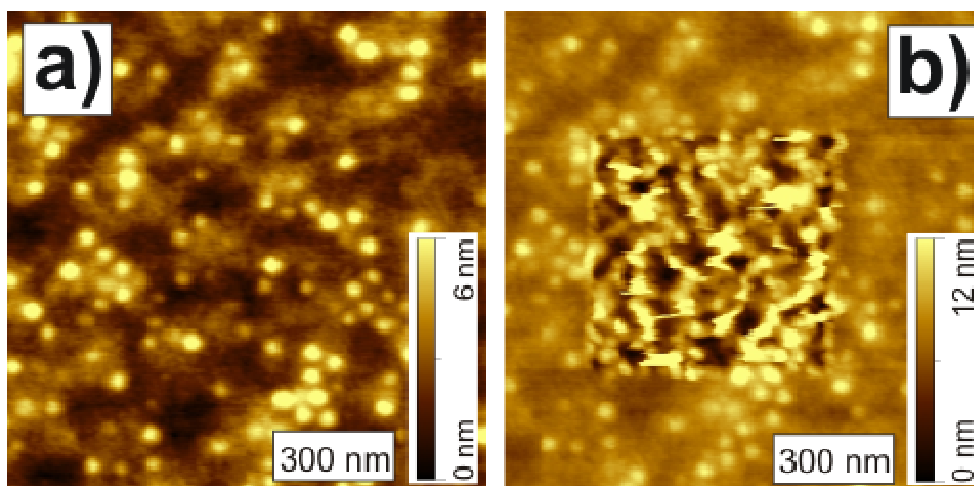


Figure 46. PEHA-g- μ gels dispersed in homopolymer matrix of 98400 g/mol. a) Sample before and b) after the wear test. The inner square in (b) was scanned 10 times with a normal force of 10 nN.

In contrast, the samples with unmodified μ gel-particles showed totally different behavior (Figure 47a and b). First, the μ gel-particles formed clusters similar to the PEHA-g- μ gels which were dispersed in high M_w matrix (Figure 47a, b). Second, due to the weak interaction of the unmodified μ gel-particles with the homopolymer matrix, the particles were torn of easily and moved to the left, right and upper face of the worn area.

The results of the nanowear tests can be regarded as direct proof of the changes in interaction between matrix and brushes, and thus to changes in brush conformation related to the molecular weight of the matrix. The μ gel particles with contracted brushes behaved more like hard spheres, thus allowing us to detach individual particles from the surface of such a composite film with a SPM tip.

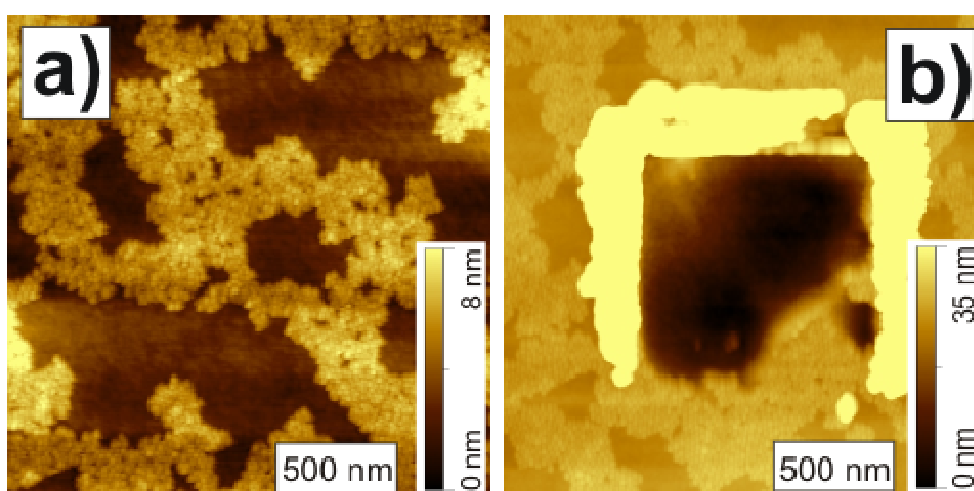


Figure 47. Unmodified μ gel-particles dispersed in homopolymer matrix of 11700 g/mol. a) Sample before and b) after the wear test.

The above presented results have shown that there is a remarkable effect of the N/P ratio on wear of the surface of nanocomposites composed of PEHA-g- μ gels and PEHA homopolymers. In samples

where the brushes are swollen by the matrix (i.e. $N/P > 1$), the surface was stable against wear of a SPM tip which scanned the surface 100 times with a normal force of 10 nN. In contrast, samples with a high matrix M_w (i.e. $N/P < 1$) have shown rupture of PEMA-g- μ gels and surface damage already after 10 scans at the same normal force. These results imply that there must be a certain onset for wear at the surface of such nanocomposites. This onset could be either a function of the number of scans or the applied normal force during a nanowear test. It might be therefore advantageous to identify parameters that can quantitatively describe the onset of surface wear.

5.2 Quantification of nanowear for varying N/P ratios

The quantification of wear is typically performed with macroscopic tests on a micrometer scale (e.g. scratch test, abrasion resistance)^{78, 79}. In the latter methods, a sample is subjected to conditions that resemble friction/wear of consumer products in practical use. Then, the consequences of the macroscopic tests are investigated by scanning electron microscopy to relate the applied wearing-/scratching force to quantitative values like the wear volume or the friction coefficient. However, with these methods it is not possible to characterize the reinforcement behavior on a nanometer scale which would be required for a directly investigation of the role of the nanoparticle - matrix interaction. One way to investigate reinforcement effects at a length scale of nanometers is the use of high resolution microscopy methods, such as scanning probe microscopy (SPM). Hereby SPM is not only used for imaging, in addition it is applied to wear the surface of samples. Recent nanowear investigations were performed only on neat materials⁸⁰. Nanowear patterns of polystyrene thin films with different molecular weight above and below the entanglement molecular weight (M_e) were analyzed. The measured nanowear patterns differ with molecular weight of the polystyrene although the density of entanglements is not M_w -dependent⁸¹. Gotsmann and Duerig⁸² used thermally cross-linkable polymers to control nanowear. In order to quantify nanowear patterns they defined nanowear as the maximum topographical height change that is observed by SPM imaging. One of the key parameters that defines nanowear mechanisms on polymers of different architecture is the cross-linking density^{76, 83}. Preparative ways to control the cross-linking density are plasma polymerization processes or the addition of chemical cross-linkers during the synthesis of polymers. Both preparation methods lead to covalent and permanent crosslinking between polymer chains. In contrast to covalent crosslinking, here we investigate the PEMA-g- μ gel particles dispersed in a polymer matrix. The interaction between the matrix polymers with the grafted polymers introduces additional anchoring sites in the nanocomposite material. In such a nanocomposite material the nanoparticle – matrix interaction is substantially enhanced by the entanglement of the grafted polymers and the matrix polymer⁸⁴. We expect that the effect of reinforcing depends on the wetting behavior of the nanoparticle surface, which is determined by the molecular weight ratio N/P . In

order to probe the reinforcement at the level of nanoparticles we performed nanowear experiments for different molecular weight ratios N/P .

To make sure that smooth and intact surfaces were chosen, all nanowear experiments started by first scanning an area of $2 \times 2 \mu\text{m}^2$ in intermittent contact mode (Figure 49a). Typically we found a surface roughness between 0.3 nm and 1.5 nm for the $2 \times 2 \mu\text{m}^2$ area. Then, in the center of the $2 \times 2 \mu\text{m}^2$ area, a nanowear test was performed in contact mode by scanning an area of $1 \times 1 \mu\text{m}^2$ with a scan frequency of 1 Hz in the fast scanning direction (Figure 49b). We started the nanowear test always by using the lowest possible normal force ($< 2 \text{ nN}$) corresponding to the magnitude of adhesion forces obtained by force distance curves (Figure 48). Typically at this normal force no surface modification was observed.

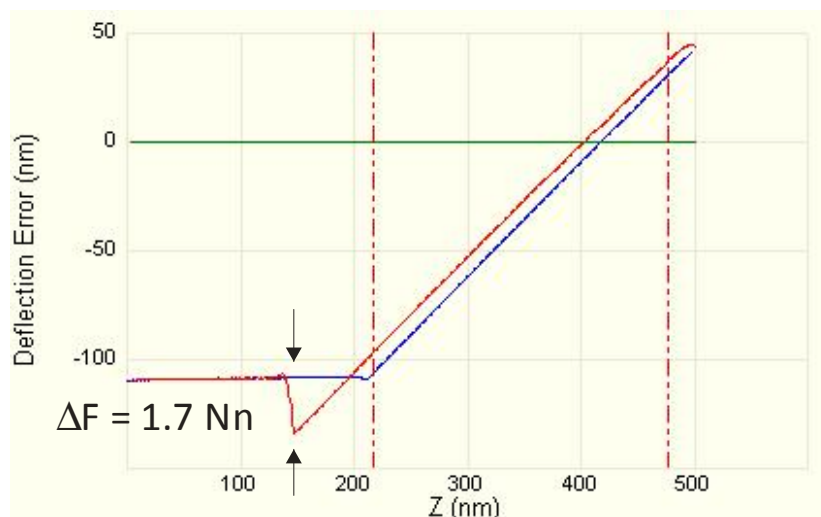


Figure 48. Force-Distance curve and acquired on a composite sample with $M_w = 36\text{k}$ and $\phi_c = 0.26$.

In our experiment a scan of 50 lines correspond to a distance of 100 nm in slow scan direction, leading to a scanned area of $0.1 \mu\text{m} \times 1 \mu\text{m}$. Scanning such an area would most probable include at least two neighboring nanoparticles in the vertical direction owing to a maximum next neighbor distance of 63 nm. After scanning 50 scan lines at the lowest force value (scan line 0-50), the scanning force was increased for the next 50 scan-lines (scan line 50-100). In order to study nanowear at different normal forces we continued to increase the normal force stepwise for each subsequent 50 scan lines (100 – 150, 150 – 200, ..., 450 - 512). The last area was scanned at the highest normal force and contained 62 lines. Finally, the impact of the nanowear experiment was imaged in intermittent contact mode at a scan area of $2 \times 2 \mu\text{m}^2$ (Figure 49c).

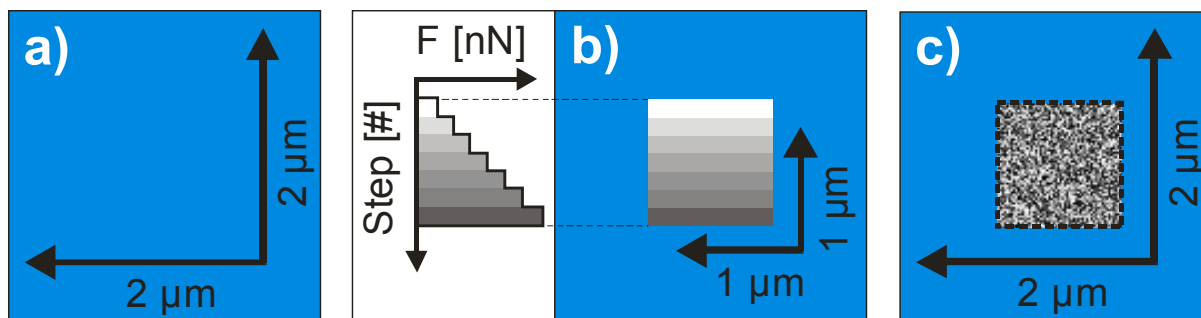


Figure 49. Schematic representation of the modified nanowear experiment. a) Imaging of an area of interest. b) Wearing an area of $1 \times 1 \mu\text{m}$ at stepwise increased forces. c) Imaging the area of interest again

We investigated PEMA-g-particles which were blended with PEMA homopolymers having different molecular weights. We have already seen in SPM and GISAXS measurements, when the M_w of the grafted brushes is larger than the one of the polymer solution ($N/P > 1$), the nanoparticles form a stable dispersion. At this ratio the PEMA homopolymer penetrates the PEMA brush that is grafted on the particle and leads to swelling. One consequence of the swelling is that the particle-particle distance increases. As a second consequence, the interpenetration of PEMA homopolymer and the brush layer could lead to a reinforcement of the entire system. In order to prove the possible reinforcement effect on a nanometer scale we performed the above described nanowear experiments.

5.3 Low molecular weight homopolymer blends

As a first sample we used PEMA-g-particles for the nanowear test with $N = 37700 \text{ g/mol}$ blended with homopolymers of $P = 11700 \text{ g/mol}$ leading to a ratio of $N/P = 3.2$ (Figure 50a). The topography of the stepwise worn area was found to be stable up to step 2, corresponding to a normal force of 7 nN. At a normal force of 22 nN (step 4) we found nanowear of the surface corresponding to removal of material. The worn material was accumulated in a pile up of material at the left and right side of the scanned area. The rms roughness of the worn area remained almost constant until the normal force reached 29 nN (step 5). At higher magnification the worn area showed that the morphology of the surface changed upon wear of the SFM tip at a normal force of 15 nN (step 3). With increasing force we observed spherical features with increasing size ranging from ~ 10 to about $\sim 50 \text{ nm}$. However, the small features within step 3 and step 6 were not attributed to be PEMA-g-particles because they were too small and their distance resembled not the interparticle-distance of the PEMA-g-particles in the unworn area. At normal forces $> 44 \text{ nN}$ (step 7) some of the spherical features have a similar size than the PEMA-g-particles. Nevertheless, most of the features were still smaller than the PEMA-g-particles and their interparticle-distance was almost zero. A detailed analysis of the material that piled up at the left and right side of the scanned area showed that for normal forces $< 44 \text{ nN}$ no

PEMA-g-particles were removed from the matrix. Although the piled up material had a spherical shape, the size of these features was always smaller than the size of a PEMA-g-particle. We associate the piled up material to be homopolymer matrix. At higher normal forces (> 44 nN) the features of the piled up material became bigger and reached the diameter of a PEMA-g-particle (18 ± 1 nm). Thus it was possible that some PEMA-g-particles were torn off the matrix and piled up together with homopolymer matrix.

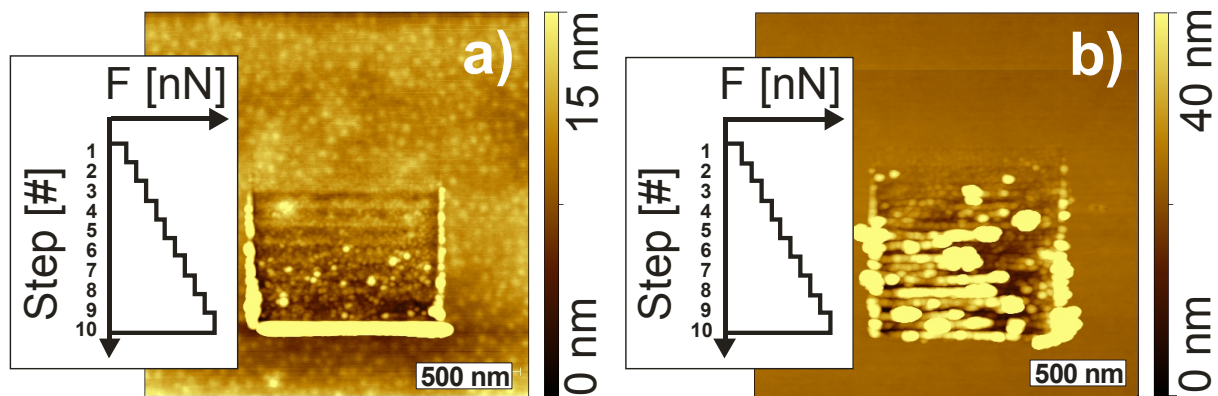


Figure 50. Nanowear test on samples with matrix M_w of 11700 g/mol. a) Topography image of a sample blended with PEMA-g-particles, b) topography image of a pure homopolymer sample. In the inner square the force was stepwise increased up to maximal normal force of 150 nN (step 10).

For a direct comparison we investigated a homopolymer reference sample (Figure 50b) made only from the matrix homopolymer ($M_w = 12k$). The topography analysis of the worn area revealed a noticeable nanowear effect already at step 1, corresponding to a normal force of < 2 nN. We observed similar nanowear patterns for normal forces above 17 nN (step 2) with small spherical features with a size of ~ 10 nm like in the sample with PEMA-g-particles. This similarity supports our above conclusion for the sample with PEMA-g-particles, that predominantly the homopolymer matrix was moved to the left and right faces of the worn area. At a normal force of 17 nN a pile up of material and plastic deformation as well as rupture of material was observed. At a normal force of 50 nN (step 3) we observed bundle formation parallel to the fast scan direction. The surface damage gets more pronounced with further increasing force resulting in the formation of big clusters and bundles (step 4-10). A magnification of the bundles which are parallel to the fast scan direction revealed the existence of the same spherical/round features mentioned before. The bundles look like a pearl necklace with “pearls” of increasing size when the force was increased. These features might be a result of the stick-slip mechanism that takes place during the nanowear experiment. The nanowear data indicated that the composite material was more wear-resistant compared to the pure homopolymer. Thus, the addition of PEMA-g-particles lead to a reinforced surface.

A more objective and quantitative analysis of the nanowear effect would require comparing different PEMA-g-particles homopolymer mixtures. Dinelli et al.⁸¹ reported the analysis of the spacing between

bundles formed during repeated scanning of a polystyrene surface at elevated normal forces. However, the mechanisms of this bundle formation might differ when nanoparticles are present in the polymer. In particular after one scan of the surface, we did not observe the formation of bundles. Thus we analyzed the surface roughness of the worn area at different normal loads as well as the roughness within the worn area at the same normal load. From each area which was scanned with a constant normal force we calculated the line rms of 25 scan lines contained in this area. In this analysis the outer left and right sides with pile ups were disregarded in the calculations. The average of these 25 line rms values and the standard deviation of the average were taken as representatives for the nanowear effect at each normal force (Figure 51a, b). First, this plot showed that the rms line roughness increased at increasing normal force. The reduction in rms line roughness at a normal force of 65 nN can be attributed to a large area that was disrupted (Figure 50b). Second, the standard deviation, sd , indicated differences in rms roughness between lines (Figure 51b). Third, at all applied normal forces the rms line roughness of the worn homopolymer was higher than that of the blended sample. In conclusion, all these findings indicate that the PE_{MA}-g-particle - polymer mixture is reinforced compared to the homopolymer system. Based on the nanowear measurement with increasing normal force and the shape of the rms line roughness curve, we were able to define a critical force f_c for the onset of nanowear. This critical force was given by the normal force where the rms line-roughness and the standard deviation of roughness increase significantly (indicated by the arrows in Figure 51a, b). For the PE_{MA}-g-particle system ($M_w = 12k$) we determined a critical force of 29 nN. For the PE_{MA} homopolymer a significantly lower f_c was measured (17 nN). The value of the critical force was then used as an indicator for the strength of reinforcing of the PE_{MA}-g-particles dispersed in PE_{MA} homopolymers.

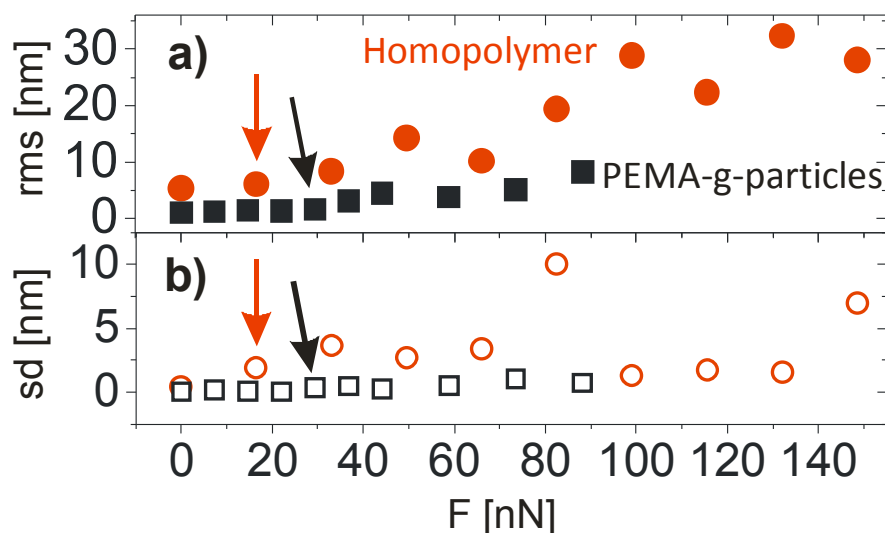


Figure 51. a) Root mean square roughness (rms) for each force step plotted against the applied force. Homopolymer: filled circles ($M_w = 12k$), PE_{MA}-g-particle blended sample: filled squares. b) Open symbols represent the standard deviation of the average. The arrows indicate the critical force f_c .

5.4. Blends with varying molecular weight

In order to investigate differences in the reinforcement of blends made of homopolymer matrix with different molecular weight we performed the nanowear test with various mixtures of PEMA-g-particles and homopolymers ($N = 37700$ g/mol and $P = 12k, 19k, 36k$ and $178k$). The experiments revealed that for matrix homopolymers with higher molecular weight the onset of nanowear was shifted to higher forces (Figure 52). This observation was supported by the analysis of the line rms values at increasing normal forces. For a matrix M_w of 18600 g/mol ($19k$, ratio $N/P = 2.03$) f_c was measured to be 12 nN for the homopolymer and 30 nN for the PEMA-g-particle blends. This force was the same f_c as measured for the $12k$ sample. In both cases the molecular weight of the matrix was below the molecular weight of the brush, i.e. $N/P > 1$. When the M_w of the matrix polymer increased to 36400 g/mol and $N/P = 1.04$, f_c was almost equal for the pure and the composite sample; $f_c = 52$ nN for the homopolymer and 58 nN for the PEMA-g- blends. At a matrix M_w of 177800 g/mol ($N/P = 0.21$) we observed that f_c was lower for the PEMA-g-particle blended sample (62 nN) compared to the neat homopolymer (85 nN). This drop in f_c (as a result of higher rms values) might be attributed to nanoparticles which were torn off during the nanowear test resulting in a higher rms roughness. The overall nanowear resistance was higher than that of the low M_w sample ($12k$) but there was no improvement in the nanowear resistance due to blending with PEMA-g-particles.

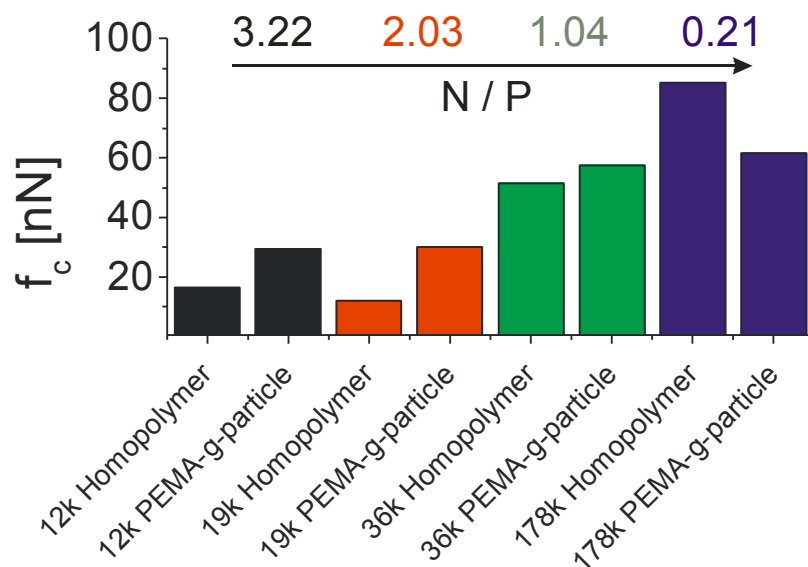


Figure 52. Critical force f_c of PEMA-g-particle blended samples and homopolymer samples in dependence of the N/P ratio.

An increased resistance to nanowear of homopolymers with increasing molecular weight was also reported by Dinelli et al. for polystyrene surfaces⁸¹. They attribute the increased resistance for polymers with M_w above the entanglement molecular weight M_e to the increased number of

entanglements. Dinelli et al. identified a threshold normal force at which a disruption of the polymer surface begins. By analyzing the distance between bundles which were formed during scanning of the surface they concluded that although the entanglement density stayed constant, for increasing M_w the molecules form more entanglements and therefore create a network that is more resistant to deformation. In our study of the pure homopolymer we could confirm these findings. For the PEMA homopolymers we have seen the same trend of an increased nanowear resistance with increasing molecular weight (Figure 52). As the number of entanglements increased with the molecular weight, the critical force f_c also increased indicating that our findings are consistent with results reported by Dinelli et al.

5.5 Reference experiments

As a reference experiment we used a blend made from PEMA homopolymer ($M_w = 12k$ and $178k$) and unmodified nanoparticles (Figure 53a, b). Without the modification of the nanoparticles with polymer brushes, the energy difference between the nanoparticle surface and the homopolymer matrix is very high. Thus, the nanoparticles were phase separated from the matrix and formed islands of densely packed nanoparticles. However, these systems showed similar nanowear patterns compared to the pure homopolymers. In addition, surface modification already started at the lowest adjustable normal forces (~ 1 nN) for the 12k sample. For the 178k sample an onset in nanowear was found at higher normal forces 13.3 nN. Rupture and torn off nanoparticles were seen when the normal force was increased further. Piling up started at a critical force $f_c = 4.9$ nN for the 12k matrix and at 13.3 nN for the 178k matrix. This difference is a direct indication that blending of unmodified nanoparticles does not improve the nanowear properties of the blends which was reported by other groups before⁸⁰, though for different nanoparticle-polymer systems.

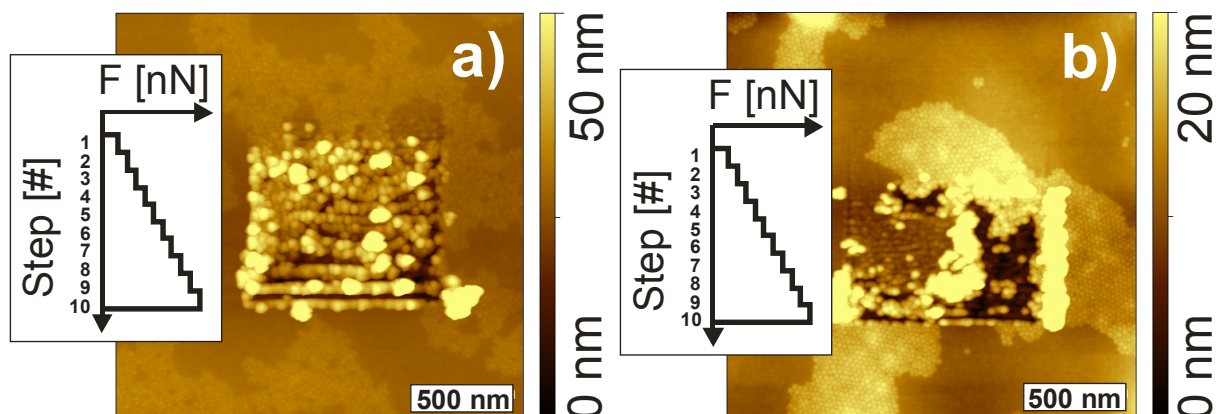


Figure 53. Topography images of PEMA homopolymers blended with unmodified nanoparticles after the nanowear experiment. a) Homopolymer $M_w = 12k$ and b) homopolymer $M_w = 178k$.

Summary

Many previous studies have been reported on the nanowear behavior of different polymeric and inorganic materials⁸⁰. However, a detailed study on nanowear of polymers being reinforced with nanoparticles has not been reported so far. Our findings were in qualitative agreement with macroscopic bulk experiments⁸⁰. We gained insight into surface nanowear effects in particular at a length scale of the nanoscopic filler particles. Using the results of the nanowear experiments we inferred the critical normal force at which individual nanoparticles were torn off the surface. Furthermore, the behavior of the studied homopolymer – nanoparticle blends indicated a reinforcement of the polymer nanocomposite material when the N/P ratio was high. At this ratio the matrix was entangled with the swollen polymer-brush. Thus, the addition of PEMA-g-particles acted as additional anchoring sites. Non-grafted nanoparticles clearly did not account for any reinforcement. Although the quantification of surface nanowear is still a challenge in material science our analysis method allows the definition of a critical force for the quantitative comparison of nanoparticle-polymer systems of different composition. Furthermore, it has the advantage of not only indicating the absolute roughness of the scanned area but also gives information of the evolution of roughness when the applied normal force is increased.

6. Plasma Deposited Polymer Layers and their Effect on Surface Wear

As we have seen in the previous chapter, the resistance of a surface against wear can be increased by the addition of polymer-grafted nanoparticles to the host material. In some cases the addition of nanoparticles can constrain the functionality of a device which is build of a thin polymer film for e.g. in nanomechanical data storage systems⁸⁵ (Figure 54). In these data storage systems a high lateral homogeneity is required to enable for writing and reading data at a high density. As a storage medium soft polymers are used were information is written in the form “geometrical bits”. Here the bit is written with a cantilever tip as an indent (1) or no indent (0) a given position. In this way a binary pattern can be created which contains the desired information. During the read out process the tip is wearing the surface which causes surface damage on the unprotected surface (Figure 54a). To protect the storage media from wear the surface of the storage media is coated with wear resistive layer (Figure 54b). The wear resistive layer hast to be very thin (1-5 nm) and needs to have a very high lateral homogeneity (roughness, thickness) to enable for writing geometrical bits with high resolution.

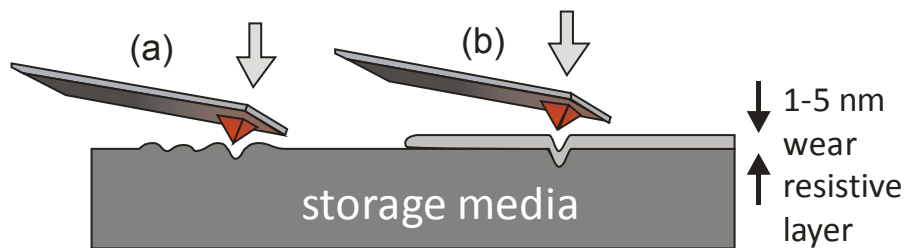


Figure 54. Nanomechanical data storage system. a) An unprotected surface of the storage medium is worn by the tip during the read out process. b) A very thin additional layer protects the storage medium from surface wear but still enables writing of data. Modified image by courtesy of Tassilo Kaule.

With these requirements we can state that a nanoparticle reinforced polymer can not be used as a wear protective layer. First, the size of the nanoparticles is larger than the maximal thickness for the protection layer which in consequence obviates high density writing since the tip has to indent much deeper to reach the storage medium. Second, the requirement for lateral homogeneity is not satisfied since particles are distributed randomly. Furthermore, the tip could hit a particle during writing an indent which causes imprecise position of the indent.

Here we introduce the field of ultra high area density storage, which is one of the major fields of interest in nanotechnology and requires detailed knowledge of mechanical properties of materials on a nanometer scale. Specific functions in such a complex device can be achieved by layered materials, where each layer fulfills a specific property. Multilayers or protection layers made from different polymeric materials are currently being investigated by different groups worldwide and are used for advanced polymer electronics⁸⁶⁻⁸⁸ and optical devices⁸⁹⁻⁹³.

Recently, scanning force microscopy (SFM) was explored as a tool to write and read information at an areal density exceeding 1 Tbit/in². It has been shown that polymer layers (e.g. polyaryl-ether-ketone) can act as a medium⁹⁴ to store information via a thermo-mechanical writing process^{85, 95, 96}. For such applications, the medium should be soft enough allowing the probe tip to deform the medium at higher loads and/or at higher temperatures. Furthermore, the roughness of the medium surface should be < 1 nm allowing for an ultrahigh storage density. Finally, the storage medium should resist copious scanning of the probe tip. The latter issue is illustrated in this manuscript by scanning a spin coated polystyrene (PS) film 100 times using a scanning force microscope tip in contact mode at a force of 10 nN and at a scan velocity of 2.5 μm/s. After this treatment, the surface was imaged at a larger area to investigate the effect of copious scanning (Figure 55a).

Clearly one can see that significant medium wear occurred in the area that was scanned repeatedly^{76, 97}. Such an increase in roughness beyond 1 nm would not be acceptable for high density storage media, because it would decrease the signal-to-noise ratio of the reading process significantly. In order to avoid wear the polymer medium can be covered by a thin, harder cover layer. The 2-layered medium consisting of the PS film covered by an ultra thin plasma polymerized hexamethyldisiloxane (HMDSO) film showed no change in surface roughness (Figure 55b) upon the same treatment. Thus the deposition of a 4 nm thick cover layer made by plasma polymerization of HMDSO^{98, 99} lead to a significant protection of a wear sensitive polymeric media.

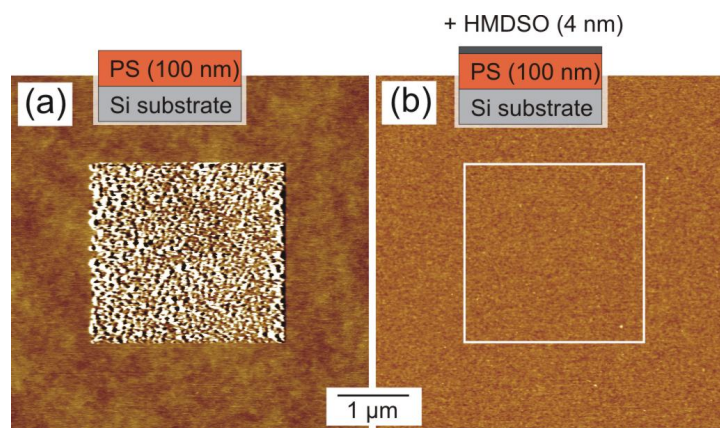


Figure 55. Surface roughening by copious scanning of a SFM-tip at a load of 10 nN, a scan speed of 2 $\mu\text{m/s}$ and after 100 recorded images of size 2.5 $\mu\text{m} \times 2.5 \mu\text{m}$: (a) Surface of a 100 nm thick spin coated PS sample. (b) A 100 nm thick spin coated PS sample having an additional 4 nm thick plasma polymerized hexamethyldisiloxane (HMDSO) layer as cover layer (deposition at RF-plasma power of 90 W). Here the surface roughness is not changed within the area that was scanned 100 times (within the white square). We determined a root mean surface roughness of $\sim 0.5 \text{ nm}$ on a 1 $\mu\text{m} \times 1 \mu\text{m}$ area. Z-scale for both images is 10 nm. For these experiments we used SFM-tips having a typical radius of curvature $< 8 \text{ nm}$. Imaging scans were performed at a scan velocity of 1 Hz with 512 lines per image. The wear experiment were performed with the same tips using 512 lines per image, a force of 10 nN and a scan velocity of 2.5 $\mu\text{m/s}$.

As illustrated above the mechanical properties of layered materials may play a major role in the working concepts of devices. In the concept taken from life science, a thin cover layer was required to be sufficiently soft to allow for scratching with a SFM tip, whereas in the concept of high density data storage, this effect should be avoided.

Here hexamethyldisiloxane (HMDSO) was selected as the monomer of choice since it is an already well known material for microelectronics and other applications. We investigated multilayers of nanometer thick films made from HMDSO monomer deposited in a one-pot plasma deposition process by using different plasma conditions in alteration. Hereby the chemical structure and the film properties of the individual layers can be tailored and it is possible to design a stacked layer structure of alternating hard and soft films. The surfaces of plasma deposited (multi-) layers have previously been studied intensively^{100, 101}. Hard, SiO_x like layers can be fabricated^{102, 103} for applications such as antireflective coatings¹⁰², barrier layers¹⁰³, corrosion protection films¹⁰⁴ and biocompatible films¹⁰⁵. The chemical composition of films made from HMDSO can be tuned either by the HMDSO/ O_2 gas ratio and/or the RF-input power of the plasma deposition process^{98, 106-109}. Changes in the RF-input power from 30 W to 180 W changes the chemical composition of the deposited film from having a substantial hydrocarbon component to films having a almost no hydrocarbon content⁹⁸.

6.1 Preparation of the plasma polymer films

Plasma deposition of multilayers made from HMDSO monomer (ACROS Organics, Germany) on silicon wafers was carried out in a plasma reactor that was described in detail elsewhere¹¹⁰. The reactor is a 30 cm long and 10 cm diameter pyrex glass cylinder that is equipped with two metal electrodes (braid rings) to deliver a 13.56 MHz radio frequency (RF). The power is supplied via an RF-

power generator (ENI 300 W) and a home-made manual matching network. The plasma deposition process allows for the introduction of different monomers and variation of the plasma deposition parameters in order to deposit films of different chemical and physical properties in a one-pot process.

In order to study the mechanical properties of plasma polymerized layers three different films were made from HMDSO: Firstly, films were made with an RF-input power of 48 W (HMDSO_{48W}). Secondly, films were made where the RF-input power was 90 W (HMDSO_{90W}). Thirdly, at the same RF-input power films were made with additional O₂ gas present in the reactor (HMDSO_{90W+O}). For this latter deposition the O₂ gas to HMDSO ratio was 5:1 at a pressure of 0.3 mbar. Higher input power and the simultaneous supply of O₂ is known to increase the oxygen content in the deposited layers. In each case, the plasma deposition time was controlled to ensure a film formation in the thickness range of 20 – 100 nm. Deposition rates were typically between 50 to 60 nm/min for the plasma deposition of HMDSO_{90W+O}. For the fabrication of multilayers the above described deposition parameters were adjusted sequentially. Thereby, multilayers consisting of 6 up to 20 layers were deposited on silicon wafers (N/Sb <100>, Si-Mat SILICIUM WAFERS, CZ). For simplicity, we introduce the following nomenclature for different multilayer films: Si_nA_n, where n stands for the number of bilayers and A and B are 48 W, 90 W or 90W+O, respectively. After deposition, the thicknesses of polymer stacks were measured with a Surface profiler (P-10, KLA Tencor, USA).

For scanning force microscopy (SFM) characterization, the silicon substrate with multilayers of Si[HMDSO_A/HMDSO_B]_n films was scratched along the Si lattice line with a diamond scribe and was fractured by hand along one axis of the silicon atomic lattice. The face side of one of the fractured pieces was investigated by means of SFM (Dimension 3100, Veeco, USA). Silicon cantilevers with a nominal spring constant of 42 N/m were used (OMCL 160, Olympus, Japan). All SFM pictures were recorded in tapping mode ($A_{sp}/A_0 \sim 0.9$), where A_{sp} is the setpoint amplitude of the cantilever during imaging and A_0 is vibration amplitude (~ 20 nm) at a tip sample distance of 100 nm¹¹¹.

6.2 Characterization of plasma polymerized multilayers

To verify the thickness and the properties of each layer more precisely a direct visualization of the variation in mechanical properties for each layer would be beneficial. Scanning force microscopy (SFM) offers spatial resolution in the nanometer realm. Furthermore, variations in the local mechanical properties can be imaged by monitoring the phase behavior of a vibrating SFM-tip¹¹¹. Substrates were fractured in order to characterize the thickness and the interface roughness of the films that were deposited as described above. The fractured face sides of the samples were imaged by means of SFM (Figure 56a).

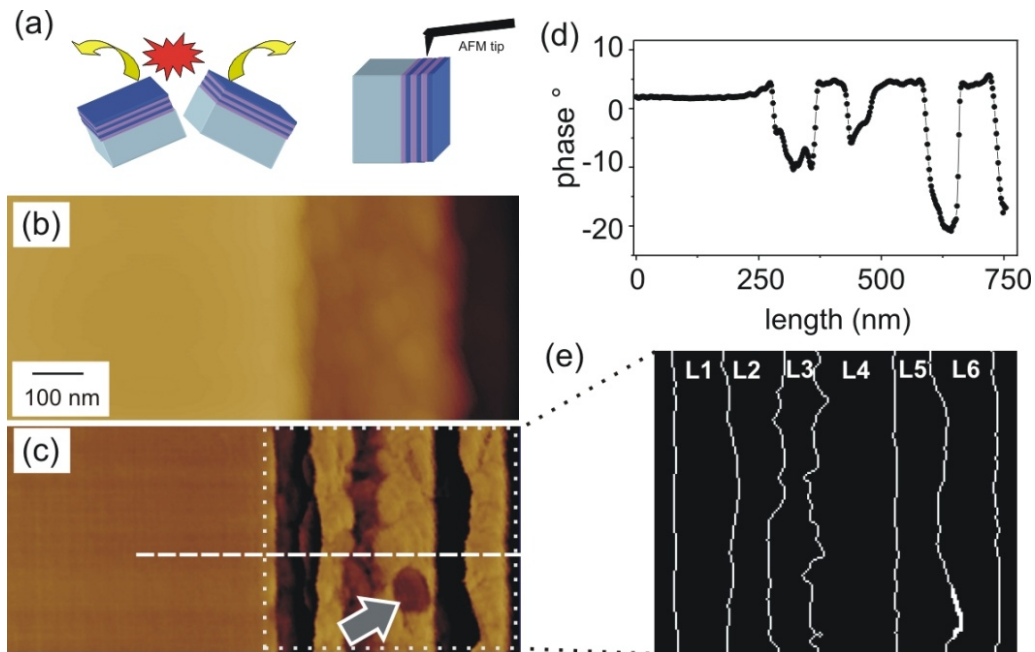


Figure 56. (a) Schematic drawing of the fracture of the sample into two parts and the subsequent imaging of the face side by SFM. (b) Topography image of the face side of the multilayered film Si[HMDSO_{90W}/HMDSO_{90W+O}]₃. Z scale 200 nm (c) Corresponding phase contrast image. Z scale 15°. (d) Line profile along the white dashed line in the phase contrast image. (e) The contour lines of the phase contrast image have been estimated using Image Pro software and were exported for roughness analysis.

The fracture process resulted in a rough surface. Different layers of the Si[HMDSO_{48W}/HMDSO_{90W+O}]₃ samples could not be identified clearly in the topography image (Figure 56b). However, the phase contrast image shows a phase difference of more than 10° between different layers (Figure 56c and d). The phase contrast between the Si-substrate (left part in Figure 4c and d) and the three HMDSO_{90W+O} layers (L2, L4, L6) appears similar, which indicates similar mechanical properties of the materials. The layers corresponding to a decreased phase shift (L1, L3, L5) are attributed to the three softer layers (HMDSO_{48W}). An analysis of layer thicknesses measured from the phase contrast image resulted in values of 77 nm for L1, 62 nm (L2), 66 nm (L3), 100 nm (L4), 62 nm (L5) and 77 nm (L6) in agreement with the values estimated from deposition rates as measured using the surface profilometer Table 5. Furthermore, the phase contrast image revealed a defect that is buried in a HMDSO_{90W+O} layer (L4) that was not observed in the topography image (grey arrow in Figure 56c).

Table 5. Summary of layering sequence and layer thickness measured from SFM images of the samples deposited in the same time

		L1(nm)	L2(nm)	L3(nm)	L4(nm)	L5(nm)	L6(nm)
Nominal thickness Si[HMDSO _{48W} /HMDSO _{90W+O}] ₃	HMDSO _{48W}	77±10		57±7		60±11	
	HMDSO _{90W+O}		66±12		112±9		82±9
SFM measured thickness Si[HMDSO _{48W} /HMDSO _{90W+O}] ₃	HMDSO _{48W}	77±11		66±3		62±10	
	HMDSO _{90W+O}		62±11		100±3		77±10

In the SFM analysis, all interfaces between the different HMDSO layers were resolved clearly in the phase contrast image. We found that the interface between a harder HMDSO_{90W+O} film followed by a softer HMDSO_{48W} film resulted in a sharp interface, while in the transition from a soft HMDSO_{48W} film to a hard HMDSO_{90W+O} film a comparatively rough interface was obtained. The interfacial roughness was quantified by further image analysis of the phase contrast image (Figure 56c, e). An interfacial roughness of 3.3 nm (RMS) (L4/L5) was calculated for the softer L5 (HMDSO_{48W}) on top of the harder L4 (HMDSO_{90W+O}) based on the line profile shown in Figure 56e which are ~ 300 nm long. For the interface where HMDSO_{90W+O} was deposited on top of HMDSO_{48W} film a significantly higher interfacial roughness of 11.2 nm (L1/L2) and 10.4 nm (L5/L6) was determined. For comparison, a standard SFM topography analysis of plasma deposited HMDSO films, as used here in this study, revealed always a roughness < 1 nm (e.g. Figure 55). We attribute the increase of the interfacial roughness to partial etching of the HMDSO films by the subsequent deposition process. The etching of a hydrocarbon rich HMDSO_{48W} film⁹⁸ is probably a result of the presence of oxygen during the deposition. In order to verify the above mentioned conclusions an additional sample was prepared which shows the same trend.

The content of hydrocarbons within a HMDSO film can be reduced by increasing the RF-input power of the plasma⁹⁸. In order to investigate the importance of the carbon content in the etching process of HMDSO films we investigated multilayer films deposited at a RF-input power of 90 W with alternating O₂ pressure (Figure 57). In this case we obtained a stack of layers composed of Si[HMDSO_{90W}/HMDSO_{90W+O}]₃ Table 5.

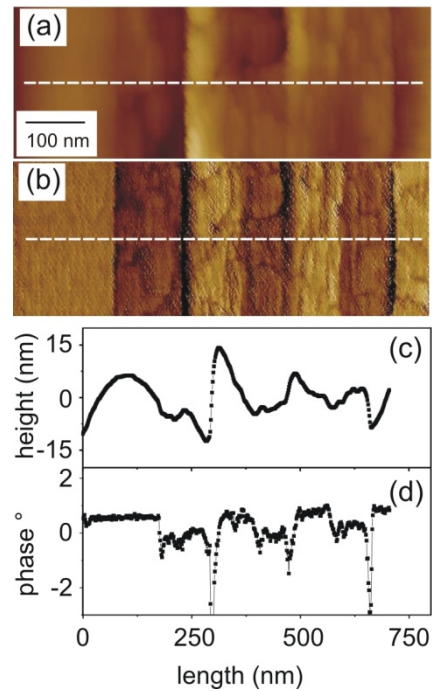


Figure 57. (a) Topography image of the face side of the multilayered film $\text{Si}[\text{HMDSO}_{90\text{W}}/\text{HMDSO}_{90\text{W}+\text{O}}]_3$. Z scale 200 nm (b) Corresponding phase contrast image. Z scale 15°. (c) Line profile along the white dashed line in the topography and (d) profile along the phase contrast image.

The corresponding SFM study revealed a reduced phase contrast of 1-2° between the HMDSO layers. The decrease in phase contrast compared to the stack composed of $\text{Si}[\text{HMDSO}_{48\text{W}}/\text{HMDSO}_{90\text{W}+\text{O}}]_3$ is attributed to more similar mechanical properties between the $\text{HMDSO}_{90\text{W}}$ and $\text{HMDSO}_{90\text{W}+\text{O}}$ layers. Furthermore we found that the interfacial roughness between adjacent layers of $\text{HMDSO}_{90\text{W}}$ and $\text{HMDSO}_{90\text{W}+\text{O}}$ does not exhibit significant differences.

Summary

This work aimed to investigate the mechanical properties of stacks of ultra thin films deposited with a plasma deposition process of hexamethyldisiloxane to study their interfaces. The mechanical properties of both the complete stack of up to 6 single layers as well as the individual thin films making up the stack were investigated. SFM phase contrast images revealed differences in mechanical properties for individual layers. These observations are in full agreement with the present understanding of the relationship between crosslink density and chemical structure of HMDSO films as a result of different input powers and gas mixture with oxygen.

The mechanical contrast as imaged by the SFM allowed us to study the interface roughness in more detail. We have shown that there are significant differences in surface and interface roughness between a hard/soft and a soft/hard materials suggesting asymmetric interfaces for adjacent layers. In contrast to our findings, a symmetric interface was found by means of secondary ion mass spectroscopy on HMDSO multilayers¹⁰³. In the latter deposition process the HMDSO precursor inlet

were controlled simply by the pumping speed. For our films the surface roughness was found to be always $< 1\text{nm}$. The typical roughness of a hard/soft interface was found to be in the order of 3 nm, while a soft/hard interface showed a roughness in the order of 10 nm. A key role in interface roughness plays the RF-input power that determines the cross linking density and the hydrocarbon content. In view of emerging applications of ultra thin plasma deposited films that were outlined in the beginning the interface properties play a crucial role for the function of a device. Here scanning force microscopy measurements of the face side of stacked layers can reveal valuable local information.

7. Towards screening the mechanical properties of polymeric materials

The characterization of nanocomposites requires the utilization of many different techniques to get an overall picture of the material and its components. Most techniques necessitate a certain amount of sample substance in the range of a few 10 to some 100 mg. We have already seen that the dispersion behavior and the resistance to nanowear of PEMA-g- μ gels in homopolymer matrices depend on the N/P ratio. To get a better understanding how material parameters like

- Matrix molecular weight (P)
- Brush molecular weight (N)
- Grafting density (Γ)
- Core volume fraction (ϕ)

will influence the properties of the nanocomposite material, a screening of these parameters would be necessary. However, if we consider 5 variations of each parameter, we end up with a number of samples in the order of $4^5 = 1024$.

Due to their chemical nature most polymeric materials can not be machined with standard micromachining techniques like focused ion beams or wet etching. Therefore the characterization of micro- or nanometer sized polymeric structures is based on well established coating techniques. Schneider et al.¹¹² reported about surface acoustic wave measurements (SAW) on pulsed laser deposited diamond like carbon and spin coated polyamide films with thickness of 5.3 and 1.8 μm respectively. Due to high damping of ultrasonic waves in polymeric materials the tested polymer films should be thin. On the other hand the penetration depth of the surface wave at 100 MHz is around 50 μm so the motion of the wave is mainly guided by the substrate and the effect of the film is small.

To check if the SAW method is applicable to polymers, we tested spin coated PEMA films on silicon and plasma polymerized norbornene (pp-norbornene) films by the *Laser Actuated Surface Acoustic Wave*¹¹² (LASAW) method. We chose PEMA as a relatively soft polymer compared to pp-norbornene¹¹³ films with thicknesses for both polymers ranging from 10-500 nm. For both, the soft PEMA and the hard pp-norbornene, we observed thermal degradation and destruction of the films

due to laser induced heat. Furthermore, the calculated elastic moduli were not consistent. These results demonstrate that LASAW is not applicable to screen the mechanical properties of polymer films with a thickness of 10-500 nm.

Tranchida et al.¹¹⁴ made a critical approach to the elastic characterization of polymers using nanoindentations. They investigated a variety of spin coated polymers from rubbery to semicrystalline and amorphous networks. By using Sneddon's elastic contact mechanics approach and gathering load-penetration curves they were able to calculate the elastic modulus of several polymeric materials like PMMA, PC, PP, LDPE, PEG and PTFE. However, the nanoindentation method requires very accurate calibration of the system and the knowledge of several experimental parameters. Furthermore this technique is gives values only on a local scale and is very time consuming. With nanoindentation measurements one could get information of local mechanical properties of a nanocomposite, e.g. in the vicinity of a nanoparticle, but large-area or bulk values are not accessible.

7.1 Analyzing the Mechanical Properties and the Cross-link Density of Ion-irradiated Polystyrene Surfaces from Rippling

The phenomena of buckling instability¹¹⁵⁻¹¹⁸ was demonstrated to work as a testing platform to determine the mechanical properties of polymeric thin films without the need for expensive test equipment. This phenomenon can be explained for an elastic surface as follows. If a compressive force parallel to the surface on the skin layer/bulk material composite exceeds a critical value, then ripples appear on the skin (Figure 58). The ripple periodicity depends on the material properties of the skin and the bulk material (their Poisson ratio and Young modulus) and the thickness h of the skin but is independent of the applied stress and strain¹¹⁹. The quantitative relationship between the measured ripple periodicity λ , induced by the buckling instability and the Young modulus of the buckled layer in the surface (E_s) is given by¹²⁰

$$E_s = 3E_b \frac{1 - \nu_s^2}{1 - \nu_b^2} \left(\frac{\lambda}{2\pi h} \right)^3 \quad (7.1)$$

where ν_b and E_b are the Poisson ratio and Young modulus of the bulk substrate and ν_s and h are the Poisson ratio and thickness of the rippled surface layer, respectively.

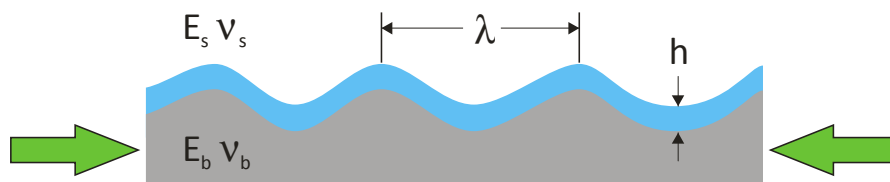


Figure 58. Scheme of the buckling instability phenomena. A thin film of thickness h forms buckles with a periodicity λ on a soft substrate upon compression.

The buckling instability phenomenon has been widely used in the development of complex patterns on different systems (e.g., thin metal film deposited on a polydimethylsiloxane (PDMS) substrate¹²¹ and plasma-treated PDMS film on untreated PDMS bulk¹²²). The Young modulus of thin PS films deposited on PDMS substrates has been calculated by exploiting the relationship among the periodicities of the ripples on the thin PS films and the film thickness, the Poisson ratios of the film and PDMS, and the Young modulus of the PDMS^{116, 123}. Recently, the rippling concept was used to determine the mechanical properties of a polyelectrolyte multilayer¹²⁴⁻¹²⁶. Here, we explore the concept of buckling instability on polymer surface layers, which were locally irradiated by ions, to estimate their Young modulus. Understanding the mechanical properties of these locally cross-linked polymers is important because they find applications in improving the local roughness for improved adhesion¹²⁷ or commercial water-treatment membranes¹²⁸.

Ion projection direct cross-linking (IPDC)¹²⁹ was used to locally cross-link skin layers of stretched polymer substrates on the submicrometer scale¹³⁰. A different degree of cross-linking should be reflected by a change in the mechanical properties of the cross-linked layers similar to what we observed for the wear resistance of nanoparticle reinforced polymers in chapter 6.

The substrates for our experiments were prepared like the following. After compress molding (160 °C, 20 kN) of PS powder to rectangular bars with thickness of 1-2 mm, each substrate was fixed with a clamp in an extensometer (Instron 6022, Instron Deutschland GmbH, Germany) and heated to 100 °C, the glass-transition temperature of PS. After that, the PS substrate was stretched at a constant speed of 0.5 mm min⁻¹ to the desired stretching ratio of 200% (length of the substrate after stretching, divided by its original length in %). After being stretched, the clamped substrate was slowly cooled in air to 50 °C in 2 h and then to room temperature within 1 min. Such a substrate was divided into smaller pieces of 10 mm × 6 to 7 mm. Only those pieces from the central areas of the stretched substrate were used for irradiation. The ion projector allows a vertical irradiation of substrate surfaces with a lateral resolution down to 50 nm¹³¹. In our experiments, we irradiated square-shaped areas with 32 μm side lengths within the substrate surface with a separation of 12 μm.

The thickness of the cross-linked layers was controlled by using different ion species, viz., xenon (Xe^+), argon (Ar^+), and helium (He^+). The cross-linking densities were varied by varying the ion fluence. After IPDC, annealing the polymer substrate above the glass-transition temperature, T_g , resulted in the relaxation of the orientated polymer chains in the non-cross-linked volumes. In the cross-linked layer, rippling occurred.

To prove that the PS surface was cross-linked by irradiation with ions, we exposed a PS substrate to 30 keV Ar^+ -ions at a high ion fluence of 10^{15} ions/cm² and afterward dipped the substrate into toluene, a good solvent for PS (Figure 59a). An insoluble crumpled piece of PS was observed. From scanning electron microscopy (SEM), we obtained a thickness of ≈ 100 nm for this insoluble part (Figure 59b). For the Ar^+ -ions we simulated we also performed simulations of the interaction of the ion projectile with the PS^{132} to determine the thickness of the skin layer h . The maximum thickness of 105 nm obtained by the simulations is in excellent agreement with experimental results from SEM. Thus the simulations, which we used to determine h also for the other ions at different fluencies can be considered valid.

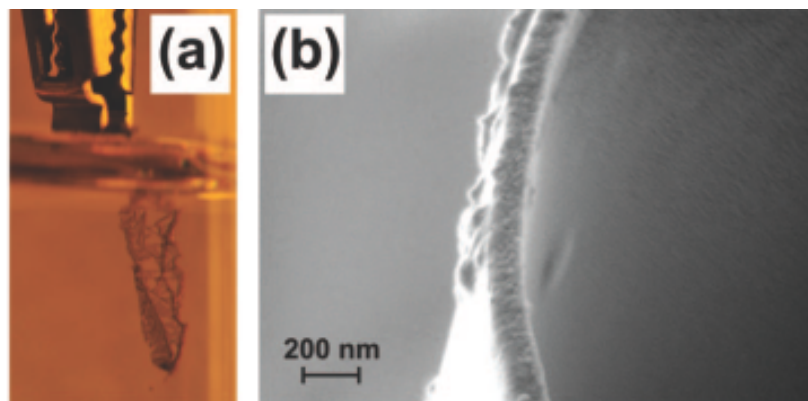


Figure 59. (a) Microscopy image of an Ar^+ -irradiated PS substrate of $1 \text{ cm} \times 1 \text{ cm}$ (30 keV , $10^{15} \text{ ions/cm}^2$) dipped into toluene. The visible crumpled part is insoluble in the solvent and proves that the PS substrate was cross-linked by irradiation with the ions. (b) SEM image of the gold covered crumpled part. The corrected thickness of the lamella is $\sim 100 \text{ nm}$ (subtraction of gold layer).

SFM Images of Xe^+ -Irradiated PS

Accelerated particles such as ions can interact with substrates in different ways. Atomic displacements can lead to a surface sputtering effect resulting in a physical etching. After the ion irradiation, we imaged a Xe^+ -irradiated PS ($10^{13} \text{ ions cm}^{-2}$) surface with scanning force microscopy (SFM) (Figure 60a). In the phase contrast image, the irradiated parts can be clearly distinguished from nonirradiated ones. The darker square-shaped area with a size of $32 \mu\text{m} \times 32 \mu\text{m}$ corresponds to the Xe^+ -irradiated PS. The phase contrast indicates a local chemical modification of the surface properties of the polymer. The irradiated parts are at most 4 nm lower than the nonirradiated ones, indicating only marginal etching. After the sample was annealed at $110 \text{ }^\circ\text{C}$ in vacuum for 1 h,

the PS substrate contracts opposite to the direction of stretching and expands perpendicular to it. This behavior is typical for amorphous polymers and indicates a relaxation of stretched polymer chains into a less stretched state^{133, 134}. Therefore, after annealing the irradiated areas appear as rhombi with an average lower diagonal length of 21.6 μm , a longer diagonal length of 65.5 μm , and a side length of 34.5 μm (Figure 60b). In addition, ripples appear in the irradiated areas (Figure 60c). They are almost uniaxial and are orientated perpendicular to the stretching direction with a periodicity of 900 ± 183 nm.

Determination of Poisson's Ratio

From the change in the shape, Poisson's ratio ν_s of the rippled skin layer was calculated according to $\nu_s = -\varepsilon_t/\varepsilon_a$, where $\varepsilon_t = (w - w_0)/w_0 = \Delta w/w_0$ and $\varepsilon_a = (l - l_0)/l_0 = \Delta l/l_0$ are the transverse and axial strains, respectively. They represent the relative changes in the width w or the length l of the irradiated area with respect to its original width or length.

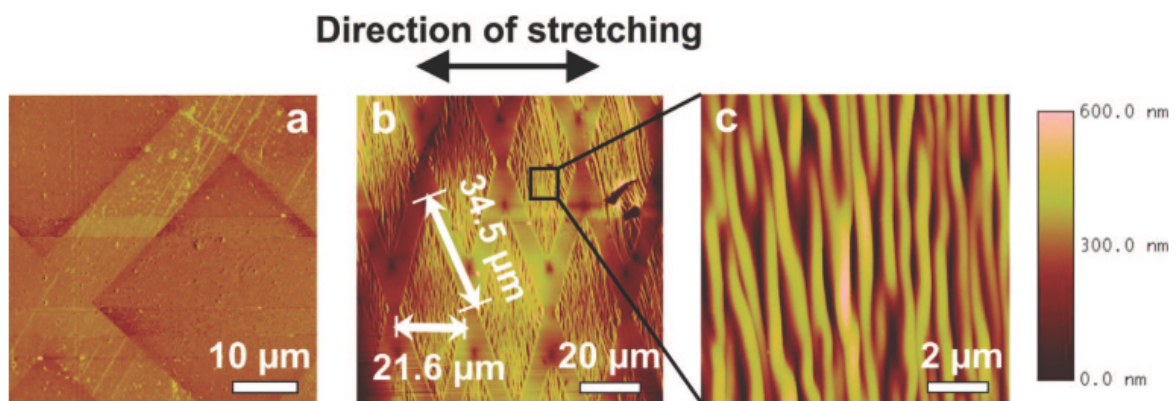


Figure 60. SFM images of a 200% stretched PS substrate after irradiation with a Xe^+ fluence of 10^{13} ions cm^{-2} : (a) phase contrast image and (b) change in the irradiated areas from square- to rhombic-shaped after annealing the substrates at 110°C for 1 h in vacuum and (c) enlarged image of the scan of the rippled area.

In our experiments, the original lengths are those after annealing (i.e., after relaxation of the substrate (rhombic shape)). Thus, $w_0 = 65\mu\text{m}$ and $l_0 = 21.6\mu\text{m}$. Because the surface is topologically structured in the direction of l_0 , the true length $l_{0,c}$, following the amplitude of the ripples is 23.7 μm . In the stretched case, the corresponding lengths are $w = l = \sqrt{2} \cdot 32.0\mu\text{m} = 45.3\mu\text{m}$ owing to the quadratic shape. Thus, the Poisson ratio of the Xe^+ -irradiated area is $\nu_s = \frac{45.3\mu\text{m} - 65.0\mu\text{m}}{45.3\mu\text{m} - 23.7\mu\text{m}} \times \frac{23.7\mu\text{m}}{65.0\mu\text{m}} = 0.333 \pm 0.05$. The same analysis was performed for the dimensions of the whole PS substrate to get the bulk value ν_b of nonirradiated PS. From stretching four different PS substrates to a length of 200%, we obtained an average Poisson ratio of 0.309 ± 0.030 . Within the limits of confidence, both values are comparable to 0.334 for bulk PS and 0.38 for cross-linked PS at room temperature, respectively¹³⁵. The value for the irradiated area tends to be higher, which supports the fact that it is more rubberlike, as expected for cross-linked PS. Because the rippling

occurred during annealing close to the glass transition of PS, where Poisson's ratio is 0.5, we take this value for the later analysis based on equation 1) for both, ν_s and ν_b ¹³⁶.

Principle of Rippling and Local Young Modulus

Rippling as observed within the rhombic areas is typical for a relaxed layered polymer system. Because rippling occurs only in the irradiated areas, it is proof for a chemically modified PS surface layer. However, the order of the ripple orientation is less pronounced than for the perfectly parallel ripples described in the cited literature. This result can be attributed to the high stretching ratio in our samples. Equation 1) offers the possibility to calculate the Young modulus of the ion beam induced skin layer from the ripple periodicity, the thickness of the skin layer, and the bulk materials' Poisson ratio. Because rippling was induced at the glass-transition temperature of bulk PS, the calculated Young modulus refers to this temperature. The ripple periodicity was measured directly from averaged height profiles across the SFM images at room temperature. The change in the ripple periodicity owing to cooling from the glass temperature to room temperature is $\sim 0.6\%$ for a linear expansion coefficient of $7 \times 10^{-5} \text{ K}^{-1}$ at 20 °C and thus negligible. To determine the thickness of the skin layer h , we also performed simulations of the interaction of the ion projectile with the PS¹³². In this way, we obtain a layer thickness h of $\sim 66 \text{ nm}$ for the exposure to Xe^+ . With a ripple distance of $0.9 \mu\text{m}$ and Poisson's ratios ν_s and ν_b of 0.5 for the modified areas and bulk PS, respectively, this leads to a calculated Young modulus of $E_s = 30E_b$ in the rippled areas. The significant increase of Young's modulus in the irradiated areas with respect to that of bulk PS indicates that the surface becomes locally stiffer. Furthermore, it again confirms a cross-linking in the surface¹³⁷. To estimate an absolute value for E_s , E_b has to be taken at the actual temperature of rippling (i.e., at 383 K). This temperature is above the glass transition of PS, where Young's modulus sharply decreases owing to the full segmental mobility of the polymer chains. At temperatures above the glass transition, an elastic regime, the so-called rubber plateau, occurs, which is characterized by a dynamic shear modulus G_N . It offers the possibility to calculate E_b at the rippling temperature according to $E_b = 2G_N(1 + \nu_b)$ ¹³⁶. With $\nu_b = 0.5$ and $G_N = 16 \text{ MPa}$, we obtain $E_b = 0.48 \text{ MPa}$ and $E_s = 14.5 \text{ MPa}$. This value provides $E_s/3 = G_N = 4.8 \text{ MPa}$ for the irradiated PS parts in agreement with 2.6 MPa for chemically cross-linked PS¹³⁸.

Summary

We locally cross-linked surfaces of stretched polystyrene (PS) by irradiation with ions of different mass (He^+ , Ar^+ , and Xe^+) using a mask with square openings. As determined from Monte Carlo simulations¹³², the thickness of the ion-beam-modified layer decreases with the mass of the ion and is between $\sim 60 \text{ nm}$ and $\sim 1 \mu\text{m}$. By annealing the irradiated PS substrate above the glass temperature, rippling within the irradiated areas occurred. Analysis of the rippling distance revealed

that the irradiated areas in PS behave elastically during contraction. The mechanical properties of the modified surface layer can reasonably be characterized by a constant Young modulus, even though the modification of the PS surface layer is not uniform throughout its depth. The modulus increases with the ion fluence and the mass of the ion to hundreds of MPa at 110 °C. Cross-linking was directly proven via the insolubility of a 100-nm- thick skin layer in toluene after irradiation with argon ions. This thickness was confirmed by the Monte Carlo simulations showing their validity for our quantitative analysis. Our results suggest that the superficial elastic properties of polymers can locally be tuned via cross-linking by irradiation with ions over a range of at least two orders of magnitude for Young's modulus. Depending on the ions' mass and/or the ion fluence, different local variations of desired Young's moduli can be fabricated in this way.

7.2 Micromechanical Cantilever Sensors as a Tool to Characterize Polymer Films

In the previous chapters I demonstrated that the mechanical properties of polymeric materials can be determined by DMTA for bulk samples or by the analysis of ripples in thin films. However, for a screening of the above mentioned parameters with DMTA, one would need large amount of substance.

We have shown that the wrinkling method is a straightforward way for the determination of the mechanical properties of thin polymeric films. This method relies on the differing mechanical behavior of the substrate and the probed film, which is required to form wrinkles. In the above presented study we modified a thin layer of a polymeric substrate to introduce this difference in mechanical behavior by ion-irradiation. However, when different compositions of composite materials are to be tested, the wrinkling method seems not to be applicable. The composites have to be coated or transferred to flexible substrates (e.g. PDMS) which often involve solvents. The solvents might change the properties of the substrate due to swelling or dissolution which is not feasible. However, wrinkling might also work on a substrate like silicon which is resistant to solvents. We could think of a silicon cantilever which is bended instead of a stretched substrate (Figure 61).

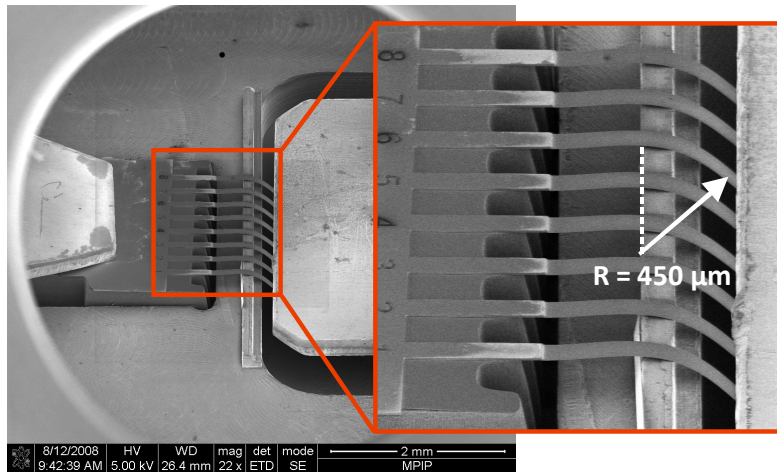


Figure 61. A banded cantilever as a possible platform for wrinkling experiments. The bending radius in this case was 450 μm.

We can calculate the critical strain^{117, 139} at which rippling would occur on a silicon cantilever when it is coated with a polymer.

$$\varepsilon_c = \frac{1}{4} \left(\frac{3E_b(1 - \nu_s^2)}{E_s(1 - \nu_b^2)} \right)^{2/3} \quad (7.2)$$

From equation (7.2) we can see that the critical strain is a function of elastic moduli ratio. By inserting the values for silicon as a substrate ($E_b = 170 \text{ GPa}, \nu_b = 0.23$) and a typical polymer ($E_s = 5 \text{ GPa}, \nu_s = 0.4$), equation (7.2) leads to a critical strain of approximately 500 %. Such a high value is a result of the high elastic modulus of the silicon compared to the modulus of the polymer. For a cantilever with a bending radius of 450 μm and a thickness of 5 μm (Figure 61) we calculate a maximum strain at the upper surface of the lever of about 0.55 %. From these values we can conclude that a banded cantilever can not be used for a wrinkling experiment. However, there is another approach which utilizes a resonating cantilever to characterize the mechanical properties of a thin film which I will introduce in the following.

Resonating Micromechanical Cantilevers

Here I want to introduce the concept of micromechanical cantilever sensors (MCS) as a tool to screen properties of polymeric materials. In this chapter I will discuss the role of film parameters like density, elastic modulus and film thickness on the frequency response of the cantilevers. To achieve reproducible results the homogeneity of the film is a crucial parameter. I show that upon surface modification of MCS with polymer brushes, Inkjet printed polymers formed homogenous films. We will use the knowledge about the interaction of brushes and matrix polymers with certain molecular weight (chapter 5 and 7) to promote the formation of homogeneous films on MCS.

In addition I performed finite element analysis of uncoated and coated cantilevers to identify critical parameters of the coating process. Subsequently, I describe how these surface-modified MCS, which were coated with polymers via Inkjet printing, can be utilized to determine the mechanical properties of the coating by measuring the resonance frequency of the MCS. A analytical approach was applied to compare the measured resonance frequency of the coated MCS with theoretical values.

7.2.1 State of the art of thin film characterization using MCS

Microcantilever sensors were initially designed and fabricated as force sensors with extremely high force sensitivity in the piconewton range, which allowed the measurement of forces between surfaces by atomic force microscopy. The availability of cheap and mass-produced microcantilevers triggered applications other than force sensing, where the microcantilevers act as physical chemical and biological sensors¹⁴⁰. The general sensing principle lies in the translation of a chemical or physical process of a coating into a mechanical response of the cantilever. To detect such a mechanical response, the MCS can be operated in two different modes. (i) The static mode, where the cantilever deflection Δz is monitored and (ii) the dynamic mode, where the cantilever resonance frequency f is monitored¹⁴¹ (Figure 62).

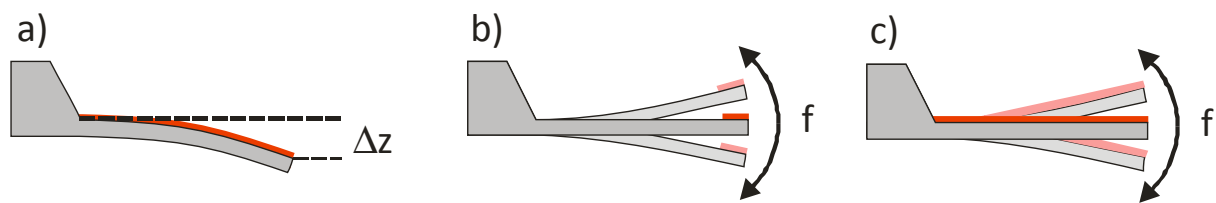


Figure 62. Operation modes of a coated micromechanical cantilever sensor. a) Static mode with asymmetric coating (red film) and b) dynamic mode with end-attached mass (red block). c) The third schematic represents a combined version of dynamic mode with asymmetric coating of the whole cantilever.

The static mode is based on changes of the surface stress σ of the cantilever surface. The stress can be caused by e.g. attached molecules, evaporated metal films or applied polymer films on one side of the cantilever. As a consequence of this surface stress, the cantilever bends downwards or upwards which corresponds to a negative or positive deflection Δz (Figure 62a). The deflection is related to the surface stress described by Stoney's formula¹⁴²

$$\Delta z = \frac{3\sigma(1-\nu)}{E} \left(\frac{L}{h}\right)^2 \quad (7.3)$$

Herein ν is the Poisson's ratio and E the Young's modulus of the cantilever. L and h are the cantilever length and thickness respectively. Using a modified version of Stoney's equation, Zhao et al.¹⁴³ were able to separate the contributions of thermal expansion and surface energy to the response of polystyrene coated microcantilevers.

The dynamic mode is typically used for high resolution mass sensing. In such an experiment the mass is located at the end of the cantilever (Figure 62b) and the frequency shift due to the attached mass is monitored. The mass change can then be calculated by

$$\Delta m = \frac{k}{4\pi^2} \left(\frac{1}{f_{load}^2} - \frac{1}{f_1^2} \right) \quad (7.4)$$

where k is the spring constant and f_1 the fundamental resonance frequency of the bare silicon cantilever. f_{load} is the resonance frequency of the loaded cantilever¹⁴⁴. By accurate calibration of the cantilevers and consideration of a correction term which accounts for the exact position of the added mass, sensitivities of subattogram were achieved¹⁴⁵. When the cantilever is uniformly coated (Figure 62c) equation (7.4) changes to

$$\Delta m = \frac{k}{4n\pi^2} \left(\frac{1}{f_{load}^2} - \frac{1}{f_1^2} \right) \quad (7.5)$$

where $n = 0.2427$ for the first resonance mode and accounts for the effective mass of the cantilever $m^* = n \cdot m_C$.

In the past years many publications about material characterization using MCS were focused on thin metal films¹⁴⁶⁻¹⁴⁸. Since the deposition techniques like evaporation or sputtering were highly improved in the last decade, the deposition of thin metal films with exceptional purity and roughness became possible. Furthermore, with focused ion beam and silicon micromachining techniques, the fabrication of sophisticated microstructures became possible. Kieswetter et al.¹⁴⁹ reported about the determination Young's modulus of Si_xN_y thin films prepared as microcantilevers using standard silicon micromachining techniques. They fabricated 0.54 μm thick cantilevers with lengths ranging from 200 to 800 μm and measured a Young's modulus of about 99 GPa with an error of 11 % using the resonance method. Haque et al.¹⁵⁰ developed a micrometer scale tensile testing setup and were able to investigate free-standing Al films of 200 nm thickness. They performed in-situ tensile testing in a scanning electron microscope and a transmission electron microscope and recorded stress strain curves. They found an elastic modulus of about 74.6 GPa which is close to the bulk modulus of Aluminum. However, both techniques are only applicable for materials which can be fabricated by standard silicon micromachining techniques.

As mentioned before, micromechanical cantilever sensors offer a very sensitive platform to detect changes in properties of a coated layer or an attached mass. One of the key issues of MCS used as sensors for changes of thin film properties (elastic modulus, swelling, thermal expansion, mass uptake) is the coating process and the quality of the resulting thin film. Bietsch et al.¹⁵¹ used Inkjet printing to functionalize cantilever array sensors. By coating the cantilevers with various sensor layers they were able to fabricate a chemical gas sensor to distinguish vapors of water and ethanol (Figure 63). Bietsch et al. could show that deposition of polymeric materials on cantilevers via Inkjet printing is in principle possible. However, the film quality plays a crucial role when it is the task to develop a device for quantitative sensing. The thickness of the film should be constant along the cantilever axis and the film should cover the whole cantilever homogeneously which is obviously not the case in their experiments (Figure 63).

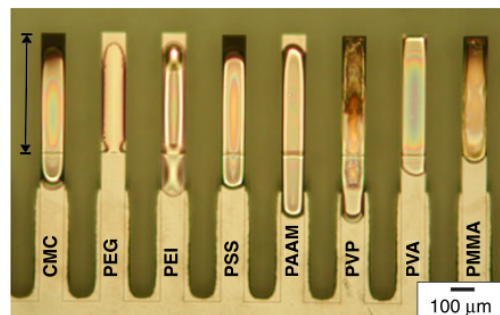


Figure 63. Optical micrograph of cantilevers coated with different polymers by inkjet printing of dilute solutions. Unmodified figure taken from¹⁵¹.

Furthermore, in their experiments the cantilevers were coated with titanium (1 nm) and gold (20 nm) before deposition of the polymers. Titanium has a high elastic modulus (122 GPa) and a moderate density (4.507 g/cm^3)¹⁵² compared to a gold film which has an elastic modulus of 80 GPa (factor 1.5 lower than Ti) but a density of 19.32 g/cm^3 (factor 4 higher)¹⁵³. A calculation of the mechanical response of such a multilayered system is difficult. Thus, a simple double layered system would be desirable.

7.2.2 Critical parameters for polymeric films

Film thickness and density

When MCS are used for the quantification of film properties, the thickness of an applied film becomes an important parameter. In a more general way, it is the ratio of cantilever thickness h_1 to film thickness h_2 that determines the frequency response of a vibrating coated cantilever. To calculate the elastic modulus of a polymer from the resonance frequency of a cantilever, it would be straight forward to fabricate a cantilever from the polymer directly ($h_1/h_2 = 0$). In this case equation (3.22) can be applied to calculate the elastic modulus of the polymer. Ransley et al.¹⁵⁴

reported a non-vacuum fabrication process to produce arrays of SU8 cantilevers and demonstrate their application as chemical sensors. SU8 is an epoxy-based, negative photoresist which is commonly used in micro lithography and therefore it is well characterized. Recently, Keller et al.¹⁵⁵ reported an optimized process to fabricate SU8 cantilevers with an initial bending below 20 μm and high spring constants. Other materials like TOPAS¹⁵⁶ and PDMS¹⁵⁷ were also reported as starting materials to fabricate micro cantilevers. As mentioned before, not all materials can be processed with lithographic methods to fabricate cantilever structures and furthermore this method is not suitable for a screening.

Standard silicon cantilevers can act as a support on which the material of interest can be deposited. Typically the elastic modulus of polymers is one order of magnitude lower than the elastic modulus of silicon ($E = 170 \text{ GPa}$ ¹⁵⁸ and $2\text{-}5 \text{ GPa}$ ¹⁵⁴⁻¹⁵⁶ for SU8 and TOPAS). In order to calculate the shift of the resonance frequency as a function of the film thickness we assume the following model system. A silicon cantilever with a length of $750 \mu\text{m}$, a width of $90 \mu\text{m}$ and a thickness of $h_1 = 5 \mu\text{m}$ having an elastic modulus of 170 GPa is coated with a polymer having an elastic modulus of 3.5 GPa and a titanium film with an elastic modulus of 122 GPa . We calculated the resulting frequency f according to equation (3.23) which attributes to both, the density and the rigidity of the film. The resonance frequency of the uncoated cantilever is $f_0 = 12248 \text{ Hz}$. The density of the film is directly proportional to the mass which is added to the cantilever and the rigidity reflects the elastic modulus of the film material. Consequently we can calculate the effect on the resonance frequency which is caused by the added mass only by using equation (7.5). Since the polymer has relatively low elastic modulus (3.5 GPa) compared to the silicon cantilever (170 GPa) the relative frequency shift of the coated cantilever is mainly driven by the added mass as can be seen from the same trend of the red and black curve in Figure 64a. When the frequency shift calculated from equation (3.23) is corrected by the mass effect (equation (7.5)) we obtain the effect of the rigidity only. If we consider all experimental errors and the sensitivity of the setup we might say that a frequency shift of 20 Hz is measurable with a sufficient small error. To achieve this shift the effect of the rigidity for the above defined polymer film, a film thickness of $h_2 \geq 280 \text{ nm}$ would be necessary ($h_1/h_2 = 18$).

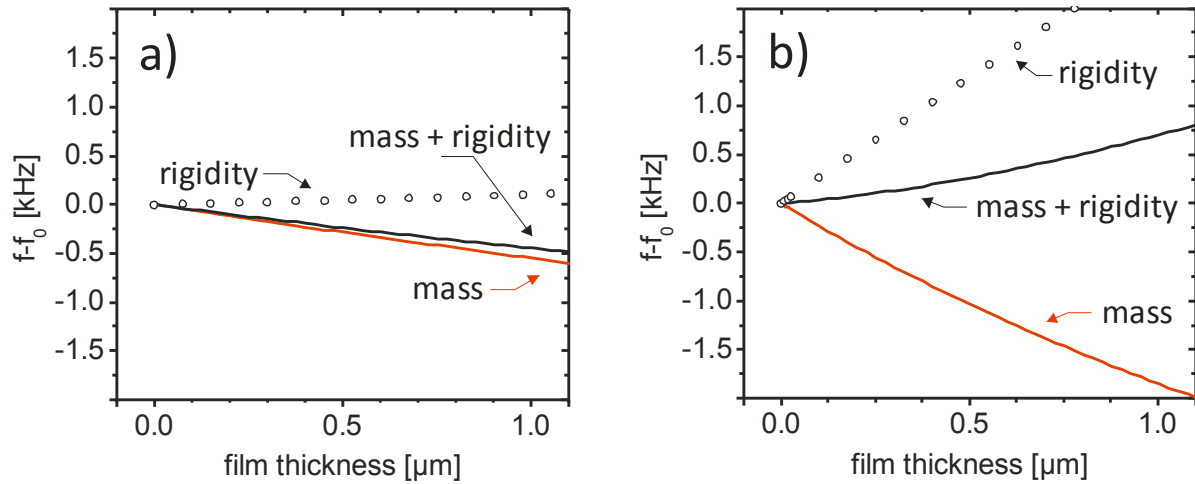


Figure 64. Resonance frequency of a 750 μm long, 90 μm wide and 5 μm thick cantilever as a function of the polymer film thickness. Effect of mass, rigidity + mass and rigidity only are plotted for a) a polymer film and b) a titanium film. The resonance frequency of the bare cantilever is $f_0 = 12248$ Hz.

In contrast, when we calculate the same curves for a titanium film with an elastic modulus (122 GPa)¹⁵² which is comparable to the elastic modulus of the silicon, a 20 Hz shift is already achieved at a film thickness of 8 nm, i.e. $h_1/h_2 = 625$ (Figure 64b). The mass effect is much stronger for the titanium than for the polymer, which is a consequence of the higher density of titanium (4.5 g/cm³)¹⁵² than of our model polymer (1.1 g/cm³). These findings lead us to important conclusions for the investigation of mechanical properties polymer films coated on silicon cantilevers.

1. To measure a change in resonance frequency of 20 Hz due to the effect of elastic modulus (rigidity) of a polymer film which is coated on a silicon cantilever, the polymer film has to be sufficiently thick, i.e. $h_1/h_2 = \text{small}$.
2. The higher the elastic modulus and the lower the density of the film, the bigger is the change in resonance frequency due to changes of the elastic modulus of the film.

Another important parameter for the coating process of MCS with polymers is the film quality in terms of homogeneity. How this parameter is controlled and how homogeneity can be tailored, I will describe in the next section.

7.2.3 Surface initiated polymerization on silicon cantilevers

When cantilevers are used in the dynamic mode to characterize mechanical properties of the coated thin film, the quality of the film becomes important. To calculate the resonance frequency of a coated cantilever analytically by equations (3.22), (3.23) and (7.5), the shape of the film has to be describable mathematically in terms of Euclidean geometry. The ideal and most simple case is a rectangular geometry of both, the cantilever and the film (Figure 65).

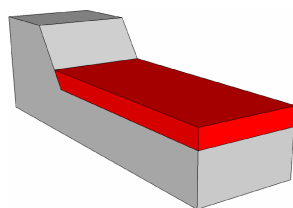


Figure 65. The ideal geometry of a double layer system like a coated cantilever. Both, the cantilever and the film have a perfect rectangular shape which can be described by Euclidian geometry.

When the film is inhomogeneous or the polymer dewets the cantilever (Figure 66a, d), the characterization of the film becomes impossible. Therefore we applied the same concept of grafting polymer brushes via ATRP which we used for the modification of μ gels particles described earlier. In this way the surface energy difference between the silicon surface of the cantilever and the polymer is lowered. The immobilization of the primary ATRP-initiator was carried out in a modified Schlenk setup consisting of a Schlenk tube with a special holder for the MCS. The Schlenk tube was connected to a Schlenk flask which contained the reaction solution¹⁵⁹. Using this modified setup it was possible to graft PEMA brushes from the silicon surface of the MCS (Figure 66b)⁷⁰. With these surface modified MCS it is possible to deposit a homogeneous polymer film at the cantilever surface via Inkjet printing (Figure 66c, e).

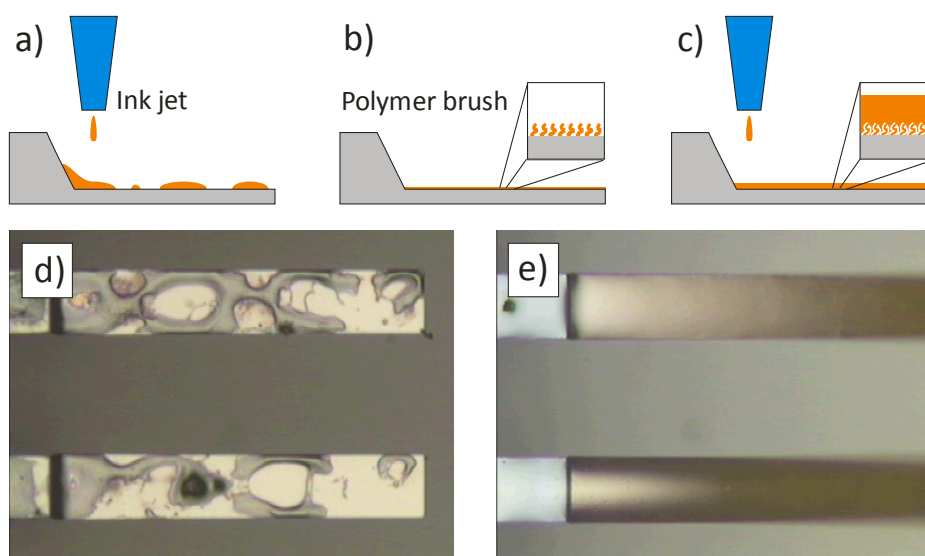


Figure 66. a) Inkjet printing of a polymer solution on a non modified cantilever leads to dewetting. b) Grafting of polymer brushes leads to a covalently bond “interfacial” layer. c) The grafted polymer brushes suppress dewetting and enable deposition of homogeneous polymer films. d) On unmodified cantilevers the PEMA dewets the surface. e) On modified cantilevers, Inkjet printing of homogeneous films became possible.

To check the influence of grafted polymer brushes on the wetting behavior of printed PEMA we prepared two microcantilever arrays with a length of the levers $L = 750 \mu\text{m}$. On the first array we grafted a layer of polymer brushes with a thickness of $25 \pm 1 \text{ nm}$ measured with Ellipsometry. The second array was left blank and was used without further treatment. According to Kim et al.¹⁶⁰ we calculated a molecular weight $N (M_w)$ of the grafted brushes as

$$M_w = \frac{\rho \cdot t_B}{\Gamma} \cdot Na \cdot PDI \quad (7.6)$$

where ρ is the mass density of the PEMA, t_B is the thickness of the brush layer, Γ is the grafting density and Na is the Avogadro's constant ($6.0221 \times 10^{23} \text{ mol}^{-1}$).

$$M_w = \frac{1.119 \frac{\text{kg}}{\text{m}^3} \cdot 25 \cdot 10^{-9} \text{m}}{0.2 \cdot (10^{-9} \cdot \text{m})^{-2}} \cdot 6.022 \cdot 10^{23} \cdot \text{mol}^{-1} \cdot 1.15 = 97 \text{ kg/mol}$$

Since we know that complete wetting of a flat substrate occurs when¹ $N/P > 1$ we therefore chose a homopolymer P with low M_w to print on the grafted cantilevers. The printing was performed with a solution of PEMA homopolymer with M_w of 14600 g/mol ($N/P = 6.6$). We prepared a solution of 10 mg/mL in toluene which was then printed on the MCS using the Nano-Plotter as follows. A printing pattern was designed consisting of 13 drops along the axis of the lever with a spacing of 70 μm between the drops. The small spacing allowed the drops to merge easily. The drops were ejected with a voltage of 75 V and a pulse time of 50 μs at a distance between nozzle and lever of 0.5 mm. After the printing process an optical photograph of the two arrays was taken with the camera of the Nano-Plotter (Figure 66). On the unmodified cantilevers the printed PEMA dewetted from the surface during the evaporation of the toluene (Figure 66d). The dewetting led to an inhomogeneous film which can not be used for any sensing applications or for material characterization. In contrast, the cantilevers which were modified with polymer brushes permitted the deposition of a homogeneous, smooth film which covered the whole cantilever (Figure 66e).

The thickness of the PEMA film was then measured by SEM to be 1.01 μm . We found the thickness of the film to be constant along the cantilever axis with deviations less the 0.05 μm . According to equation (3.23) we calculated a resonance frequency for the coated cantilever of 12605 Hz for the first resonance mode by using the parameters given in Table 6. For silicon we assumed an elastic modulus of 170 GPa and a density of 2.33 g/cm^3 . For PEMA we deduced the elastic modulus (1.42 GPa) from the DMTA measurement in (Figure 36). The density was 1.119 g/cm^3 . The measured resonance frequency was 12628 Hz. Furthermore, we performed a finite element analysis (Figure 67) of the uncoated and the coated cantilever with ANSYS to compare theoretical and experimental data.

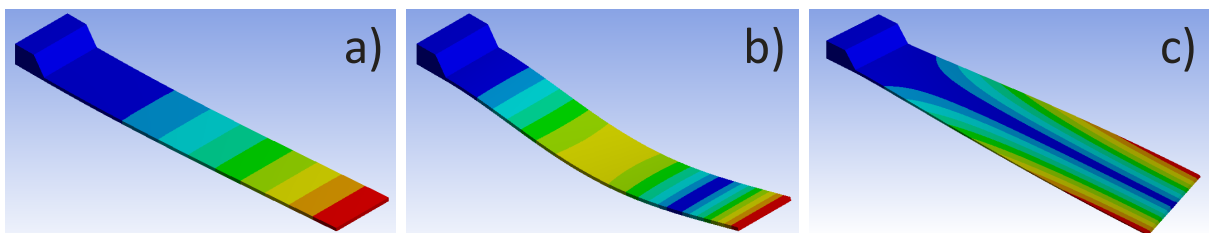


Figure 67. Simulated mode shapes for a cantilever with dimensions given in Table 6.

The first three vibration modes were simulated and showed the expected shape for flexural and torsional vibration (Figure 67a-c). Moreover, the simulated resonance frequencies were close to the experimental and calculated frequencies (Table 6)

Table 6. Parameters for the brush coated cantilever with an Inkjet printed PEMA film. f_0 denotes the resonance frequency of the uncoated cantilever. f_1 and f_2 denote the first and the second resonance mode of the coated cantilever respectively.

Cantilever	L [μm]	w [μm]	h_1 [μm]
	750	90	5.355
Polymer film	ρ [g/cm^3]	E [GPa]	h_2 [μm]
	1.119	1.42	1.01
	f_0 [Hz]	f_1 [Hz]	f_2 [Hz]
Experiment	13137	12628	79570
Equation (3.23)	13134	12605	78997
ANSYS	13060	12554	78618

From the results in Table 6 we can see that the measured resonance frequency is 23 Hz higher as the calculated resonance frequency for the first resonance mode and 735 Hz higher for the second resonance mode. A possible reason for this discrepancy is the frequency dependence of the elastic modulus of polymers. This dependency can be seen in all the DMTA measurements shown in the previous chapters. Within more than ten decades in the frequency window, the elastic modulus varies about seven decades. The resonance frequency which was calculated by using equation (3.23) was based on an elastic modulus of 1.42 GPa, deduced from a DMTA measurement. However, by rearranging equation (3.23) and inserting the measured resonance frequencies we can calculate the elastic modulus of the PEMA film for the first and the second resonance mode. By doing so, we derived an elastic modulus of 2.20 GPa at 12628 Hz and 4.53 GPa at 79570 Hz.

7.2.4 Mechanical spectroscopy with cantilevers

The relation between frequency and elastic modulus could be used to perform a mechanical spectroscopy experiment like DMTA with a polymer coated cantilever. In particular it would offer the possibility to screen the mechanical properties of a sample if only a small amount of substance is available. To verify the applicability of polymer coated cantilevers as sensor platforms for mechanical spectroscopy we can utilize the frequency-temperature equivalence principle⁴⁴. In a typical DMTA measurement this is either done by sweeping the frequency at a given temperature of the sample to construct a mastercurve or by sweeping the temperature at a fixed frequency to deduce the modulus-temperature relation. For an experiment with a cantilever the second way seems to be more applicable because the temperature of the specimen can be varied easily while the frequency steps are limited to the resonance modes of the lever.

To check if the results of a cantilever experiment can be compared to the results of a typical DMTA measurement we need to know the relation between elastic modulus and temperature at the frequency of the cantilever. This relation can be deduced from a master curve by using the WLF equation. In a rearranged form (equation (3.9)) it states that the viscoelastic behavior at one frequency (ω_{ref}) can be related to that at another frequency (ω) by a change in the temperature scale only.

$$T = T_{ref} - \frac{C_2}{1 + \frac{C_1}{\log\left(\frac{\omega}{\omega_{ref}}\right)}}$$

Since we know G' and G'' at ω for a given reference temperature from the mastercurve and C_1 and C_2 from the shift factors, we can transform the master curve to a temperature dependent expression. To check if this transformation is valid we first measured the dynamic response of a PEMA homopolymer with $M_w=15k$ (Table 3) at a frequency of 10 rad/s for temperatures between 50 and 140 °C with a heating rate of 2K/min (Figure 68a). Subsequently we transformed a mastercurve that we have already measured before (Figure 37a) by using equation (3.9) to get the dynamic response with respect to the temperature (Figure 68b) at 10 rad/s.

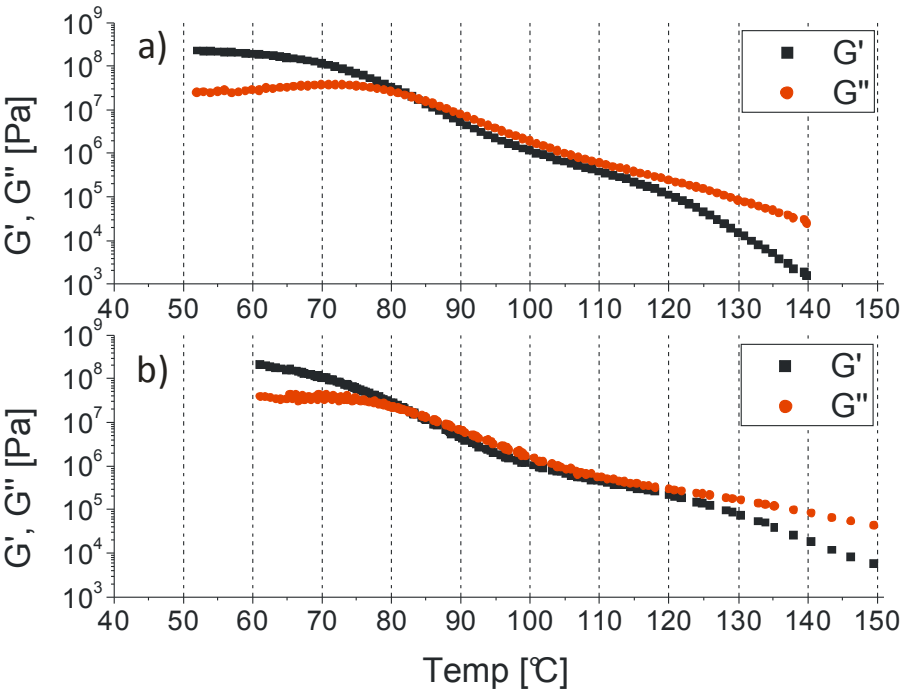


Figure 68. a) Temperature dependence of G' and G'' of PEMA homopolymer with $M_w=15k$. The heating rate was 2 K/min and the reference frequency $\omega_{ref} = 10$ rad/s. b) Transformed mastercurve at 10 rad/s.

From Figure 68 we can see a) that the transformation of a mastercurve to a temperature dependent response curve is valid in the temperature range from 60-120 °C. First, the curves of G' are showing the same progression between 60 and 120 °C. Beyond 120 °C the polymer is creeping already which

might lead to the differences between the measured and the transformed curve. Second, the curves for G'' are also showing the same progression between 60 and 120 °C. From the measured G'' (Figure 68a) we can deduce the glass transition point at the maximum of the G'' curve¹⁶¹ as $T_g(G''_{max}) = 72\text{ °C}$ which is in good agreement with the glass transition we measured via DSC $T_g = 68\text{ °C}$ (Table 3). The glass transition which we deduced from the transformed curve is $T_g(G''_{max}) = 70\text{ °C}$ (Figure 68b). The conformity of the curves for G' and G'' and the agreement of the glass transitions for the measured and the transformed curves shows that the WLF equation can be used to transform a mastercurve to a temperature dependent dynamic response curve for a given frequency, e.g. the resonance frequency of a cantilever.

Temperature sweep with polymer-coated cantilevers

A 750 μm long and 1.23 μm thick cantilever was covered with polymer brushes as described earlier. Then a solution of PEMA with $M_w = 15\text{k}$ was printed via the Inkjet printer and a homogeneous film was formed. The thickness was measured with ellipsometry to 260 nm which results in $h_1/h_2 = 5$. We chose a thin cantilever and a thin polymer film, to ensure homogeneous temperature field over the whole cantilever while heating it up. The cantilever was mounted on a piezo driven cantilever holder for vibration excitation. The polymer covered face of the cantilever was adjusted $\sim 2\ \mu\text{m}$ above a heating stage and the resonance frequency was read out via a laser which was reflected on the backside of the lever. The temperature was increased stepwise from 20 to 250 $^\circ\text{C}$. After holding each temperature for 10 minutes, a frequency spectrum was recorded. The maximum of the resonance peak was chosen as the resonance frequency and the full width half maximum (FWHM) was deduced from the shape of the peak. The frequency curve was corrected by the contribution of the silicon due to heating (0.3 Hz/ $^\circ\text{C}$) which was measured with a blank silicon cantilever of the same size.

The temperature dependent dynamic response curve for PEMA at a frequency of 3.2 kHz is shown in Figure 69a (filled squares). By comparing the storage modulus at 3.2 kHz with the storage modulus at 1.6 Hz (10 rad/s) in Figure 68 we can see that the curve is shifted to higher temperatures while the shape of the curve remains similar. The viscous part of a DMTA measurement is described by the loss modulus G'' (Figure 69a, open squares). From the G'' -curve we deduced a $T_g(G''_{max}) = 80\ ^\circ\text{C}$, which is 12 $^\circ\text{C}$ higher than the same curve at 1.6 Hz (Figure 68a).

The temperature dependent dynamic response of a PEMA-coated cantilever can be divided into two parts. (i) The resonance frequency of the cantilever as a function of temperature (Figure 69b). (ii) The full width half maximum (FWHM) of the resonance peak as a function of temperature (Figure 69c). While the resonance curve is mainly correlated to the storage modulus of the coating, the FWHM curve can be correlated with the loss modulus because it reflects the damping of the vibration.

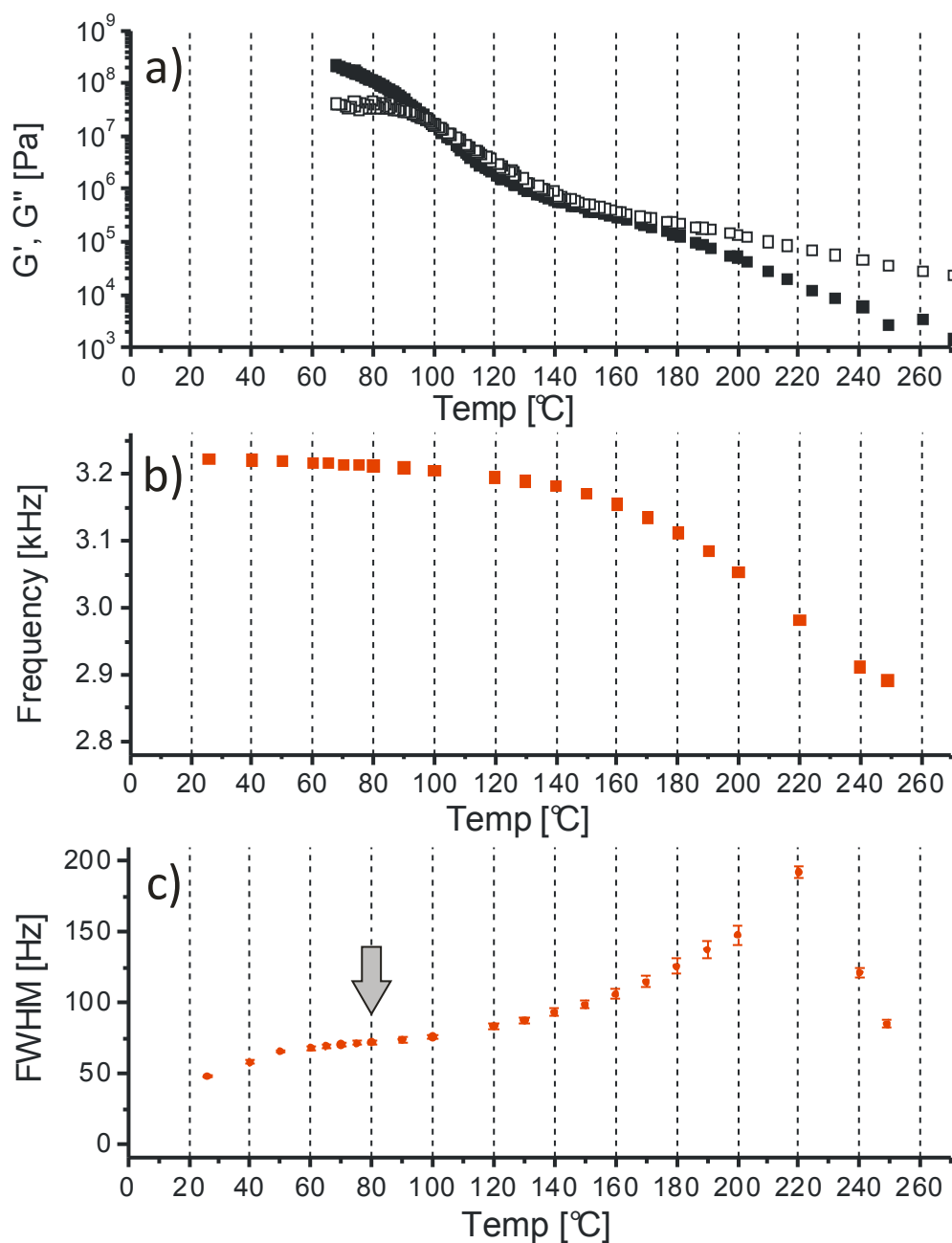


Figure 69. a) Temperature dependent storage modulus curve which was created by transforming the corresponding master curve to a frequency of 3.2 kHz. b) Measured resonance frequency of a PEMA-coated cantilever. The frequency was corrected by the contribution of the silicon (0.3 Hz/°C) due to heating. c) Measured FWHM of the resonance peak for the PEMA-coated cantilever.

In the resonance frequency curve (Figure 69b) we can see that the frequency decreases from 3.22 kHz to 3.21 kHz between 20 and 80 °C. This small decrease of only 10 Hz might be attributed to the softening of the PEMA with increased temperature. Starting from 80 °C the frequency decreases significantly faster with increasing temperature until it reaches a frequency of 2.89 kHz at 250 °C. Above the T_g of PEMA, the film is getting soft and it starts to flow leading to a decreased frequency. Based on equation (3.23), we calculated storage modulus for PEMA of 14 GPa at 20 °C and 1.4 GPa at 250 °C. Firstly, these values are much higher than the values obtained by DMTA (Figure 69a).

Secondly, they vary in a range of about one order of magnitude while the G' and G'' in the DMTA measurements varies about 5 orders of magnitude in the same temperature range.

The discrepancy between the DMTA and cantilever results might originate in two effects. (i) Due to the small thickness of the film, the mechanical contribution of the polymer between 20 and 80 °C is too small to lower the resonance frequency sufficiently. (ii) Around 80 °C the polymer undergoes the transition from one elastic state to another elastic state at higher temperatures. The viscous flow region is still not reached but viscous damping comes into play. Viscous flow starts between 160 and 180 °C as can be seen from the slope of the G' and G'' curve above this temperature. Since the resonance frequency curve describes only the elastic behavior of the coated PEMA, it would be therefore interesting to see also the viscous behavior with increasing temperature.

At $T_g(G''_{max}) = 80\text{ °C}$ which was deduced from the DMTA measurement we can observe a plateau in the FWHM (Figure 69c, grey arrow) where the FWHM does not change significantly between 60 and 100 °C. This plateau might be connected to glass transition as described above. At temperatures above 100 °C the FWHM is further increasing which implies that the polymer starts to flow. From the DMTA measurement (Figure 69a) we observed an onset of flow between 140 and 160 °C. The melting temperature of PEMA with $M_w = 15\text{ kg/mol}$ is around 160 °C¹⁶². Because the T_g is frequency dependent, the melting temperature should also depend on the frequency. In the FWHM curve (Figure 69c) we saw a drop of the FWHM between 240 and 250 °C which we assign to the melting of PEMA.

We have seen from the transformation of the mastercurve to different frequencies that the resulting curve of G' and G'' is shifted to higher temperatures. We have also seen that the frequency response and the damping of a coated cantilever depend on the temperature. It would therefore be desirable to check if this response can be reproduced by cantilevers with different frequencies. Furthermore, the use of thicker polymer films might enhance the sensitivity and increase the contribution of the polymer film to the resonance frequency.

Summary

The approach of surface initiated polymerization to lower the surface energy difference between silicon and polymer and the subsequent Inkjet printing of polymer solution leads to homogeneous polymer films when they are printed by Inkjet printing. The films had a sufficient thickness and homogeneity along the cantilever axis. The consistency of the analytical data, the FEM simulations and the experimental data shows that we were able to deduce the mechanical properties of an Inkjet

printed polymer film by measuring the resonance frequency of the coated cantilever. For a 1.01 μm thick PEMA film we derived an elastic modulus of 2.20 GPa at 12628 Hz and 4.53 GPa at 79570 Hz.

Furthermore micromechanical cantilever sensors have some advantages over typical methods to measure mechanical properties of polymers like DMTA.

- They are relatively cheap compared to setups needed for DMTA or SPM, since they can be manufactured as mass products with conventional silicon microfabrication technologies.
- Only a small amount of sample substance is needed since the size of typical MCS is in the range of a few 100 μm .
- The analyzing procedure is very fast since the response of MCS to changes of the applied sample is very fast.
- Furthermore, due to their geometry, MCS are highly sensitive sensor platforms for high throughput and multiplexed detection.

By transforming a mastercurve of PEMA to a temperature dependent modulus curve we could show that material parameters like the glass transition are shifting to higher temperatures when the frequency is increased. By shifting such a curve to the frequency of a PEMA-coated MCS we could show that the dynamic response of the coated MCS at different temperatures displays the mechanical properties of the coated film. Although a quantitative analysis of the elastic moduli with coated cantilevers resulted in values one order of magnitude higher than the values recorded by DMTA, the mechanical response of PEMA at different temperatures could be related to DMTA results.

7.3 Nanoparticle Monolayer Assembly on Silicon Cantilevers

Colloidal monolayers can be used to form highly ordered 2D crystals¹⁶³. To form such 2D crystals the nanoparticles are trapped at the air – water interface. By using a Langmuir-Blodgett trough, the nanoparticles can be pushed together to form a hexagonal close-packed monolayer, which can then be transferred onto a solid substrate. In this way a monolayer of polymeric colloids can be formed where the thickness of the monolayer is determined by the diameter of the colloids. Recently it has been shown that such monolayers can be transferred not only to large scale substrate but also to micromechanical cantilevers¹⁶⁴. By dry annealing or vapor annealing polymeric colloids can be fused together to prepare layers with different architecture ranging from spot bonded particles to continuous films (Figure 70). During the fusion of the colloids, the mechanical properties of the layer change. This change can be tracked the resonance frequency of the cantilever. During a dry annealing process, we expect that the mechanical properties of the layer will change due to two effects. (i) First, the Young's modulus of the colloids is decreasing and the layer becomes soft. This

effect will lead to a decrease in resonance frequency. (ii) At a certain temperature the colloids start to fuse together which increases the stiffness of the monolayer and leads to an increase in resonance frequency.

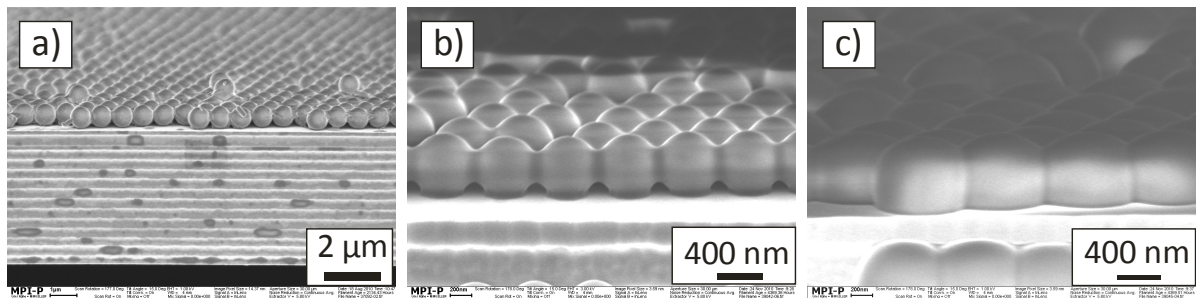


Figure 70. Monolayer of polystyrene colloids on a cantilever at different stages of the fusing process. a) Colloids before heating, b) during heating and c) at 180°C. Images by courtesy of Ting Liu.

When the cantilever is coated with a monolayer of spheres, a simple analytical expression for the resonance frequency for a solid film like equation (3.23) can not be applied anymore. Therefore we designed a finite element model consisting of a cantilever with the following dimensions. The cantilever had a length of $L = 50 \mu\text{m}$, a width of $w = 2.132 \mu\text{m}$ and a thickness $h_1 = 0.5 \mu\text{m}$. It was coated with n spheres with a diameter D in a hexagonal close-packed pattern (Figure 71a). The cantilever surface was turned hydrophobic by a chemical vapor deposition of a perfluorosilane before deposition of the colloids. This step was necessary for the transfer of the colloids from the floating monolayer to the cantilever¹⁶⁴. It has to be noticed that the fusing process could be modeled by simulating an overlap or bridging between the spheres like seen in Figure 70b. Such a model requires extensive design of the FEM model for every stage of the fusing process, i.e. increased overlap. To describe the principal change in resonance frequency of the cantilever during the fusing process without extensive model design we therefore chose flexible contact approach described in the following. As a boundary condition for the FEM model, the colloids must stay at their position, e.g. they are not allowed to separate from the cantilever. Otherwise the model would turn into a kinematic. Accordingly we chose a fixed contact between sphere and cantilever as a first boundary condition μ_{SC} (Figure 71b). This boundary condition mimics a physical connection of the sphere and the cantilever at the contact point. In other words, at the boundary of the two geometries (sphere and cantilever) they share one knot at the contact point. This connection allows no separation and transmits tensile- and compressive forces. For the contact point between two spheres we defined a variable boundary condition, μ_{SS} , which transmits compressive forces and allows sliding of the spheres. This condition is equivalent to friction between bodies, where the static friction coefficient μ between two solid surfaces is defined as the ratio of the tangential force required to produce sliding, divided by the normal force between the surfaces. By varying μ_{SS} we are able to mimic the

fusion process of the colloids where the physical connection between spheres becomes stronger with increasing temperature.

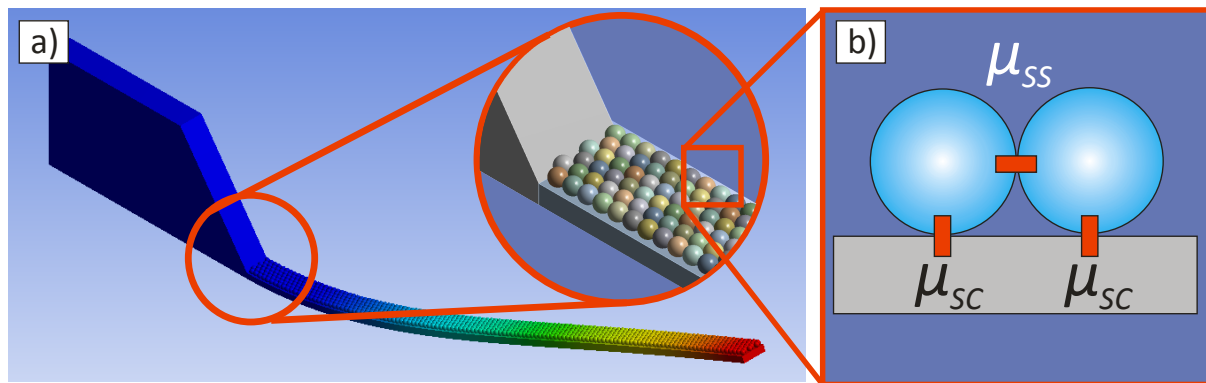


Figure 71. a) FEM model for the modal analysis of a cantilever coated with polymeric colloids. The colloids are arranged in a hexagonal close-packed pattern (inset). The image shows the calculated displacement for the first resonance mode of the cantilever. b) The spheres have different boundary conditions. μ_{SC} and μ_{SS} representing the interactions between sphere and cantilever and between spheres respectively.

Investigating the second stage of the fusing process, where the spheres start to fuse together, we increased μ_{SS} from 0 to 1.0 (Figure 72). At $\mu_{SS} = 0$ the spheres can slide frictionless whereas at $\mu_{SS} = 1.0$ the friction coefficient is two times the dry friction coefficient between two polystyrene surfaces¹⁶⁵. With increasing μ_{SS} from 0 to 0.6 we see a small increase in the resonance frequency of 0.04%. At a friction coefficient of 0.7 the interaction between the colloids becomes strong and the frequency shifts about 5% to higher frequencies. We assume that at $\mu_{SS} = 0.7$ the friction between spheres becomes so strong that the spheres basically do not slide anymore but start to deform. This assumption is supported by the fact that with further increase of μ_{SS} the frequency stays constant. When we set $\mu_{SS} = \mu_{SC}$ which reflects physical connection between sphere and cantilever, the frequency increases further to about 40%. At this point we have a different situation because now all colloids are physically connected representing a single body. We also have to take into account that the spheres were modeled with an elastic modulus of 3 GPa.

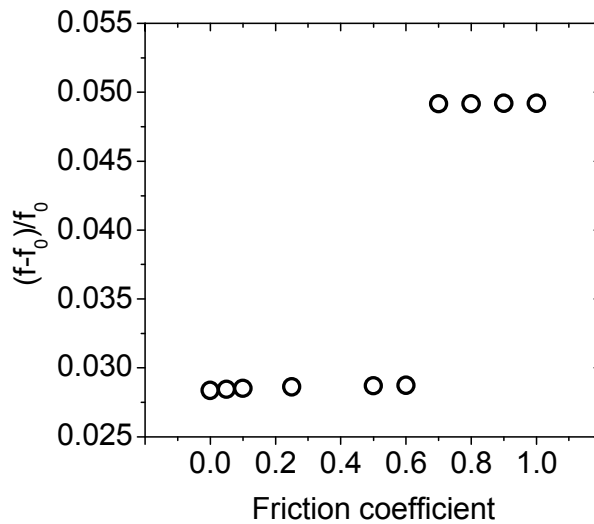


Figure 72. Relative resonance frequency shift of a 50 μm long, 2.1 μm wide and 0.5 μm thick cantilever with a resonance frequency of $f_0 = 275.581$ kHz. Relative resonance frequency shift of the cantilever coated with 750 polystyrene spheres with an elastic modulus of 3.0 GPa as a function of the friction coefficient between the spheres.

In the next simulation we varied the elastic modulus of the spheres imitating the first stage of the fusing process where the polymer becomes soft with increasing temperature. The results of a modal analysis are shown in Figure 73. The model consisted of a cantilever coated with 750 spheres. At high elastic modulus of the spheres the resonance frequency of the cantilever is increased, represented by a positive frequency shift.

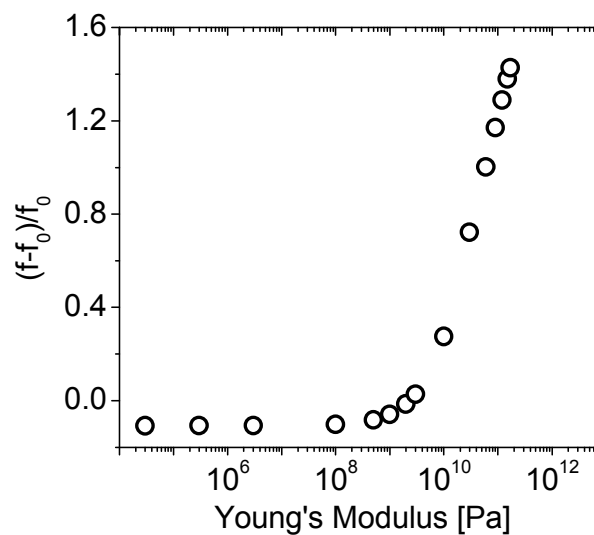


Figure 73. Relative resonance frequency shift of a 50 μm long, 2.1 μm wide and 0.5 μm thick cantilever with a resonance frequency of $f_0 = 275.581$ kHz. Relative resonance frequency shift of the cantilever coated with 750 polystyrene spheres as a function of the Young's modulus of the spheres.

Similar to the model system of a continuous titanium film which we developed before (Figure 64b), the rigidity of the spheres contributes to the average rigidity of the cantilever, causing a positive frequency shift. At moduli $E < 3$ GPa, the shift of the resonance frequency becomes negative. The

shift to lower frequencies is because for very low moduli of the coating, the mass effect becomes dominant. In this case we can see the similarity to the continuous polymer film in Figure 64a.

We will now connect the results of both simulations for spheres (Figure 72, Figure 73) and the analytical results we got from our model system for films in Figure 64. When we draw a principal trend of the resonance frequency for a cantilever which is coated with polystyrene spheres as a function of temperature, we can differentiate different behaviors of the colloidal monolayer and the continuous film (Figure 74). For low temperatures we have a certain resonance frequency of the cantilever coated with spheres (Figure 74a). As the temperature is increased, the frequency will decrease until a point (Figure 74b) is reached where the spheres start to fuse/merge. Upon further heating the frequency will increase due to the increased contact strength between spheres until the spheres have physical connection representing a single body (Figure 74c). The spheres are fused together and a continuous film has formed. Due to further heating the film becomes softer and thus the resonance frequency is decreased again until it reaches a minimum (Figure 74d). Upon cooling, the film becomes stiffer which leads to an increased resonance frequency until it reaches its maximum (Figure 74e). The final frequency of the film is higher than the frequency of the colloidal monolayer.

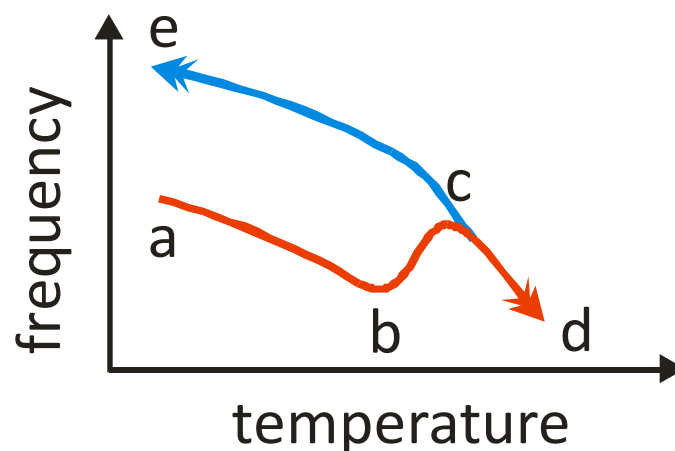
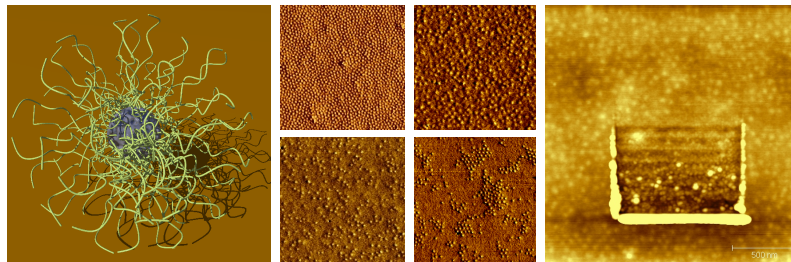


Figure 74. Principal trend of the resonance frequency for a cantilever coated with polymeric spheres as a function of the temperature.

Experimentally, this curve was already reproduced by Liu et al.¹⁶⁶. In order to study the film formation of colloidal polystyrene (PS) monolayers, non-crosslinked PS colloidal monolayers were coated on a microcantilever array. The temperature was increased from room temperature up to 210 °C and the resonance frequency of the cantilever was recorded.

8. Concluding Remarks and Outlook

Dispersion behavior and wear resistivity



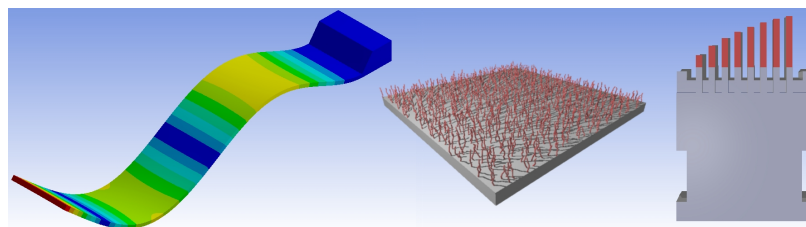
In my thesis I investigated the interaction of surface grafted polymer brushes with like homopolymers in materials such as composites composed of soft, polymer-grafted nanoparticles and homopolymers. I found that the properties of these composites are substantially influenced by the molecular weight ratio of polymer-brush and matrix polymer. The dispersion behavior and the resistivity to surface wear were associated with the wettability of the brush-coated nanoparticles. A transition from complete wetting to incomplete wetting of PEMA-g-nanoparticles was found at molecular weight ratios (N/P) between 0.3 and 0.5. For composites with $N/P > 0.5$ good dispersion and increased wear resistivity was observed while for $N/P < 0.3$ aggregation and no increase of the wear resistivity was observed. With the nanowear experiment described in this work I gained insight into surface nanowear effects in particular at a length scale of the nanoscopic filler particles, which was not reported so far for such composites. Furthermore, the analysis method allows the definition of a critical force for the quantitative comparison of nanoparticle-polymer systems of different composition. Subsequently, by dynamic mechanical thermal analysis I could show that the T_g and the elastic modulus of blends with $N/P > 1$ were preserved while the wear resistivity of these blends was improved.

Further analysis of the composites which were investigated in this work could contribute to a comprehensive understanding of the wetting mechanisms of polymer brushes. A direct measurement of the wettability of the PEMA-g-nanoparticles would be very interesting since it could confirm the theoretical results that were reported by Leibler et al.¹⁶⁷ and Gay¹⁶⁸ and the experimental results of Mass et al.¹. The results for flat substrates were further developed for curved substrates like spherical particles by Gast and Leibler^{169, 170}, Vincent and co-workers^{171, 172} and some other groups.

However, a direct measurement of the wettability in terms of contact angle between polymer-grafted nanoparticles and like polymer matrix has not been reported so far.

The presented nanowear experiment and the analysis of the data might also be useful for the analysis of self-healing polymers. Self-healing polymers have a structurally incorporated ability to repair damage caused by mechanical stress. Initiation and propagation of cracks as well as other types of damage on a microscopic level has been shown to change material properties like impact or tensile strength. These changes could lead to whole scale failure of the material¹⁷³. Typically, self-healing polymers have been analyzed by first inducing cracks or damage. The cracks or damage were induced by stretching the sample or by indenting/sliding the surface with spherical, conical or tetrahedral probes. After the mechanical treatment a sample analysis with SEM or TEM of the damaged area was performed¹⁷⁴⁻¹⁷⁶. This procedure has several disadvantages. The damage induced by a mechanical treatment with macroscopic indenters or sliders causes dramatic changes in the morphology of the probed material, i.e. macroscopic cracks. According to Wool and co-workers¹⁷⁷, the stages of self-healing are: (i) surface rearrangement, (ii) surface approach, (iii) wetting, (iv) diffusion, and (v) randomization, ensuring disappearance of cracking interface. By the investigation of the healing of such large material deformations via SEM, only the first two stages of the healing process can be investigated. To get an understanding of the wetting, diffusion and randomization stages, the application of the described nanowear experiment to such self-healing systems would be beneficial. First, the induced damage is much smaller and can be furthermore tuned by adjusting the normal applied force of the SPM tip. Due to the high resolution of the SPM it might be possible to investigate the diffusion and randomization of the polymer during the healing process. Second, visualization of the treated surface is directly accessible without transferring the sample to other devices. This would also enable the dynamic tracking of the healing process.

Cantilever sensors



For the characterization of the PEMA-g- μ gels and the composites with PEMA homopolymers we have used classic techniques like DMTA, SPM or X-ray scattering. We used the results of the different techniques to draw a picture of how such polymer-grafted nanoparticles behave when they were mixed with like homopolymers. Similar to the results of Green and Mewis⁷ for nanoparticles in dilute

suspensions we found that the molecular weight ratio of brush and matrix is a crucial factor for properties like dispersion behavior or wear resistivity. However, the classic techniques are somewhat limited when a screening of more than one parameter like molecular weight is desired; they become too time consuming and a high amount of material is required. We therefore introduced the concept of mechanical cantilever sensors as a platform for the investigation of mechanical properties of polymers. The polymers were applied as thin films via Inkjet printing from solution for which only small amount of material were needed. We successfully applied the approach of surface initiated polymerization, which we used before to tailor the miscibility of the PEMA-g- μ gels, to lower the surface energy difference between silicon cantilever and printed polymer. In this way homogeneous films with reasonable thickness could be printed.

On the unmodified cantilevers the dewetting of PEMA during the evaporation of the toluene was observed. The dewetting led to an inhomogeneous film which is not applicable for any sensing applications or for material characterization. In contrast, the cantilevers which were modified with the presented grafting method permitted the Inkjet-deposition of a homogeneous, smooth film which covered the whole cantilever.

From theoretical considerations we identified the thickness and the homogeneity of the polymer film as critical parameters for the analysis of the mechanical properties of the polymer film. By using an analytical approach and FEM simulations we were able to reproduce experimental results of an Inkjet printed PEMA film by measuring the resonance frequency of the coated cantilever.

Taking into account that the mechanical properties of polymers depend on the frequency, we proved that a mathematical transformation of a master curve to a temperature dependent modulus curve can be experimentally reproduced. Subsequently by comparing the dynamic response of a polymer-coated MCS (frequency and damping) at different temperatures with the transformed curve we have shown that the response displays the mechanical behavior of the coated film. However, it would be desirable to construct a full mastercurve by using the dynamic response of the cantilever. Thus, I suggest printing a polymer on surface grafted cantilevers with different length. Because of their differing length the levers have also a differing resonance frequency. Upon measuring the resonance frequency and the damping of the cantilevers at different temperatures one could mimic a classic DMTA experiment. To increase the sensitivity of the experiment I propose to print the polymer on both sides of the cantilever. In this way an initial bending of the lever caused by the asymmetric coating would be eliminated. Furthermore, the ratio of cantilever to polymer thickness would be decreased which also increases the sensitivity.

References

1. Maas, J. H.; Fleer, G. J.; Leermakers, F. A. M.; Stuart, M. A. C., Wetting of a polymer brush by a chemically identical polymer melt: Phase diagram and film stability. *Langmuir* **2002**, *18* (23), 8871-8880.
2. Bhat, R. R.; Genzer, J.; Chaney, B. N.; Sugg, H. W.; Liebmann-Vinson, A., Controlling the assembly of nanoparticles using surface grafted molecular and macromolecular gradients. *Nanotechnology* **2003**, *14* (10), 1145-1152.
3. Pihan, S. A.; Emmerling, S. A. L.; Butt, H. J.; Gutmann, J. S.; Berger, R., Nanowear in nanocomposite reinforced polymer. *Submitted* **2011**.
4. Daoud, M.; Cotton, J. P., STAR SHAPED POLYMERS - A MODEL FOR THE CONFORMATION AND ITS CONCENTRATION-DEPENDENCE. *Journal De Physique* **1982**, *43* (3), 531-538.
5. Alexander, S., Adsorption of chain molecules with a polar head a scaling description. *Journal De Physique* **1977**, *38* (8), 983-987.
6. de Gennes, P. G., Conformations of Polymers Attached to an Interface. *Macromolecules* **2002**, *13* (5), 1069-1075.
7. Green, D. L.; Mewis, J., Connecting the wetting and rheological behaviors of poly (dimethylsiloxane)-grafted silica spheres in poly(dimethylsiloxane) melts. *Langmuir* **2006**, *22* (23), 9546-9553.
8. O'Dogherty, M. J.; Huber, J. A.; Dyson, J.; Marshall, C. J., A Study of the Physical and Mechanical Properties of Wheat Straw. *Journal of Agricultural Engineering Research* **1995**, *62* (2), 133-142.
9. Wong, M.; Paramsothy, M.; Xu, X. J.; Ren, Y.; Li, S.; Liao, K., Physical interactions at carbon nanotube-polymer interface. *Polymer* **2003**, *44* (25), 7757-7764.
10. Breuer, O.; Sundararaj, U., Big returns from small fibers: A review of polymer/carbon nanotube composites. *Polymer Composites* **2004**, *25* (6), 630-645.
11. Dunlop-tires <http://www.dunloptires.com/about/>.
12. Liang, J. Z.; Li, R. K. Y., Rubber toughening in polypropylene: A review. *Journal of Applied Polymer Science* **2000**, *77* (2), 409-417.
13. Kanter, J.; Koski, R. E.; Martin, D., The relationship of weight loss to surface roughness of composite resins from simulated toothbrushing. *The Journal of Prosthetic Dentistry* **1982**, *47* (5), 505-513.
14. Poon, W. C. K.; Pusey, P. N., *Observation, Prediction and Simulation of Phase Transitions in Complex Fluids*. Kluwer Academic Publishers: Dordrecht, 1995; Vol. 460, p 664.
15. Vrij, A., Polymers at interfaces and interactions in colloidal dispersions. *Pure and Applied Chemistry* **1976**, *48* (4), 471-483.
16. Asakura, S.; Oosawa, F., On interaction between 2 bodies immersed in a solution of macromolecules. *Journal of Chemical Physics* **1954**, *22* (7), 1255-1256.
17. Bechinger, C.; Rudhardt, D.; Leiderer, P.; Roth, R.; Dietrich, S., Understanding depletion forces beyond entropy. *Physical Review Letters* **1999**, *83* (19), 3960-3963.
18. Stekolnikov, A. A.; Furthm, Ü.; Iler, J.; Bechstedt, F., Absolute surface energies of group-IV semiconductors: Dependence on orientation and reconstruction. *Physical Review B* **2002**, *65* (11), 115318.
19. Lide, D. R., *CRC Handbook of Chemistry and Physics*. CRC, Taylor & Francis: Boca Raton, 2006.

20. Gennes, P.-G.; Brochard-Wyart, F.; Quéré, D., *Capillarity and wetting phenomena*. Springer: New York, 2004.
21. Cherry, B. W., *Polymer surfaces*. Cambridge University Press: Cambridge [Eng.] ; New York, 1981.
22. Surface-Tension <http://www.surface-tension.de/solid-surface-energy.htm>.
23. Kwok, D. Y.; Wu, R.; Li, A.; Neumann, A. W., Contact angle measurements and interpretation: wetting behavior and solid surface tensions for poly(alkyl methacrylate) polymers. *Journal of Adhesion Science and Technology* **2000**, *14* (5), 719-743.
24. Luscombe, C. K.; Li, H.-W.; Huck, W. T. S.; Holmes, A. B., Fluorinated Silane Self-Assembled Monolayers as Resists for Patterning Indium Tin Oxide. *Langmuir* **2003**, *19* (13), 5273-5278.
25. Pihan, S. A. Silizium Wafer Bonding mittels Si-haltiger PECVD-Beschichtungen. Masterthesis, Fachhochschule Wiesbaden, Rüsselsheim, 2008.
26. Liu, Q.; Ding, J.; Chambers, D. E.; Debnath, S.; Wunder, S. L.; Baran, G. R., Filler-coupling agent-matrix interactions in silica/polymethylmethacrylate composites. *Journal of Biomedical Materials Research* **2001**, *57* (3), 384-393.
27. Bauer, F.; Glasel, H. J.; Decker, U.; Ernst, H.; Freyer, A.; Hartmann, E.; Sauerland, V.; Mehnert, R., Trialkoxysilane grafting onto nanoparticles for the preparation of clear coat polyacrylate systems with excellent scratch performance. *Progress in Organic Coatings* **2003**, *47* (2), 147-153.
28. Zhang, H.; Cui, Z. C.; Wang, Y.; Zhang, K.; Ji, X. L.; Lu, C. L.; Yang, B.; Gao, M. Y., From water-soluble CdTe nanocrystals to fluorescent nanocrystal-polymer transparent composites using polymerizable surfactants. *Advanced Materials* **2003**, *15* (10), 777-+.
29. Advincula, R. C., *Polymer brushes: synthesis, characterization, applications*. Wiley-VCH: Weinheim, 2004; p XXIII, 483 S.
30. Milner, S. T., Polymer Brushes. *Science* **1991**, *251* (4996), 905-914.
31. Schärfl, W.; Lindenblatt, G.; Strack, A.; Dziezok, P.; Schmidt, M., Spherical and rod-like colloids with polymer-brush surfaces. *Progress in Colloid and Polymer Science* **1998**, *110*, 285-290.
32. Corbierre, M. K.; Cameron, N. S.; Sutton, M.; Laaziri, K.; Lennox, R. B., Gold nanoparticle/polymer nanocomposites: Dispersion of nanoparticles as a function of capping agent molecular weight and grafting density. *Langmuir* **2005**, *21* (13), 6063-6072.
33. Lan, Q.; Francis, L. F.; Bates, F. S., Silica nanoparticle dispersions in homopolymer versus block copolymer. *Journal of Polymer Science Part B-Polymer Physics* **2007**, *45* (16), 2284-2299.
34. Xu, C.; Ohno, K.; Ladmiral, V.; Composto, R. J., Dispersion of polymer-grafted magnetic nanoparticles in homopolymers and block copolymers. *Polymer* **2008**, *49* (16), 3568-3577.
35. Wang, X. R.; Foltz, V. J.; Rackaitis, M.; Böhm, G. G. A., Dispersing hairy nanoparticles in polymer melts. *Polymer* **2008**, *49* (26), 5683-5691.
36. Lindenblatt, G.; Schärfl, W.; Pakula, T.; Schmidt, M., Structure and dynamics of hairy spherical colloids in a matrix of nonentangled linear chains. *Macromolecules* **2001**, *34* (6), 1730-1736.
37. Flory, P. J., *Principles of polymer chemistry*. Cornell University Press: Ithaca [u.a.], 1986; p XVI, 672 S.
38. Hiemenz, P. C., *Polymer chemistry; the basic concepts*. Dekker: New York; Basel, 1984; p XI, 738 S.
39. Winey, K. I.; Vaia, R. A., Polymer Nanocomposites. *Mrs Bulletin* **2007**, *32* (4), 314-322.

40. Ajayan, P. M.; Schadler, L. S.; Braun, P. V., *Nanocomposite Science and Technology*. Wiley-VCH: Weinheim, 2003.
41. Shull, K. R., Wetting behavior of polymer melts on polydisperse grafted polymer layers. *Macromolecules* **1996**, *29* (26), 8487-8491.
42. Hasegawa, R.; Aoki, Y.; Doi, M., Optimum Graft Density for Dispersing Particles in Polymer Melts. *Macromolecules* **1996**, *29* (20), 6656-6662.
43. Lindenblatt, G.; Schärftl, W.; Pakula, T.; Schmidt, M., Synthesis of polystyrene-grafted polyorganosiloxane microgels and their compatibility with linear polystyrene chains. *Macromolecules* **2000**, *33* (25), 9340-9347.
44. Goldman, A. Y., Prediction of the deformation properties of polymeric and composite materials. American Chemical Society: Washington, DC, 1994.
45. Strobel, G., *The Physics of Polymers: Concepts for Understanding Their Structures and Behavior*. Springer Verlag: 2007.
46. Williams, M. L.; Landel, R. F.; Ferry, J. D., The Temperature Dependence of Relaxation Mechanisms in Amorphous Polymers and Other Glass-forming Liquids. *Journal of the American Chemical Society* **1955**, *77* (14), 3701-3707.
47. Wu, S., Chain entanglement and melt viscosity of compatible polymer blends: poly(methyl methacrylate) and poly(styrene-acrylonitrile). *Polymer* **1987**, *28* (7), 1144-1148.
48. Wu, S., Entanglement between dissimilar chains in compatible polymer blends: poly(methyl methacrylate) and poly(vinylidene fluoride). *Journal of Polymer Science Part B: Polymer Physics* **1987**, *25* (3), 557-566.
49. Eckstein, A.; Suhm, J.; Friedrich, C.; Maier, R. D.; Sassmannshausen, J.; Bochmann, M.; Mulhaupt, R., Determination of Plateau Moduli and Entanglement Molecular Weights of Isotactic, Syndiotactic, and Atactic Polypropylenes Synthesized with Metallocene Catalysts. *Macromolecules* **1998**, *31* (4), 1335-1340.
50. Fetters, L. J.; Lohse, D. J.; Richter, D.; Witten, T. A.; Zirkel, A., Connection between Polymer Molecular Weight, Density, Chain Dimensions, and Melt Viscoelastic Properties. *Macromolecules* **1994**, *27* (17), 4639-4647.
51. Elias, H.-G., *Macromolecules*. In *Physical Structures and Properties*, Wiley-VCH: Weinheim, 2008; Vol. 3.
52. Clark, N. A.; Lunacek, J. H.; Benedek, G. B., A Study of Brownian Motion Using Light Scattering. *American Journal of Physics* **1970**, *38* (5), 575-585.
53. Provencher, S. W., CONTIN: A general purpose constrained regularization program for inverting noisy linear algebraic and integral equations. *Computer Physics Communications* **1982**, *27* (3), 229-242.
54. Butt, H.-J.; Cappella, B.; Kappl, M., Force measurements with the atomic force microscope: Technique, interpretation and applications. *Surface Science Reports* **2005**, *59* (1-6), 1-152.
55. García, R.; Pérez, R., Dynamic atomic force microscopy methods. *Surface Science Reports* **2002**, *47* (6-8), 197-301.
56. Glatter, O.; Kratky, O., *Small angle X-ray scattering*. Academic Press: London [u.a.], 1982; p X, 515 S.
57. Guinier, A., X-ray diffraction at small angles. *Annalen der Physik/Annalen der Physik* **1939**, 161-237.
58. Smilgies, D.-M. <http://staff.chess.cornell.edu/~smilgies/gisaxs/GISAXS.php>.

59. Roth, S. V.; Dohrmann, R.; Dommach, M.; Kuhlmann, M.; Kroger, I.; Gehrke, R.; Walter, H.; Schroer, C.; Lengeler, B.; Muller-Buschbaum, P., Small-angle options of the upgraded ultrasmall-angle x-ray scattering beamline BW4 at HASYLAB. *Review of Scientific Instruments* **2006**, *77*.
60. Wolkenhauer, M.; Bumbu, G. G.; Cheng, Y.; Roth, S. V.; Gutmann, J. S., Investigation of micromechanical cantilever sensors with microfocus grazing incidence small-angle X-ray scattering. *Applied Physics Letters* **2006**, *89* (5).
61. Yoneda, Y., Anomalous Surface Reflection of X Rays. *Physical Review* **1963**, *131* (5), 2010.
62. Jones, D. I. G., *Handbook of Viscoelastic Vibration Damping*. John Wiley & Sons, Ltd: West Sussex, 2001.
63. Sampath, U.; Heinrich, S. M.; Josse, F.; Lochon, F.; Dufour, I.; Rebiere, D., Study of viscoelastic effect on the frequency shift of microcantilever chemical sensors. *Ieee Transactions on Ultrasonics Ferroelectrics and Frequency Control* **2006**, *53* (11), 2166-2173.
64. de Gans, B. J.; Duineveld, P. C.; Schubert, U. S., Inkjet Printing of Polymers: State of the Art and Future Developments. *Advanced Materials* **2004**, *16* (3), 203-213.
65. Petyt, M., *Introduction to finite element vibration analysis*. Cambridge University Press: Cambridge, 1990.
66. Guillaume, P., *Modal Analysis*. Vrije Universiteit Brussel: Brussel, Belgium.
67. Ramakrishnan, A.; Dhamodharan, R., Facile synthesis of ABC and CBABC multiblock copolymers of styrene, tert-butyl acrylate, and methyl methacrylate via room temperature ATRP of MMA. *Macromolecules* **2003**, *36* (4), 1039-1046.
68. Wind, M.; Graf, R.; Renker, S.; Spiess, H. W., Structural Reasons for Restricted Backbone Motion in Poly(n-alkyl methacrylates): Degree of Polymerization, Tacticity and Side-Chain Length. *Macromolecular Chemistry and Physics* **2005**, *206* (1), 142-156.
69. Marutani, E.; Yamamoto, S.; Ninjbadgar, T.; Tsujii, Y.; Fukuda, T.; Takano, M., Surface-initiated atom transfer radical polymerization of methyl methacrylate on magnetite nanoparticles. *Polymer* **2004**, *45* (7), 2231-2235.
70. Emmerling, S. G. J. *Polymer Brushes - Wetting Properties and μ -Patterning*. Johannes Gutenberg-Universität Mainz, 2010.
71. Dutta, N.; Green, D., Nanoparticle Stability in Semidilute and Concentrated Polymer Solutions. *Langmuir* **2008**, *24* (10), 5260-5269.
72. Wijmans, C. M.; Zhulina, E. B.; Fler, G. J., Effect of Free Polymer on the Structure of a Polymer Brush and Interaction between Two Polymer Brushes. *Macromolecules* **1994**, *27* (12), 3238-3248.
73. Zhou, T. H.; Ruan, W. H.; Yang, J. L.; Rong, M. Z.; Zhang, M. Q.; Zhang, Z., A novel route for improving creep resistance of polymers using nanoparticles. *Composites Science and Technology* **2007**, *67* (11-12), 2297-2302.
74. Jakuczek, L.; Gutmann, J. S.; Müller, B.; Rosenauer, C.; Zuchowska, D., Well-defined core-shell structures based on silsesquioxane microgels: Grafting of polystyrene via ATRP and product characterization. *Polymer* **2008**, *49* (4), 843-856.
75. Liang, K. W.; Li, G. Z.; Toghiani, H.; Koo, J. H.; Pittman, C. U., Cyanate ester/polyhedral oligomeric silsesquioxane (POSS) nanocomposites: Synthesis and characterization. *Chemistry of Materials* **2006**, *18* (2), 301-312.

76. Berger, R.; Cheng, Y.; Förch, R.; Gotsmann, B.; Gutmann, J. S.; Pakula, T.; Rietzler, U.; Schärfl, W.; Schmidt, M.; Strack, A.; Windeln, J.; Butt, H. J., Nanowear on Polymer Films of Different Architecture. *Langmuir* **2007**, *23* (6), 3150-3156.
77. Hutter, J. L.; Bechhoefer, J., CALIBRATION OF ATOMIC-FORCE MICROSCOPE TIPS. *Review of Scientific Instruments* **1993**, *64* (7), 1868-1873.
78. Shipway, P. H.; Ngao, N. K., Microscale abrasive wear of polymeric materials. *Wear* **2003**, *255* (1-6), 742-750.
79. Briscoe, B. J.; Pelillo, E.; Sinha, S. K.; Evans, P. D., Scratching maps for polymers. *Wear* **1996**, *200* (1-2), 137-147.
80. Dasari, A.; Yu, Z.-Z.; Mai, Y.-W., Fundamental aspects and recent progress on wear/scratch damage in polymer nanocomposites. *Materials Science and Engineering: R: Reports* **2009**, *63* (2), 31-80.
81. Dinelli, F.; Leggett, G.; Shipway, P., Nanowear of polystyrene surfaces: molecular entanglement and bundle formation. *Nanotechnology* **2005**, *16* (6), 675.
82. Gotsmann, B.; Duerig, U. T.; Sills, S.; Frommer, J.; Hawker, C. J., Controlling Nanowear in a Polymer by Confining Segmental Relaxation. *Nano Letters* **2006**, *6* (2), 296-300.
83. Bhuyan, S.; Sundararajan, S.; Andjelkovic, D.; Larock, R., Micro- and nano-tribological behavior of soybean oil-based polymers of different crosslinking densities. *Tribology International* **2010**, *43* (11), 2231-2239.
84. Rong, M. Z.; Zhang, M. Q.; Zheng, Y. X.; Zeng, H. M.; Walter, R.; Friedrich, K., Structure-property relationships of irradiation grafted nano-inorganic particle filled polypropylene composites. *Polymer* **2001**, *42* (1), 167-183.
85. Vettiger, P.; Cross, G.; Despont, M.; Drechsler, U.; Durig, U.; Gotsmann, B.; Haberle, W.; Lantz, M. A.; Rothuizen, H. E.; Stutz, R.; Binnig, G. K., The "millipede" - Nanotechnology entering data storage. *Ieee Transactions on Nanotechnology* **2002**, *1* (1), 39-55.
86. Sirringhaus, H.; Kawase, T.; Friend, R. H.; Shimoda, T.; Inbasekaran, M.; Wu, W.; Woo, E. P., High-resolution inkjet printing of all-polymer transistor circuits. *Science* **2000**, *290* (5499), 2123-2126.
87. Zhang, J.; Li, C. M.; Chan-Park, M. B.; Zhou, Q.; Gan, Y.; Qin, F.; Ong, B.; Chen, T., Fabrication of thin-film organic transistor on flexible substrate via ultraviolet transfer embossing. *Applied Physics Letters* **2007**, *90* (24).
88. Starostin, S. A.; Premkumar, P. A.; Creatore, M.; de Vries, H.; Paffen, R. M. J.; van de Sanden, M. C. M., High current diffuse dielectric barrier discharge in atmospheric pressure air for the deposition of thin silica-like films. *Applied Physics Letters* **2010**, *96* (6).
89. Weber, M. F.; Stover, C. A.; Gilbert, L. R.; Nevitt, T. J.; Ouderkirk, A. J., Giant birefringent optics in multilayer polymer mirrors. *Science* **2000**, *287* (5462), 2451-2456.
90. Edrington, A. C.; Urbas, A. M.; DeRege, P.; Chen, C. X.; Swager, T. M.; Hadjichristidis, N.; Xenidou, M.; Fetters, L. J.; Joannopoulos, J. D.; Fink, Y.; Thomas, E. L., Polymer-based photonic crystals. *Advanced Materials* **2001**, *13* (6), 421-425.
91. Ibanescu, M.; Fink, Y.; Fan, S.; Thomas, E. L.; Joannopoulos, J. D., An all-dielectric coaxial waveguide. *Science* **2000**, *289* (5478), 415-419.
92. Sandrock, M. L.; Shirk, J. S.; Tai, H. W.; Ranade, A.; Wiggins, M.; Baer, E.; Hiltner, A., Tunable refractive index nanolayered polymer systems. *Abstracts of Papers of the American Chemical Society* **2003**, *226*, 147-PMSE.

93. Jiang, H.; O'Neill, K.; Grant, J. T.; Tullis, S.; Eyink, K.; Johnson, W. E.; Fleitz, P.; Bunning, T. J., Variable refractive index polymer thin films prepared by plasma copolymerization. *Chemistry of Materials* **2004**, *16* (7), 1292-1297.
94. Wiesmann, D.; Rawlings, C.; Vecchione, R.; Porro, F.; Gotsmann, B.; Knoll, A.; Pires, D.; Duerig, U., Multi Tbit/in(2) Storage Densities with Thermomechanical Probes. *Nano Letters* **2009**, *9* (9), 3171-3176.
95. Lantz, M. A.; Gotsmann, B.; Durig, U. T.; Vettiger, P.; Nakayama, Y.; Shimizu, T.; Tokumoto, H., Carbon nanotube tips for thermomechanical data storage. *Applied Physics Letters* **2003**, *83* (6), 1266-1268.
96. Gotsmann, B.; Duerig, U.; Frommer, J.; Hawker, C. J., Exploiting chemical switching in a Diels-Alder polymer for nanoscale probe lithography and data storage. *Advanced Functional Materials* **2006**, *16* (11), 1499-1505.
97. Leung, O. M.; Goh, M. C., Orientational Ordering of Polymers by Atomic Force Microscope Tip-Surface Interaction. *Science* **1992**, *255* (5040), 64-66.
98. Chifen, A. N.; Jenkins, A. T. A.; Knoll, W.; Forch, R., Adhesion improvement of plasma-polymerized maleic anhydride films on gold using HMDSO/O-2 adhesion layers. *Plasma Processes and Polymers* **2007**, *4* (9), 815-822.
99. Dennler, G.; Houdayer, A.; Raynaud, P.; Seguy, I.; Segui, Y.; Wertheimer, M. R., Growth modes of SiO_x films deposited by evaporation and plasma-enhanced chemical vapor deposition on polymeric substrates. *Plasmas and Polymers* **2003**, *8* (1), 43-59.
100. Fan, X. W.; Park, M. K.; Xia, C. J.; Advincula, R., Surface structural characterization and mechanical testing by nanoindentation measurements of hybrid polymer/clay nanostructured multilayer films. *Journal of Materials Research* **2002**, *17* (7), 1622-1633.
101. Beake, B. D.; Leggett, G. J.; Alexander, M. R., Scanning force microscopy of plasma polymerised hexane: information on the mechanical properties of thin films from tip-induced wear. *Polymer* **2001**, *42* (6), 2647-2653.
102. Wang, L. A.; Chen, H. L., Multilayer hexamethyldisiloxane film as bottom antireflective coating for ArF lithography. *Journal of Vacuum Science & Technology B* **1999**, *17* (6), 2772-2775.
103. Patelli, A.; Vezzu, S.; Zottarel, L.; Menin, E.; Sada, C.; Martucci, A.; Costacurta, S., SiO_x-Based Multilayer Barrier Coatings Produced by a Single PECVD Process. *Plasma Processes and Polymers* **2009**, *6*, S665-S670.
104. Angelini, E.; d'Agostino, R.; Fracassi, F.; Grassini, S.; Rosalbino, F., Surface analysis of PECVD organosilicon films for corrosion protection of steel substrates. *Surface and Interface Analysis* **2002**, *34* (1), 155-159.
105. Hayakawa, T.; Yoshinari, M.; Nemoto, K., Characterization and protein-adsorption behavior of deposited organic thin film onto titanium by plasma polymerization with hexamethyldisiloxane. *Biomaterials* **2004**, *25* (1), 119-127.
106. Benitez, F.; Martinez, E.; Esteve, J., Improvement of hardness in plasma polymerized hexamethyldisiloxane coatings by silica-like surface modification. *Thin Solid Films* **2000**, *377*, 109-114.
107. Benitez, F.; Martinez, E.; Galan, M.; Serrat, J.; Esteve, J., Mechanical properties of plasma deposited polymer coatings. *Surface & Coatings Technology* **2000**, *125* (1-3), 383-387.
108. Zajickova, L.; Bursikova, V.; Kucerova, Z.; Franta, D.; Dvorak, P.; Smid, R.; Perina, V.; Mackova, A., Deposition of protective coatings in rf organosilicon discharges. *Plasma Sources Science & Technology* **2007**, *16* (1), S123-S132.

109. Benissad, N.; Boisse-Laporte, C.; Vallee, C.; Granier, A.; Goullet, A., Silicon dioxide deposition in a microwave plasma reactor. *Surface & Coatings Technology* **1999**, *116*, 868-873.
110. Forch, R.; Zhang, Z. H.; Knoll, W., Soft plasma treated surfaces: Tailoring of structure and properties for biomaterial applications. *Plasma Processes and Polymers* **2005**, *2* (5), 351-372.
111. Magonov, S. N.; Reneker, D. H., Characterization of polymer surfaces with atomic force microscopy. *Annual Review of Materials Science* **1997**, *27*, 175-222.
112. Schneider, D.; Schwarz, T., A photoacoustic method for characterising thin films. *Surface & Coatings Technology* **1997**, *91* (1-2), 136-146.
113. Kaule, T.; Pihan, S. A.; Zhang, Y.; Emmerling, S. A. L.; Förch, R.; Gutmann, J. S.; Butt, H. J.; Berger, R.; Knoll, A. W.; Dürig, U.; Gotsmann, B., Hyper-thin waer protection layers for nanoscale thermomechanical data storage. *Submitted* **2011**.
114. Tranchida, D.; Piccarolo, S.; Soliman, M., Nanoscale mechanical characterization of polymers by AFM nanoindentations: Critical approach to the elastic characterization. *Macromolecules* **2006**, *39* (13), 4547-4556.
115. Bowden, N.; Huck, W. T. S.; Paul, K. E.; Whitesides, G. M., The controlled formation of ordered, sinusoidal structures by plasma oxidation of an elastomeric polymer. *Applied Physics Letters* **1999**, *75* (17), 2557-2559.
116. Stafford, C. M.; Harrison, C.; Beers, K. L.; Karim, A.; Amis, E. J.; VanLandingham, M. R.; Kim, H.-C.; Volksen, W.; Miller, R. D.; Simonyi, E. E., A buckling-based metrology for measuring the elastic moduli of polymeric thin films. *Nat Mater* **2004**, *3* (8), 545-550.
117. Volynskii, A. L.; Bazhenov, S.; Lebedeva, O. V.; Bakeev, N. F., Mechanical buckling instability of thin coatings deposited on soft polymer substrates. *Journal of Materials Science* **2000**, *35* (3), 547-554.
118. Knittel, D.; Kesting, W.; Schollmeyer, E., Surface Structuring of Synthetic Fibres by UV Laser Irradiation, Part I: Phenomenological Report. *Polymer International* **1997**, *43* (3), 231-239.
119. Genzer, J.; Groenewold, J., Soft matter with hard skin: From skin wrinkles to templating and material characterization. *Soft Matter* **2006**, *2* (4), 310-323.
120. Brush, D. O.; Almoth, B. O., *Buckling of Bars, Plates and Shells*. McGraw-Hill: New York, 1975.
121. Bowden, N.; Brittain, S.; Evans, A. G.; Hutchinson, J. W.; Whitesides, G. M., Spontaneous formation of ordered structures in thin films of metals supported on an elastomeric polymer. *Nature* **1998**, *393* (6681), 146-149.
122. Katzenberg, F., Irradiation- and Strain-Induced Self-Organization of Elastomer Surfaces. *Macromolecular Materials and Engineering* **2001**, *286* (1), 26-29.
123. Harrison, C.; Stafford, C. M.; Zhang, W.; Karim, A., Sinusoidal phase grating created by a tunably buckled surface. *Applied Physics Letters* **2004**, *85* (18), 4016-4018.
124. Lu, C.; Dönch, I.; Nolte, M.; Fery, A., Au Nanoparticle-based Multilayer Ultrathin Films with Covalently Linked Nanostructures: Spraying Layer-by-layer Assembly and Mechanical Property Characterization. *Chemistry of Materials* **2006**, *18* (26), 6204-6210.
125. Lu, C.; Mohwald, H.; Fery, A., A lithography-free method for directed colloidal crystal assembly based on wrinkling. *Soft Matter* **2007**, *3* (12), 1530-1536.
126. Nolte, A. J.; Rubner, M. F.; Cohen, R. E., Determining the Young's Modulus of Polyelectrolyte Multilayer Films via Stress-Induced Mechanical Buckling Instabilities. *Macromolecules* **2005**, *38* (13), 5367-5370.

127. Carbone, G.; Mangialardi, L., Adhesion and friction of an elastic half-space in contact with a slightly wavy rigid surface. *Journal of the Mechanics and Physics of Solids* **2004**, *52* (6), 1267-1287.
128. Chennamsetty, R.; Escobar, I.; Xu, X., Characterization of commercial water treatment membranes modified via ion beam irradiation. *Desalination* **2006**, *188* (1-3), 203-212.
129. Büscher, K.; Berger, R.; Brünger, W.; Graf, K., Surface morphologies in polymers by irradiation with argon ions and consecutive swelling. *Microelectronic Engineering* **2006**, *83* (4-9), 819-822.
130. Martínez-Pardo, M. E.; Cardoso, J.; Vázquez, H.; Aguilar, M.; Rickards, J.; Andrade, E., Characterization of MeV proton irradiated PS films. *Nuclear Instruments and Methods in Physics Research Section B: Beam Interactions with Materials and Atoms* **1997**, *131* (1-4), 219-225.
131. Bruenger, W. H.; Torkler, M.; Leung, K. N.; Lee, Y.; Williams, M. D.; Loeschner, H.; Stengl, G.; Fallmann, W.; Paschke, F.; Stangl, G.; Rangelow, I. W.; Hudek, P., Resolution improvement of ion projector with a low energy spread multicusp ion source. *Microelectronic Engineering* **1999**, *46* (1-4), 477-480.
132. Karade, Y.; Pihan, S. A.; Brünger, W. H.; Dietzel, A.; Berger, R.; Graf, K., Determination of Cross-Link Density in Ion-Irradiated Polystyrene Surfaces from Rippling. *Langmuir* **2009**, *25* (5), 3108-3114.
133. Kuhn, W., Dependence of the average transversal on the longitudinal dimensions of statistical coils formed by chain molecules. *Journal of Polymer Science* **1946**, *1* (5), 380-388.
134. Zhang, X.; Aji, A., Biaxial orientation behavior of polystyrene: Orientation and properties. *Journal of Applied Polymer Science* **2003**, *89* (2), 487-496.
135. Cleaver, J. A. S.; Looi, L., AFM study of adhesion between polystyrene particles; -- The influence of relative humidity and applied load. *Powder Technology* **2007**, *174* (1-2), 34-37.
136. Seitz, J. T., The estimation of mechanical properties of polymers from molecular structure. *Journal of Applied Polymer Science* **1993**, *49* (8), 1331-1351.
137. Bonaccorso, E.; Cappella, B.; Graf, K., Local Mechanical Properties of Plasma Treated Polystyrene Surfaces. *The Journal of Physical Chemistry B* **2006**, *110* (36), 17918-17924.
138. Kogler, F. R.; Koch, T.; Peterlik, H.; Seidler, S.; Schubert, U., Mechanical, thermomechanical, and thermal properties of polystyrene crosslinked with a multifunctional zirconium oxo cluster. *Journal of Polymer Science Part B: Polymer Physics* **2007**, *45* (16), 2215-2231.
139. Jiang, C.; Singamaneni, S.; Merrick, E.; Tsukruk, V. V., Complex Buckling Instability Patterns of Nanomembranes with Encapsulated Gold Nanoparticle Arrays. *Nano Letters* **2006**, *6* (10), 2254-2259.
140. Finot, E.; Passian, A.; Thundat, T., Measurement of mechanical properties of cantilever shaped materials. *Sensors* **2008**, *8* (5), 3497-3541.
141. Berger, R.; Gerber, C.; Lang, H. P.; Gimzewski, J. K., Micromechanics: A toolbox for femtoscale science: "Towards a laboratory on a tip". *Microelectronic Engineering* **1997**, *35* (1-4), 373-379.
142. Stoney, G. G., The tension of metallic films deposited by electrolysis. *Proceedings of the Royal Society of London Series a-Containing Papers of a Mathematical and Physical Character* **1909**, *82* (553), 172-175.
143. Zhao, J.; Berger, R.; Gutmann, J. S., Thermal contributions to the bending of bimaterial cantilever sensors. *Applied Physics Letters* **2006**, *89* (3), 3.

144. Zhang, R.; Graf, K.; Berger, R., Swelling of cross-linked polystyrene spheres in toluene vapor. *Applied Physics Letters* **2006**, *89* (22).
145. Ilic, B.; Craighead, H. G.; Krylov, S.; Senaratne, W.; Ober, C.; Neuzil, P., Attogram detection using nanoelectromechanical oscillators. *Journal of Applied Physics* **2004**, *95* (7), 3694-3703.
146. Sandberg, R.; Molhave, K.; Boisen, A.; Svendsen, W., Effect of gold coating on the Q-factor of a resonant cantilever. *Journal of Micromechanics and Microengineering* **2005**, *15* (12), 2249-2253.
147. Dongkyu, L.; Seonghwan, K.; Namchul, J.; Thundat, T.; Sangmin, J., Effects of gold patterning on the bending profile and frequency response of a microcantilever. *Journal of Applied Physics* **2009**, 024310 (7 pp.).
148. Sandberg, R.; Svendsen, W.; Molhave, K.; Boisen, A., Temperature and pressure dependence of resonance in multi-layer microcantilevers. *Journal of Micromechanics and Microengineering* **2005**, *15* (8), 1454-1458.
149. Kiesewetter, L.; Zhang, J. M.; Houdeau, D.; Steckenborn, A., Determination of Young's moduli of micromechanical thin films using the resonance method. *Sensors and Actuators a-Physical* **1992**, *35* (2), 153-159.
150. Haque, M. A.; Saif, M. T. A., In-situ tensile testing of nano-scale specimens in SEM and TEM. *Proceedings of the Society for Experimental Mechanics, Inc* **2002**, *49*, 123-128.
151. Bietsch, A.; Zhang, J. Y.; Hegner, M.; Lang, H. P.; Gerber, C., Rapid functionalization of cantilever array sensors by inkjet printing. *Nanotechnology* **2004**, *15* (8), 873-880.
152. Sibus, H.; Güther, V.; Roidl, O.; Habashi, F.; Wolf, H. U., Titanium, Titanium Alloys, and Titanium Compounds. *Ullmann's Encyclopedia of Industrial Chemistry* **2000**.
153. Neugebauer, C. A., Tensile Properties of Thin, Evaporated Gold Films. *Journal of Applied Physics* **1960**, *31* (6), 1096-1101.
154. Ransley, J. H. T.; Watari, M.; Sukumaran, D.; McKendry, R. A.; Seshia, A. A., SU8 bio-chemical sensor microarrays. *Microelectronic Engineering* **2006**, *83* (4-9), 1621-1625.
155. Keller, S.; Haefliger, D.; Boisen, A., Fabrication of thin SU-8 cantilevers: initial bending, release and time stability. *Journal of Micromechanics and Microengineering* **2010**, *20* (4), 11.
156. Greve, A.; Keller, S.; Vig, A. L.; Kristensen, A.; Larsson, D.; Yvind, K.; Hvam, J. M.; Cerruti, M.; Majumdar, A.; Boisen, A., Thermoplastic microcantilevers fabricated by nanoimprint lithography. *Journal of Micromechanics and Microengineering* **2009**, *20* (1).
157. Llobera, A.; Cadarso, V. J.; Zinoviev, K.; Dominguez, C.; Buttgenbach, S.; Vila, J.; Plaza, J. A., Poly(Dimethylsiloxane) Waveguide Cantilevers for Optomechanical Sensing. *Ieee Photonics Technology Letters* **2009**, *21* (1-4), 79-81.
158. Mason, W. P., *Physical Acoustics and the Properties of Solids*. Van Nostrand, Princeton, N.J., 1958.
159. Bumbu, G. G.; Kircher, G.; Wolkenhauer, M.; Berger, R.; Gutmann, J. S., Synthesis and characterization of polymer brushes on micromechanical cantilevers. *Macromolecular Chemistry and Physics* **2004**, *205* (13), 1713-1720.
160. Kim, J.-B.; Bruening, M. L.; Baker, G. L., Surface-Initiated Atom Transfer Radical Polymerization on Gold at Ambient Temperature. *Journal of the American Chemical Society* **2000**, *122* (31), 7616-7617.
161. Ehrenstein, G. W.; Riedel, G.; Trawiel, P., *Praxis der thermischen Analyse von Kunststoffen*. Hanser: 2003.

162. Smith, W. F.; Hashemi, J., *Foundations of Material Science and engineering*. 4 ed.; McGraw-Hill: 2006.
163. Pieranski, P., Two-Dimensional Interfacial Colloidal Crystals. *Physical Review Letters* **1980**, *45* (7), 569.
164. Retsch, M. Complex materials via colloidal crystallization. Johannes Gutenberg-Universität Mainz, 2009.
165. Minshall, H., *CRC Handbook of Chemistry and Physics*. CRC, Taylor & Francis: Boca Raton, 2006.
166. Liu, T.; Pihan, S. A.; Berger, R., Formation of thin polymer films via fusion of colloidal monolayers. *Submitted* **2011**.
167. Leibler, L.; Ajdari, A.; Mourran, A.; Coulon, G.; Chatenay, D., *Ordering in Macromolecular Systems*. Springer Verlag: Berlin, 1993.
168. Gay, C., Wetting of a Polymer Brush by a Chemically Identical Polymer Melt. *Macromolecules* **1997**, *30* (19), 5939-5943.
169. Gast, A. P.; Leibler, L., *Effect of polymer solutions on sterically stabilized suspensions*. American Chemical Society: Washington, DC, ETATS-UNIS, 1985; Vol. 89.
170. Gast, A. P.; Leibler, L., INTERACTIONS OF STERICALLY STABILIZED PARTICLES SUSPENDED IN A POLYMER-SOLUTION. *Macromolecules* **1986**, *19* (3), 686-691.
171. Vincent, B.; Luckham, P. F.; Waite, F. A., EFFECT OF FREE POLYMER ON THE STABILITY OF STERICALLY STABILIZED DISPERSIONS. *Journal of Colloid and Interface Science* **1980**, *73* (2), 508-521.
172. Vincent, B.; Edwards, J.; Emmett, S.; Jones, A., DEPLETION FLOCCULATION IN DISPERSIONS OF STERICALLY-STABILIZED PARTICLES (SOFT SPHERES). *Colloids and Surfaces* **1986**, *18* (2-4), 261-281.
173. Yuan, Y. C.; Yin, T.; Rong, M. Z.; Zhang, M. Q., Self healing in polymers and polymer composites. Concepts, realization and outlook: A review. *Express Polymer Letters* **2008**, *2* (4), 238-250.
174. Tan, P. S.; Zhang, M. Q.; Bhattacharyya, D., Processing and performance of self-healing materials. *IOP Conference Series: Materials Science and Engineering* **2009**, *4*, 012017 (5 pp.)-012017 (5 pp.).
175. Li, G. Q.; John, M., A self-healing smart syntactic foam under multiple impacts. *Composites Science and Technology* **2008**, *68* (15-16), 3337-3343.
176. Haiyan, L.; Rongguo, W.; Honglin, H.; Wenbo, L., Surface modification of self-healing poly(urea-formaldehyde) microcapsules using silane-coupling agent. *Applied Surface Science* **2008**, *255* (5), 1894-1900.
177. Wool, R. P.; O'Connor, K. M., A theory crack healing in polymers. *Journal of Applied Physics* **1981**, *52* (10), 5953-5963.

Acknowledgements

*"I may not have gone where I intended to go, but I think I have ended up where I needed to be" *¹.*

During my time at the MPIP in Mainz, and especially during my PhD, many people accompanied me in my scientific work and my personal life. I'd like to take the chance to express my gratitude to my supervisors, colleagues, friends and some people that I grew fond of.

Without the great effort of my supervisor **Prof. Hans-Jürgen Butt**, my way would probably have been much different. I am an Engineer with a degree of a Fachhochschule (Dipl.- Ing., MSc.) and unfortunately the Bologna Declaration from 1999, to make European higher education more compatible and comparable, has not yet entered all Universities in Germany. Due to his attempts, finally the University of Siegen, where he is an Außerplanmäßiger professor, accepted my application and he was my temporary supervisor for the first six month of my PhD. With his invaluable input during several discussions and the infrastructure he offered me in his group in Mainz, I had the best chance a young scientist can think of. Thank you!

I want to express my gratitude to my Doktorvater **Prof. Holger Schönherr** from the University of Siegen. Coincidental we came into contact since he is a good colleague of Renate Förch, which was the supervisor of my master thesis at the MPIP. At the very beginning of my PhD he accepted a chair at the University of Siegen and was about to move from the Netherlands. Nevertheless he took the time to discuss about my topic and gave me the chance to start a PhD in his new group as an external student. With fruitful discussions and his excellent tips he guided me thru my thesis. Thank you!

The most important person during my PhD was **Rüdiger Berger**. I got to know him during my master thesis where he fascinated me with interesting projects when I was searching for Phd topics. The hard school of knocks when discussing abstracts for conferences, posters or manuscripts with him was a blessing in disguise. I remember that my very first abstract for a conference came back full of comments and modifications. He wrote more comments than the length of the actual text. I'll never forget his comment about the fifth iteration of the abstract: *da fehlt noch mehr Fleisch!* After some time I realized that, whenever we discussed a text or a poster it became much better afterwards. As time passed his comments to my texts became less since once, I think it was in my third year, I received a document with only one comment. I jumped up from my desk, running into the next office where my colleagues were sitting and informed them about this unusual happening. The only comment of my colleague Stefan was: welcome to level three! I want to express my gratitude to Rüdiger for his professional and personal supervision of my work. With his subtle instinct for

*¹ Douglas Adams, The Long Dark Tea-Time of the Soul, 1988.

important details he always managed to guide me to the best results and beside work there was always time for a chat or a laugh. Thank you!

A mayor part of my work was based on materials which were synthesized by **Sebastian Emmerling**. I'd like to thank him for the nice teamwork that he kept always at a high professional level. I will never forget the night shifts we had in Hamburg at the DESY, walking around the construction site of PETRA at 3 am.

I also like to thank some other people from the institute that contributed to my work in different ways. I want to thank **Kaloian Koynov** for the intense discussions about the DMTA results and the pink curves. Many thanks to **Gunnar Kircher** and **Andreas Hanewald** for the support in the labs. Many thanks to **Uwe Rietzler** who taught me how to use the SPM and lend a helping hand at numerous occasions. Thanks to **Maren Müller** for hours of FIB-cutting my cantilevers and **Helma Burg** for the support with SPM measurements and the grapes for the wine. For the fruitful cooperations and the interesting projects I want to thank **Davide Tranchida**, **Chuanjun Liu**, **Elmar Bonaccurso** and **Charly Graf**. For the warm welcome and the very helpful support in Japan I want to thank **Akiko Itakura** and **Prof. Sasaki**. Yoroshiku onegai shimasu!

I want to thank **Stefan Weber** for being my colleague and friend during the last years. He was always a source of knowledge, constructive ideas and jokes. We had a great time not only on a professional level but also in our free time during several cooking sessions. Distraction from my work, improvement of my English and relaxing my muscle ache were supported by **Riccardo Raccis** during endless chess games (count 36:26 for him), countless human chess sessions at Lomo and refreshing sauna evenings. Thank you dude! Many thanks to **Simone Lerch**, **Karen Johnston** and **Regina Bauer** for taking care of Schovis during conferences and my trips abroad.

If you did not find any misspelling in this work, it is the merit of **Anna Domanski**, **Rabea Keller**, **Huong Ngyuen**, **Riccardo Raccis**, **Esha Sengupta**, **Charly Mears** and **Stefan Weber**. If you do so, it was my brainchild!

I want to thank my parents **Petra Pihan** and **Kurt Pihan** who encouraged me to study and let me go make my own way. Thanks to my brother **Andreas Pihan** and his wife **Natascha Pihan** for the mental support and the delicious dinners. Thank you Schovis for being my living alarm clock, which made noise at 7 am every day. I also like to thank the **Deutsche Forschungsgemeinschaft** for financial support under the **SPP1369** Priority program (Polymer-Solid contacts: Interfaces and Interphases).

So long, and thanks for all the fish.

List of publications

- [1] **Pihan, Sascha A.**; Emmerling, Sebastian G.J.; Butt, Hans-Jürgen; Gutmann, J. S.; Berger, R., *Nanowear in nanocomposite reinforced polymer*, *Wear* **2011**, DOI: 10.1016/j.wear.2011.05.040.
- [2] Filipe Natalio, Rute André, **Sascha A. Pihan**, Madalena Humanes, Ron Wever and Wolfgang Tremel; V2O5 nanowires with an intrinsic iodination activity leading to the formation of self-assembled melanin-like biopolymers, *Journal of Materials Chemistry*, **2011**, DOI: 10.1039/C1JM11811K.
- [3] Hans-Jürgen Butt, Maria Retschke, Ali Golriz, **Sascha A. Pihan**, Rüdiger Berger; Electric field-induced condensation: An extension of the Kelvin Equation, *Physical Review E* **2011**, (83), 6, DOI: 10.1103/PhysRevE.83.061604
- [4] Chuanjun Liu, Marcus C. Lopes, **Sascha A. Pihan**, Daniela Fell, Mordechai Sokuler, Hans-Jürgen Butt, Günter K. Auernhammer, Elmar Bonaccorso, Water diffusion in polymer nanofilms measured with microcantilevers , *Sensors and Actuators B*, **2011**, DOI: 10.1016/j.snb.2011.07.007.
- [5] Tranchida, Davide; **Pihan, Sascha A.**; Zhang, Yi; et al., Nanomechanical Properties of Advanced Plasma Polymerized Coatings for Mechanical Data Storage, *The Journal of Physical Chemistry B* **2011**, DOI: 10.1021/jp112211c
- [6] Emmerling, Sebastian G. J.; Langer, Laura B. N.; **Pihan, Sascha A.**; Lellig, P.; Gutmann, J. S., Patterning of a Surface Immobilized ATRP Initiator with an Inkjet Printer, *Macromolecules* **2010**, 43(11), 5033-5042. DOI: 10.1021/ma902836n
- [7] Zhang, Yi; Arfsten, Judith; **Pihan, Sascha A.**; Kaule, T. Förch; R. Berger, R. , Interface roughness of plasma deposited polymer layers, *Journal of Colloid and Interface Science* **2010**, 351(2), 532-536. DOI: 10.1016/j.jcis.2010.07.051
- [8] Karade, Y; **Pihan, Sascha A.**; Brünger, W. H.; Dietzel, A.; Berger, R.; Graf, K. , Determination of Cross-Link Density in Ion-Irradiated Polystyrene Surfaces from Rippling, *Langmuir* **2009**, 25(5), 3108-3114. DOI: 10.1021/la802363v
- [9] **Pihan, Sascha A.**; Tsukruk, T.; Förch, R., Plasma polymerized hexamethyl disiloxane in adhesion applications, *Surface & Coatings Technology* **2009**, 203(13), 1856-1862. DOI: 10.1016/j.surfcoat.2009.01.026

Oral presentations at international conferences

- 05 / 2010** Session 4: „Physical phenomena in micro/nano cantilevers“, Workshop on Nanomechanical cantilever Sensors, Banff, Canada. „Elastic modulus of thin, plasma polymerized film determined by micromechanical cantilever sensors“
- 04 / 2010** Topic: Structure, Morphology and Properties of Polymers: „Characterisation, testing, simulation/modelling“, POLYCHAR18, Siegen, Germany. „The Mechanical Properties of Brush-Coated Nanoparticles in Homopolymer A Matrix“
- 12 / 2009** Symposium FF: „Mechanical Behavior of Nanomaterials – Experiments and Modelling“, MRS Fall meeting, Boston, MA. „The Mechanical Properties of Brush-Coated Nanoparticles in Homopolymer Matrix“

Poster presentations at international conferences

- 07 / 2010** Priority Program: „Polymer-Solid contacts: Interfaces and Interphases“, 2. Annual Meeting, Dechema Frankfurt, Germany. „Synthesis and characterization of hairy nano-particles. Influence of matrix molecular weight on conformation of brushes “
- 12 / 2009** Frontiers in Polymer Science: „Polymer Physics“, Mainz, Germany. „Ultrathin Polymeric Films For Scanning Probe Based Storage Media “
- 09 / 2009** Polymer Interfaces: „Science and Technology“, International Bunsen Discussion Meeting, Darmstadt, Germany. „Synthesis and characterization of hairy nano-particles for polymer reinforcement “